Spring 4-19-2022

Nano-fabricated Atomic Waveguides for Inertial Measurements

Adrian S. Orozco

Adrian Orozco

Candidate

Physics

Department

This dissertation is approved, and it is acceptable in quality and form for publication:

Approved by the Dissertation Committee:

Ivan Deutsch , Chairperson

Grant Biedermann

Elohim Becerra

Victor Acosta

Nano-fabricated Atomic Waveguides for Inertial Measurements

by

Adrian Samuel Orozco

B.S., Physics, University of New Mexico, 2014
M.S., Physics, University of New Mexico, 2017

DISSERTATION

Submitted in Partial Fulfillment of the
Requirements for the Degree of

Doctor of Philosophy
Physics

The University of New Mexico

Albuquerque, New Mexico

May, 2022

Dedication

To my wonderful wife, amazing son, and extraordinary family, for their support and encouragement along this journey.

"The best that most of us can hope to achieve in physics is simply to misunderstand at a deeper level" – Wolfgang Pauli

Acknowledgments

There are many colleagues, family, and friends whose support helped make this work possible. I am thankful for the many great scientists at Sandia. Especially my advisor, Grant Biedermann (now at Oklahoma University), for his guidance and expertise in not only the field of atom interferometry but also his technical skills in cold atom physics. I enjoyed our discussions in the laboratory where his insights undoubtedly helped me become a better scientist.

I'd like to acknowledge several individuals with whom I worked in the lab. I started working in the lab with another graduate student Rustin Nourshargh, with whom I was lucky enough to work on his year long study abroad project. He helped guide me in the fundamentals of laser systems and optics and also embarked on the journey of constructing our first magneto-optical trap. William Kindel joined the project for a short time. His physical intuition was enlightening and our conversations were always illuminating. Christian Arrington provided a space to build our fiber puller and always was available and supportive whether it be in the context of the lab or outside of it. Jongmin Lee was a postdoc and later the principal investigator of the project that encompasses most of this work. I thank him for being an excellent mentor whose guidance and experience provided invaluable knowledge in the subject underlying this work.

Other Sandians that I would also like to thank from our group are Peter Schwindt, Yuan-Yu Jau, Amir Borna, Bethany Little, Michael Gehl, Nick Karl and Jonathan Sterk. I also overlapped with other graduate students Kaleb Cambell, Jonathan Bainbridge, and Matthew Chow. In particular, Matthew Chow and Bethany Little shared the laboratory and were always highly motivated and approachable. I would also like to thank professor Ivan Deutsch for his support and helping me meet the right folks at Sandia. Additionally, Ivan was always available to discuss lecture topics further and I enjoyed his engaging lectures.

I would like to thank my family. My parents, Elsa and Samuel, always supported my interests even when they varied from Fine Arts to Physics. Especially my mother, always motivating me to focus on a career that I was passionate about. I am also fortunate to have a twin brother who was a source of constant encouragement. My wife, Charla Orozco, who has been with me for most of this journey has provided unwaivering support, which kept me grounded especially during the most challenging times. Our son, Ezra Orozco, whose curiosity and love of climbing was always a great distraction when I was unhealthily fixated on a problem.

This work was funded by Sandia National Laboratories through the Laboratory Directed Research and Development program. I am thankful for this program, without which this work would not be possible.

Sandia National Laboratories is a multimission laboratory managed and operated by National Technology & Engineering Solutions of Sandia, LLC, a wholly owned

subsidiary of Honeywell International Inc., for the U.S. Department of Energy's National Nuclear Security Administration under contract DE-NA0003525.

Nano-fabricated Atomic Waveguides for Inertial Measurements

by

Adrian Samuel Orozco

B.S., Physics, University of New Mexico, 2014
M.S., Physics, University of New Mexico, 2017

PhD, Physics, University of New Mexico, 2022

Abstract

Atom-based inertial measurement systems can measure acceleration and rotation very precisely in the laboratory. The central element of these systems is atom interferometry where the phase shifts are sensitive to inertial forces experienced by the atom. This phenomenon has been used to make atom-based gravimeters, gradiometers, and gyroscopes. Recent effort has been made to make these systems more compact which require small size, light weight, and low power (SWaP). Nano-fabricated waveguides, such as photonic waveguides or optical nanofibers, offer a promising avenue to meet these goals. They have dimensions comparable to the guided light's wavelength producing a mode that not only propagates within the waveguide but also without in the form of an evanescent wave. This mode has a small area that is comparable to the atom's absorption cross section providing a highly efficient atom-light interaction. This property reduces the laser power required for efficient manipulation of atomic systems. In addition, photonic waveguides on silicon substrates provide the added benefit of further reducing the system size and being intrinsically scalable.

In this thesis, I detail two projects that aim to help progress the implementation of these platforms for use in inertial measurements.

Most of this thesis focuses on the nanofiber platform. I detail the construction of a fiber pulling rig used to fabricate tapered optical fibers with sub-micron diameters, so-called nanofibers. The fiber pulling rig has the capability of tailoring the fiber geometry for use as a 1-dimensional atom guide. Using a scanning-electron-microscope, we verify the accuracy and repeatability of nanofiber fabrication. In addition, we experimentally demonstrate trapping of cesium atoms around a nanofiber using a dual-color optical trap with magic wavelengths. This trap implements far-detuned laser beams that repel and attract atoms near the surface to produce a potential well where they can be trapped. We measure trap lifetimes up to 26 ms with an optical depth (OD) of 5.5 ± 0.3, corresponding to about 70 atoms. Additionally, the coherence properties of the trapped atoms are probed using microwave spectroscopy. I also discuss theoretical efforts in understanding the effects of driving Raman transitions with fiber guided fields.

Finally, I present an atom chip with a suspended optical rib waveguide extending across a cutout enabling an atomic cloud to be overlapped with the waveguide as a source for the trap. Simulations show that a dual-color trap with a trap depth of 350 μK can be generated using a total power of 6 mW. To demonstrate the chip designs are suitable for this type of trap, we experimentally test several waveguide designs and demonstrate power handling capabilities close to 30 mW before breaking. In addition, we measure the effect of the waveguide on the atom cloud by measuring the atom number when the atomic cloud is overlapped with the waveguide. Using fluorescence imaging, we measure the initial atom number in the cloud and find that it is reduced by an order of magnitude when overlapped with the waveguide.

Contents

List of Figures

Chapter 1

Introduction

A remarkable property of matter was postulated by Louis de Broglie about a century ago. He postulated that particles such as electrons, atoms, and molecules should exhibit wave-like behavior in addition to their particle behavior. The first demonstration of the wave behavior of matter was demonstrated by Davidson and Germer a few years later [2]. Forward to today, atom interferometers are some of the most precise measurement devices created, finding applications in measuring acceleration and rotation through the atom's dynamics. In these devices, optical pulses of light are used to separate, redirect, and recombine the atomic wavepackets. The sensitivity of the phase difference between matter waves that travel through distinct paths on acceleration and rotation has been used in a variety of applications such as gravimetry [3, 4, 5], gravity gradiometry [6, 7], and inertial navigation [8].

In an effort to exploit the high sensitivity of these sensors outside the laboratory, atom interferometers have been realized with high-data rate collection [9, 10, 11, 12] and in mobile platforms [13, 5]. Characterization of compact interferometers include small size, weight, and power consumption (SWaP) [14]. In this dissertation, we focus on the application of a nanofiber platform which intrinsically allows an efficient atom-light interaction, substantially reducing the power required for the manipulation of

the atom's dynamics required for atom interferometry.

1.1 Atom Interferometry

In 1991, Kasevich et al. demonstrated an atom interferometer that uses three light pulses to split, redirect, and recombine the atomic wavepackets [15]. Atoms were launched vertically upward in an atomic fountain configuration, and the three interferometric pulses were subsequently applied. The gravitational acceleration g experienced by the falling atoms was measured with a resolution of 3×10^{-8} in 1000 s of integration time [3]. The sensitivity of this interferometer is given by $\Delta\phi = 2kgT^2$, where ϕ is the phase difference between the arms of the interferometer, k is the wavevector of the light, and T is the time between the light pulses. In an effort to increase the sensitivity, 10 m tall towers have been realized [16, 17] and are under construction around the world [18] which can increase the total interrogation time to 2.3 s, splitting the atomic wavepacket 10's of centimeters [19].

Smaller compact interferometers have also been realized albeit are less sensitive due to the decrease in the interrogation times. However, to mitigate this effect, high data rate atom interferometers have been realized [9, 10, 11]. Reducing the size of atom interferometers inherently reduces the sensitivity by reducing the time T. However, other enhancements to the sensitivity include large momentum kicks [20] that can separate the wavepackets even further within the same time T, making smaller compact interferometers a viable option.

By decreasing the size of the apparatus, atom interferometers have now been realized outside the laboratory [14, 5]. For high dynamic range applications other systematic effects such as the Coriolis acceleration [21] can limit the accuracy of the device. This effect is due to the transverse motion of the atoms relative to the Raman beams. The Coriolis effect rotates the optics platform, and thus the Raman beams,

relative to the atomic cloud making the AI sensitive to rotations [22] via the Sagnac effect [23]. A 1D atomic guide can be used to keep the atoms and Raman beams aligned during the process. These guided atom interferometers have been realized using hollow photonic crystal fibers (PCF) with neutral atoms [24] and crossed dipole traps using Bose-Einstein condensates (BEC) [25]. In [24], atoms are guided into the hollow PCF which obstructs direct axis to atoms during the experiment in the radial direction. Furthermore, in [25] 4.5 watts of power was required for the trap, which isn't compatible for SWaP conditions. Optical nanofibers intrinsically provide a small mode area [26] that can reduce the power required to trap by orders of magnitude [27, 28]. In addition, atom's are trapped outside the surface of the optical fiber giving direct access to atoms for cooling using free space beams in addition to fiber guided fields [29, 30].

1.2 Atom Waveguides Using Evanescent Optical Fields

Driving coherent Raman transitions using an evanescent mode has many interesting features that result from the intensity gradient. Here, we focus on the nanofiber's fundamental mode as discussed in Chapter (2). First, since the Raman fields are both detuned from a high lying atomic state, a dipole force is applied to the atoms from each of these fields [31]. This force can change the trapping potential of the guided atoms with undesired changes in their dynamics. A technique that can be used to cancel this force involves using a single phase modulated beam [29]. This technique involves adjusting the sideband-to-carrier ratio and detuning to cancel the induced quadratic Stark shifts. Second, the decay of the evanescent field couples transverse trap states and internal states [32, 33].

In addition to the intensity gradient, the fundamental nanofiber mode has a com-

plex polarization field where all three components, E_x, E_y, and E_z can be nonzero. This is markedly different in free space experiments. In the nanofiber, polarization impurity has the potential to drive undesirable transitions, spreading out the atomic population across a ground state manifold which reduces contrast. Even with these complexities, we have found that driving the required interferometric pulses is possible utilizing Raman transitions.

1.3 Overview

In this thesis, I discuss research on the application of atom interferometry on nanofabricated devices with optically trapped atoms, with focus on an optical nanofiber. An optical nanofiber has proven to be a reliable platform for atom trapping and efficient atom-light interaction. However, due to the complexity of its fundamental mode special care is required when driving Raman transitions. In Chapter (2), I discuss the theory of electromagnetic modes that can exist in the nanofiber in general and for a specific geometry. In Chapter (3), I discuss the relevant atom-light interactions for atom trapping and the coherent manipulation of matter waves required for light pulse atom interferometry. Chapter (4) discusses the research related to building a nanofiber pulling rig to fabricate our own nanofibers in house. We have used these fibers to generate a dual color atom trap and studied their coherence properties using microwaves as discussed in Chapter (5). I also discuss a project where we designed and characterized an optical waveguide on a chip designed to trap atoms in the evanescent field in Chapter (6).

Chapter 2

Nanofiber Mode Theory

Optical glass fibers are used for communication networks worldwide. Their low loss of 0.2 dB/km (at 1550 nm light) allows the guiding of light over distances of 100's of kilometers [34]. For our purposes, this extraordinary property makes them attractive for guiding light close to and interfacing with an atomic ensemble. By fabricating an optical fiber with a diameter smaller than the guided light, an appreciable amount of power initially coupled into the fiber can extend beyond the waveguide [35]. This evanescent field has been used to trap atoms around the nanofiber [27, 28] and coherently drive atomic transitions [29]. In this thesis, we propose to use these modes to drive velocity sensitive coherent atomic transitions.

In this chapter, I discuss the theory describing the modes that propagate in step-index fibers. In the first section, Maxwell's equations are used to find the guided modes given a specific fiber geometry and guided wave properties. In the subsequent sections, the solution of the fundamental mode of a fiber with a radius smaller than or comparable to the guided light wavelength, the HE_{11} mode, is discussed. As will be shown, the field distribution around a nanofiber extends outside the fiber surface creating an interface for atom-light interactions which is further discussed in Chapter (3).

2.1 Guided Modes in a Step-Index Optical Fiber

Consider light that is guided in a higher index material called the core that is surrounded by a lower index material called the cladding. Because the index changes in a stepwise fashion from the outer material to the inner material, it is known as a step-index fiber (see Figure (2.1)). Due to this difference in index, light propagating in the core reflects rather than transmits at the interface between the two materials given that the angle of incidence is less than a critical angle $\theta_{crit} = \text{asin}(n_2/n_1)$, where n_1 is the index of the core and n_2 is the index of the cladding [36]. The step-index

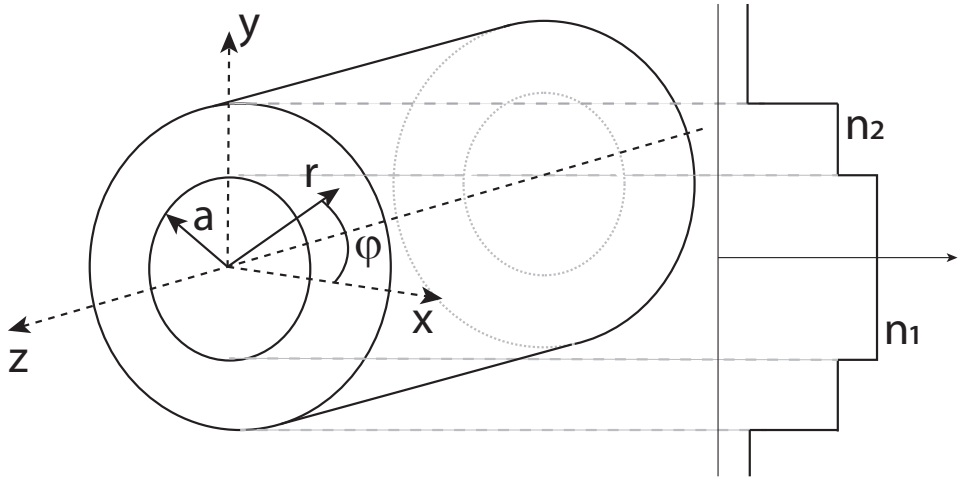

Figure 2.1: A step-index fiber has a core with index n_1 surrounded by the cladding of index n_2. The radius of the core is a. Here both the Cartesian and cylindrical coordinates are displayed.

optical fiber is modeled as a cylindrical rod composed of two concentric materials with index of refraction n_1 and n_2 as shown in Figure (2.1). Here n_1 refers to the index of the central material known as the core and n_2 is the index of the outer ma-

terial known as the cladding. To derive the modes supported by a step-index fiber, we follow the work of [37, 26, 38]. The procedure involves writing down Maxwell's equations for a dielectric with electric permittivity ϵ and permeability μ_0 for each layer. Because the glass is non-magnetic $\mu = \mu_0$ where μ_0 is the permeability of free space [38]. Maxwell's equations for an electric field $\vec{E}$ and magnetic field $\vec{H}$ are [26]

$$\begin{aligned} &\vec{\nabla} \times \vec{E} = -\mu_0 \frac{\partial \vec{H}}{\partial t}, \quad \vec{\nabla} \times \vec{H} = \epsilon \frac{\partial \vec{E}}{\partial t} \\ &\vec{\nabla} \cdot \epsilon \vec{E} = 0, \qquad\qquad \vec{\nabla} \cdot \vec{H} = 0 \end{aligned} \tag{2.1}$$

From this set of equations, and using the vector identity $\vec{\nabla} \times (\vec{\nabla} \times \vec{A}) = \vec{\nabla}(\vec{\nabla} \cdot \vec{A} - \vec{\nabla}^2 \vec{A})$, we can write the wave equation for the electric field

$$\vec{\nabla}^2 \vec{E} - \mu_0 \epsilon \frac{\partial^2 \vec{E}}{\partial t^2} = -\vec{\nabla} \left(\frac{1}{\epsilon} \vec{E} \cdot \vec{\nabla} \epsilon \right) \tag{2.2}$$

The gradient and Laplace operator written in cylindrical coordinates take the following form [39]

$$\begin{aligned} \vec{\nabla} &= \frac{\partial}{\partial r} \vec{r} + \frac{1}{r} \frac{\partial}{\partial \phi} \vec{\phi} + \frac{\partial}{\partial z} \vec{z} \\ \vec{\nabla}^2 &= \frac{\partial^2}{\partial r^2} + \frac{1}{r} \frac{\partial}{\partial r} + \frac{1}{r^2} \frac{\partial^2}{\partial \phi^2} + \frac{\partial^2}{\partial z^2} \end{aligned} \tag{2.3}$$

where we have introduced the cylindrical coordinates r, ϕ, and z as shown in Figure (2.1). The equation for $\vec{H}$ is obtained by replacing $\vec{E}$ with $\vec{H}$ in equation (2.2). Due to the cylindrical symmetry of the optical fiber, the axial components take on the following form

$$\begin{aligned} E_z(\vec{r}, t) &= E_z(r, \phi) \exp[i(\omega t - \beta z)] \\ H_z(\vec{r}, t) &= H_z(r, \phi) \exp[i(\omega t - \beta z)] \end{aligned} \tag{2.4}$$

The frequency of the field is denoted ω and β is the effective wave vector of the mode and is referred to as the propagation constant. This constant is unique to the different possible modes that can propagate in the fiber and is determined numerically as will be shown later.

Inserting equation (2.4) into Maxwell's equations (equation (2.1)), we get the following relationships between the radial and azimuthal components

$$\begin{aligned} E_r &= \frac{-i\beta}{\omega^2\mu_0\epsilon - \beta^2}\left(\frac{\partial}{\partial r}E_z + \frac{\omega\mu_0}{\beta}\frac{1}{r}\frac{\partial}{\partial\phi}H_z\right) \\ E_\phi &= \frac{-i\beta}{\omega^2\mu_0\epsilon - \beta^2}\left(\frac{1}{r}\frac{\partial}{\partial\phi}E_z - \frac{\omega\mu_0}{\beta}\frac{\partial}{\partial r}H_z\right) \\ H_r &= \frac{-i\beta}{\omega^2\mu_0\epsilon - \beta^2}\left(\frac{\partial}{\partial r}H_z - \frac{\omega\epsilon}{\beta}\frac{1}{r}\frac{\partial}{\partial\phi}E_z\right) \\ H_\phi &= \frac{-i\beta}{\omega^2\mu_0\epsilon - \beta^2}\left(\frac{1}{r}\frac{\partial}{\partial\phi}H_z + \frac{\omega\epsilon}{\beta}\frac{\partial}{\partial r}E_z\right) \end{aligned} \tag{2.5}$$

From this equation, we see that all the transverse components of the guided fields are solvable in terms of the axial components E_z and H_z. The equations describing the behavior of the axial components are obtained by inserting equation (2.4) into equation (2.2)

$$\begin{aligned} \left[\frac{\partial^2}{\partial r^2} + \frac{1}{r}\frac{\partial}{\partial r} + \frac{1}{r^2}\frac{\partial^2}{\partial\phi^2} + (k^2 - \beta^2)\right]E_z(\vec{r},t) = 0 \\ \left[\frac{\partial^2}{\partial r^2} + \frac{1}{r}\frac{\partial}{\partial r} + \frac{1}{r^2}\frac{\partial^2}{\partial\phi^2} + (k^2 - \beta^2)\right]H_z(\vec{r},t) = 0 \end{aligned} \tag{2.6}$$

where $\omega^2\mu_0\epsilon = k^2$ was obtained by using the relationship $c^2 = 1/\sqrt{\mu_0\epsilon_0}$. The solutions of these equations are obtained by using the separation of variables method to separate the radial and azimuthal behavior of the fields. The solutions are

$$\begin{aligned} E_z(\vec{r}) &= R(r)\exp(\pm i\phi) \\ H_z(\vec{r}) &= R(r)\exp(\pm i\phi) \end{aligned} \tag{2.7}$$

where the radial equation $R(r)$ is the solution for either the electric field or magnetic field axial component amplitude. It is obtained from the radial differential equation which has the form of a Bessel differential equation

$$\left[\frac{\partial^2}{\partial r^2} + \frac{1}{r}\frac{\partial}{\partial r} + (k^2 - \beta^2 - \frac{l^2}{r^2})\right]R(r) = 0 \tag{2.8}$$

The solutions for the radial wavefunctions are [40]

$$R(r) = c_1 J_l(hr) + c_2 Y_l(hr) \text{ for } k^2 - \beta^2 > 0, \text{ where } h^2 = k^2 - \beta^2 \tag{2.9}$$

$$R(r) = c_3 I_l(qr) + c_4 K_l(qr) \text{ for } k^2 - \beta^2 < 0, \text{ where } q^2 = \beta^2 - k^2 \tag{2.10}$$

The function $J_l(hr)$ is the Bessel function of the first kind, $Y_l(hr)$ is the Bessel function of the second kind, $I_l(hr)$ is the modified Bessel function of the first kind, and $K_l(hr)$ is the modified Bessel function of the second kind. Referring to Figure (2.2), we see that $Y_0(hr) \to \infty$ as $hr \to 0$. In order to have well-defined solutions at $hr = 0$, we set the coefficient for the functions $Y_l(hr)$ to zero. Similarly, $I_l(hr) \to \infty$ as $qr \to \infty$ is an nonphysical result since we expect the field mode to approach zero at a distance far away from the fiber. To find the amplitudes of the fields, we use the following ansatz for $r < a$

$$\begin{bmatrix} E_z(\vec{r},t) \\ H_z(\vec{r},t) \end{bmatrix} = \begin{bmatrix} A \\ B \end{bmatrix} J_l(hr)\exp(i(\omega t \pm l\phi - \beta z)) \tag{2.11}$$

and the ansatz for $r > a$

$$\begin{bmatrix} E_z(\vec{r},t) \\ H_z(\vec{r},t) \end{bmatrix} = \begin{bmatrix} C \\ D \end{bmatrix} K_l(qr)\exp(i(\omega t \pm l\phi - \beta z)) \tag{2.12}$$

Inserting these ansatz into the equations (2.5), we get several expressions for the amplitudes in terms of the constants A, B, C, and D.

The field equations for $r < a$ are

$$\begin{aligned} E_r &= \frac{-i\beta}{h^2}\left[AhJ_l'(hr) + \frac{i\omega\mu_0(\pm l)}{\beta r}BJ_l(hr)\right]\exp[i(\omega t \pm l\phi - \beta z)] \\ E_\phi &= \frac{-i\beta}{h^2}\left[\frac{i(\pm l)}{r}AJ_l(hr) - \frac{\omega\mu_0}{\beta}BhJ_l'(hr)\right]\exp[i(\omega t \pm l\phi - \beta z)] \\ E_z &= AJ_l(hr)\exp[i(\omega t \pm l\phi - \beta z)] \end{aligned} \tag{2.13}$$

$$\begin{aligned} H_r &= \frac{-i\beta}{h^2}\left[BhJ_l'(hr) - \frac{i\omega\epsilon n_1(\pm l)}{\beta r}AJ_l(hr)\right]\exp[i(\omega t \pm l\phi - \beta z)] \\ H_\phi &= \frac{-i\beta}{h^2}\left[\frac{i(\pm l)}{r}BJ_l(hr) + \frac{\omega\epsilon n_1}{\beta}AhJ_l'(hr)\right]\exp[i(\omega t \pm l\phi - \beta z)] \\ H_z &= BJ_l(hr)\exp[i(\omega t \pm l\phi - \beta z)] \end{aligned} \tag{2.14}$$

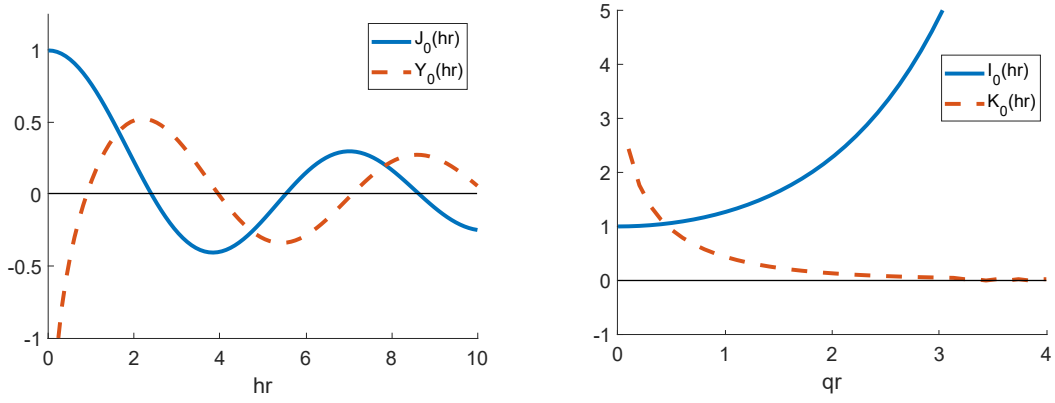

Figure 2.2: The Bessel functions are plotted above for $n = 0$. The Bessel function of the second kind diverges for $hr \to 0$. The modified Bessel function of the first kind diverges for $hr \to \infty$.

For $r > a$

$$\begin{aligned} E_r &= \frac{i\beta}{q^2}\left[CqK_l'(qr) + \frac{i\omega\mu_0(\pm l)}{\beta r}DK_l(qr)\right]\exp[i(\omega t \pm l\phi - \beta z)] \\ E_\phi &= \frac{i\beta}{q^2}\left[\frac{i(\pm l)}{r}CK_l(qr) - \frac{\omega\mu_0}{\beta}DqK_l'(qr)\right]\exp[i(\omega t \pm l\phi - \beta z)] \\ E_z &= CK_l(qr)\exp[i(\omega t \pm l\phi - \beta z)] \end{aligned} \tag{2.15}$$

$$\begin{aligned} H_r &= \frac{i\beta}{q^2}\left[DqK_l'(qr) - \frac{i\omega\epsilon n_2(\pm l)}{\beta r}CK_l(qr)\right]\exp[i(\omega t \pm l\phi - \beta z)] \\ H_\phi &= \frac{i\beta}{q^2}\left[\frac{i(\pm l)}{r}DK_l(qr) + \frac{\omega\epsilon n_2}{\beta}CqK_l'(qr)\right]\exp[i(\omega t \pm l\phi - \beta z)] \\ H_z &= DK_l(qr)\exp[i(\omega t \pm l\phi - \beta z)] \end{aligned} \tag{2.16}$$

The primes on the Bessel functions indicate derivatives with respect to their arguments such as hr or qr. To solve for the constants A, B, C, and D, we impose the boundary conditions that the tangential components (E_z, E_ϕ, H_z, and H_ϕ) to the dielectric surface at $r = a$ have to be continuous together with equations (2.13)-(2.16).

$$
\begin{aligned}
AJ_l(ha) - CK_l(qa) &= 0 \\
A\left[\frac{i(\pm l)}{ah^2}J_l(ha)\right] + B\left[-\frac{\omega\mu_0}{h\beta}J_l'(ha)\right] + C\left[\frac{i(\pm l)}{aq^2}K_l(qa)\right] + D\left[-\frac{\omega\mu_0}{q\beta}K_l'(qa)\right] &= 0 \\
BJ_l(ha) - DK_l(qa) &= 0 \\
A\left[\frac{\omega\epsilon}{ah^2}J_l(ha)\right] + B\left[-\frac{\omega\mu_0}{h\beta}J_l'(ha)\right] + C\left[\frac{i(\pm l)}{aq^2}K_l(qa)\right] + D\left[-\frac{\omega\mu_0}{q\beta}K_l'(qa)\right] &= 0
\end{aligned}
\tag{2.17}
$$

If the determinant of the coefficients of the constants A, B, C, and D in equation (2.17) is zero, then we get a non-trivial solution [38]. This requirement results in the following equation, from which the propagation constant β can be found numerically

$$
\left(\frac{J_l'(ha)}{haJ_l(ha)} + \frac{K_l'(qa)}{qaK_l(qa)}\right)\left(\frac{n_1^2J_l'(ha)}{haJ_l(ha)} + \frac{n_2^2K_l'(qa)}{qaK_l(qa)}\right) = l^2\left[\frac{1}{(ha)^2} + \frac{1}{(qa)^2}\right]^2\left(\frac{\beta}{k_0}\right)^2 \tag{2.18}
$$

Due to the quadratic dependence on $J_l'(ha)/haJ_l(ha)$ there are two possible solutions that satisfy equation (2.18) corresponding to the two roots of the resulting quadratic equation. To write this equation in a simpler form, we can use the following relationships for the derivatives of the Bessel functions

$$
\begin{aligned}
J_l'(x) &= J_{l-1}(x) - \frac{l}{x}J_l(x) \\
J_l'(x) &= -J_{l+1}(x) + \frac{l}{x}J_l(x) \\
K_l'(x) &= -\frac{1}{2}[K_{l-1}(x) + K_{l+1}(x)]
\end{aligned}
\tag{2.19}
$$

Inserting the above relationships in equation (2.18) and rearranging results in the following two possible solutions for β

$$
\begin{aligned}
\frac{J_{l+1}(ha)}{haJ_l(ha)} &= \frac{(n_1^2+n_2^2)}{2n_1^2}\frac{K_l'(qa)}{qaK_l(qa)} + \left(\frac{1}{(ha)^2} - R\right) \\
\frac{J_{l-1}(ha)}{haJ_l(ha)} &= -\frac{(n_1^2+n_2^2)}{2n_1^2}\frac{K_l'(qa)}{qaK_l(qa)} + \left(\frac{1}{(ha)^2} - R\right)
\end{aligned}
\tag{2.20}
$$

where

$$R = \left[\left(\frac{n_1^2 - n_2^2}{2n_1^2} \right)^2 \left(\frac{K_l'(qa)}{qaK_l(qa)} \right)^2 + \left(\frac{l\beta}{n1k_0} \right)^2 \left(\frac{1}{(qa)^2} + \frac{1}{(ha)^2} \right)^2 \right]^{1/2} \tag{2.21}$$

$$\beta = \sqrt{n_1^2 k_0^2 - \left(\frac{(ha)_{cross}}{a} \right)^2} \tag{2.22}$$

The first set of solutions corresponding to the upper equation in equation (2.20) are designated EH modes and for the lower equation HE modes. These modes will generally have nonzero E_z, H_z, E_ϕ, H_ϕ, E_r, and H_r components. We can use a graphical method of plotting the left-hand side (LHS) and the right-hand side (RHS) of equation (2.20) to determine β. An example is shown in Figure (2.3) for $l = 1$. The LHS is plotted in blue and the RHS is plotted in red. The grey lines indicate the zeros of the Bessel function of the first kind, $J_l(ha)$. These vertical asymptotes appear due to dividing by $J_1(ha)$. The intersection of the LHS and RHS determines β. The vertical asymptote of the right-hand side is determined by a parameter called the V number (dotted black line). Note that in this case, Figure (2.3)(a), there are only three possible solutions. In Figure (2.3)(b), there are two possible solutions. The number of possible solutions is determined by the V number, defined by

$$V = ak\sqrt{n_1^2 - n_2^2} \tag{2.23}$$

where a is the radius of the fiber, n_1 is the core index, n_2 is the cladding index, and $k = \frac{2\pi}{\lambda}$ is the free-space wavenumber with wavelength λ. From equation (2.23), we see that the number of modes that are supported by the fiber depends on the geometry of the fiber and the wavelength of the guided light. For instance, below $V = 2.405$ only one mode can exist in the fiber as shown in Figure (2.4). This is known as the fundamental mode and, due to its importance in our experiments, its properties are studied in more detail in the next section. The effective index of the mode is related to the effective wave vector by $n_{\text{eff}} = \beta/k_0$ where k_0 is the wave

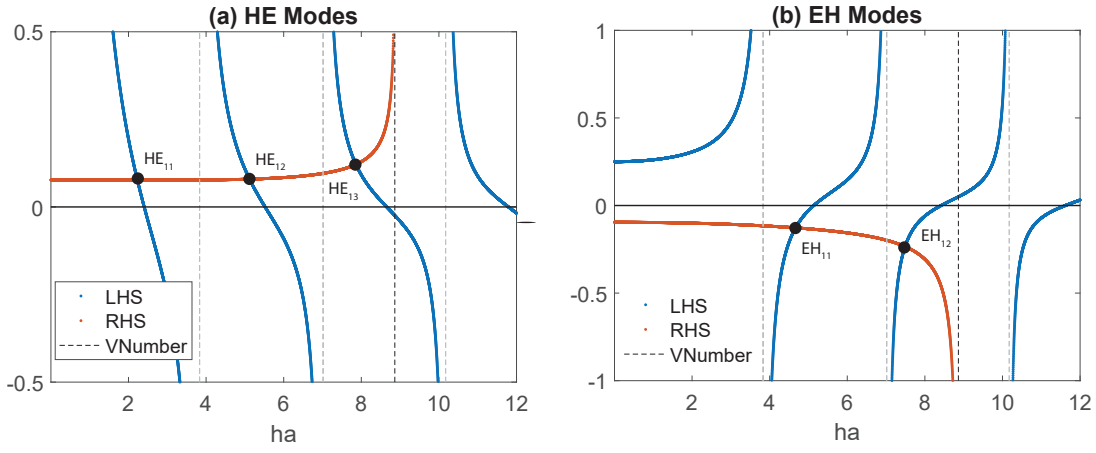

Figure 2.3: Plot showing a graphical solution to the propagation constants for the HE and EH modes. The black dashed vertical line is the V number and the gray lines are the zeros of the corresponding Bessel function.

number of the mode in free space. Figure (2.4) displays the effective wave number as a function of the V number. The cuttoff at V = 2.405 is shown as a vertical dashed line.

After determining β, we can determine the relationships between the coefficients introduced in equation (2.17). The relationship between these coefficients is

$$\begin{aligned}
\frac{C}{A} &= \frac{J_l(ha)}{K_l(q)} \\
\frac{B}{A} &= \frac{i\beta(\pm l)}{\omega\mu_0}\left(\frac{1}{(ha)^2}+\frac{1}{(qa)^2}\right)\left(\frac{J_l'(ha)}{haJ_l(ha)}+\frac{K_l'(qa)}{qaK_l(qa)}\right) \\
\frac{D}{A} &= \frac{C}{A}\frac{B}{A^2}
\end{aligned} \tag{2.24}$$

There are four constants (A, B, C, and D) and three equations. Another equation is required to uniquely solve for all of the constants. The fourth equation required is the total power of the field and is calculated by using the time-averaged Poynting vector $\langle\vec{S}\rangle = \mathrm{Re}(\vec{E}\times\vec{H}^*)/2$. We are interested in the power propagating along the fiber axis. This is given by the z-component of the Poynting vector. The energy flux

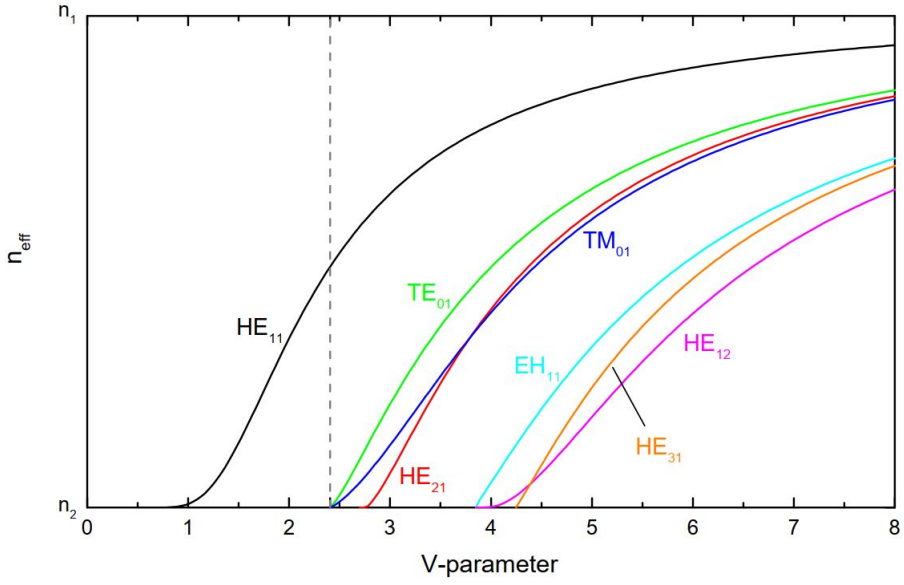

Figure 2.4: The effective index $n_{\text{eff}} = \beta/k_0$ of the guided mode is dependent on the fiber radius a and guided light of wavelength λ. The V-number is shown as a vertical line. See text for more details. This image has been borrowed from [1].

along the fiber axis (z direction) is

$$\begin{aligned} P =& P_{in} + P_{out} \\ =& \int_0^a \int_0^{2\pi} P_z r dr d\phi + \int_a^\infty \int_0^{2\pi} P_z r dr d\phi \end{aligned} \tag{2.25}$$

where $P_z = \langle \vec{S} \rangle \cdot \hat{z}$.

In the next section, the theory developed here will be used to calculate the fundamental mode of an optical nanofiber.

2.2 Fundamental HE_{11} Nanofiber Mode

The theory in the previous section indicated that for a small enough fiber radius, only one mode could be supported by the fiber geometry. In this section, we describe

this fundamental mode designated HE_{11}. The radius of the fiber is smaller than or comparable to the wavelength of the guided light and, due to being on the nanometer scale, is designated a nanofiber.

The power in the fundamental mode is distributed not only within the fiber but also extends beyond its surface in the form of an evanescent wave. The total power is $P = P_{in} + P_{out}$. Setting $l = 1$ and evaluating the integrals in equation (2.25), the normalization constant can be obtained and is equal to

$$A = \sqrt{\frac{P\beta}{a^2\pi\omega\epsilon_0}} \left(D^{\text{in}} + D^{\text{out}}\right)^{-1/2} \tag{2.26}$$

where

$$\begin{aligned} D^{\text{in}} = n_1^2 \frac{q^2 K_1^2(qa)}{h^2 J_1^2(ha)} \Big\{ & (1-s)(1-s_1)\left[J_0^2(ha) + J_1^2(ha)\right] \\ & +(1+s)(1+s_1)\left[J_2^2(ha) - J_1(ha)J_3(ha)\right] \Big\} \end{aligned} \tag{2.27}$$

$$\begin{aligned} D^{\text{out}} = n_2^2 \Big\{ & (1-s)(1-s_2)\left[K_1^2(qa) - K_0^2(qa)\right] \\ & +(1+s)(1+s_2)\left[K_1(qa)K_3(qa) - K_2^2(qa)\right] \Big\} \end{aligned} \tag{2.28}$$

with

$$\begin{aligned} s &= \left(\frac{1}{(qa)^2} + \frac{1}{(ha)^2}\right) \left(\frac{J_1'(ha)}{haJ_1(ha)} + \frac{K_1'(qa)}{qaK_1(qa)}\right)^{-1} \\ s_1 &= \frac{\beta^2}{k_0 n_1^2} s \\ s_2 &= \frac{\beta^2}{k_0^2 n_2^2} s \end{aligned} \tag{2.29}$$

Now having solved for the normalization constant A, the electromagnetic fields for the HE_{11} can be written. However, before writing them down it is instructive to mention that in the derivation in section (2.1) it was assumed that the electromagnetic wave was traveling in the $+z$ direction but it can also propagate in the $-z$ direction. In doing so, we not only have to change the sign of the phase factor $e^{i\beta z}$ but also the sign of the z component of the field. Generalizing the mode to take into account

its propagation direction is important when considering counter-propagating fields in the nanofiber which would be required for lattice based traps [27, 28] or driving velocity sensitive Raman transitions [41] which are required for atom interferometry. To take this into account, we can introduce an index $f = 1$ for $+z$ propagation and $f = -1$ for $-z$ propagation [42]. A quasilinearly polarized field can then be written as

$$\begin{aligned}\vec{E}^{lin}(r,\phi,z) = A\sqrt{2}\left(e_r\cos(\phi-\phi_0)\vec{r} + ie_\phi\sin(\phi-\phi_0)\vec{\phi} + fe_z\cos(\phi-\phi_0)\vec{z}\right) \\ \times \exp(if\beta z - i\omega t)\end{aligned} \tag{2.30}$$

where $\vec{r} = \cos(\phi)\vec{x} + \sin(\phi)\vec{y}$, $\phi = -\sin(\phi)\vec{x} + \cos(\phi)\vec{y}$, and $\vec{z}$ are the unit basis vector for cylindrical coordinates in terms of the Cartesian unit vectors $\vec{x}$, $\vec{y}$, and $\vec{z}$. The direction of polarization is determined by the parameter ϕ_0. This constant is the angle of the polarization vector with respect to the positive x-axis. For $\phi_0 = 0$ we have x polarized light and for $\phi_0 = \pi/2$ we have y polarized light. The circularly polarized field is also included here for completeness.

$$\vec{E}^{circ}(r,\phi,z) = A\left(e_r\vec{r} + lie_\phi\vec{\phi} + fe_z\vec{z}\right)\exp(if\beta z - i\omega t) \tag{2.31}$$

where the parameter $l = +1$ for right-hand circular polarization and $l = -1$ for left-hand circular polarization referenced to the positive direction of the z axis. The mode profile functions $e_r, e_\phi,$ and e_z have are given for $r < a$ by

$$\begin{aligned} e_r &= i\frac{qK_1(qa)}{hJ_1(ha)}\left[(1-s)J_0(hr) - (1+s)J_2(hr)\right] \\ e_\phi &= -\frac{qK_1(qa)}{hJ_1(ha)}\left[(1-s)J_0(hr) + (1+s)J_2(hr)\right] \\ e_z &= \frac{2q}{\beta}\frac{K_1(qa)}{J_1(ha)}J_1(hr) \end{aligned} \tag{2.32}$$

and

$$\begin{aligned} h_r &= \frac{\omega\epsilon_0 n_1^2 q}{h\beta}\frac{K_1(qa)}{J_1(ha)}\left[(1-s)J_0(hr) + (1+s)J_2(hr)\right] \\ h_\phi &= i\frac{\omega\epsilon_0 n_1^2 q}{h\beta}\frac{qK_1(qa)}{hJ_1(ha)}\left[(1-s)J_0(hr) - (1+s)J_2(hr)\right] \\ h_z &= i\frac{2q}{\omega\mu_0}s\frac{K_1(qa)}{J_1(ha)}J_1(hr) \end{aligned} \tag{2.33}$$

For $r > a$

$$\begin{aligned} e_r &= i\left[(1-s)K_0(qr) + (1+s)J_2(qr)\right] \\ e_\phi &= -\left[(1-s)K_0(qr) - (1+s)K_2(qr)\right] \\ e_z &= \frac{2q}{\beta}K_1(qr) \end{aligned} \tag{2.34}$$

and

$$\begin{aligned} h_r &= \frac{\omega\epsilon_0 n_2^2}{\beta}\left[(1-s_2)K_0(qr) - (1+s_2)K_2(qr)\right] \\ h_\phi &= i\frac{\omega\epsilon_0 n_2^2}{\beta}\left[(1-s_2)K_0(qr) + (1+s_2)K_2(qr)\right] \\ h_z &= i\frac{2q}{\omega\mu_0}sK_1(qr) \end{aligned} \tag{2.35}$$

Figure (2.5) displays normalized intensity plots for the components of equation (2.30) for $\phi_0 = 0$ (x quasipolarized field). Each intensity profile was normalized to the total intensity at $r = a$. The plots were calculated using $|E_i(r)|^2/|\vec{E}(r = a)|^2$ where $i = x$, y, or z. Figure (2.5)(a) shows the intensity of the x-component of the field. The evanescent tail of the field has most of its energy along the polarization direction (along x). Another important feature to note is the strength of the z-component. In nanofiber based atom traps (discussed further in Chapter (3)), atoms are trapped in the evanescent field. The presence of the z-component induces light shifts that are similar to the Zeeman shifts induced by a static-magnetic field [43, 44].

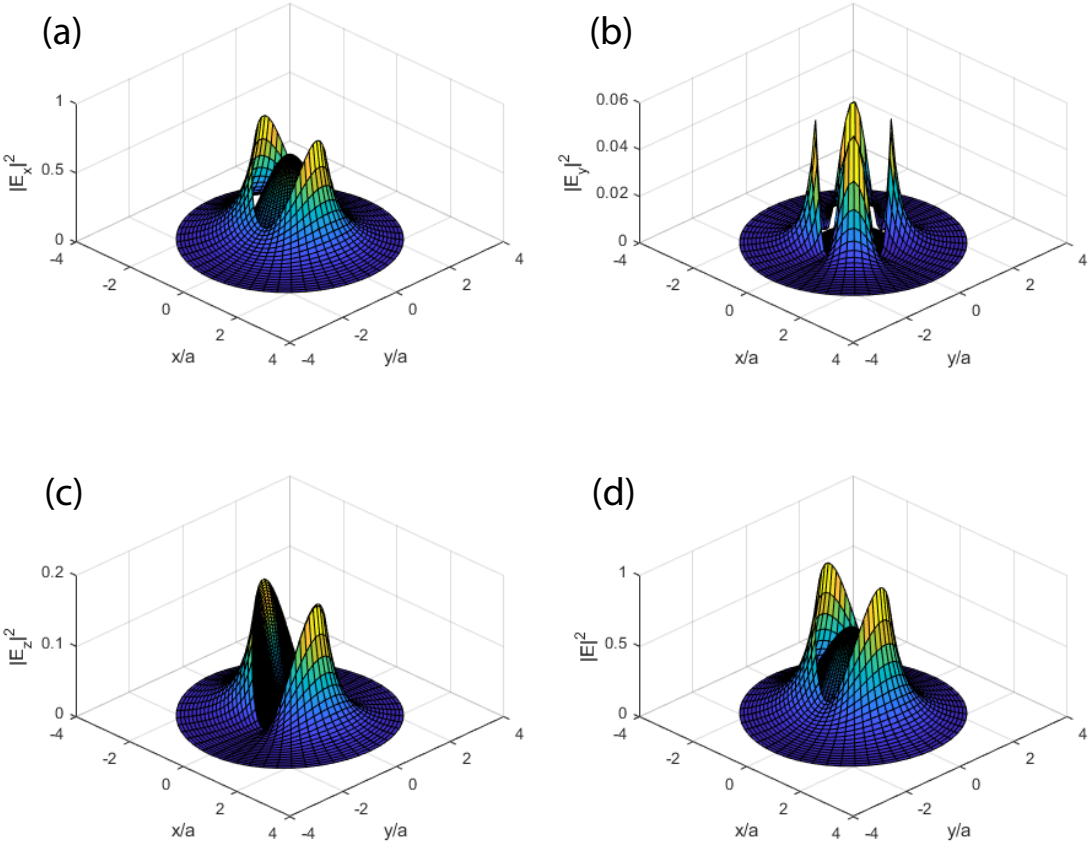

Figure 2.5: Intensity plots of the electric field components normalized to the total electric field at $r = a$.

Chapter 3

Atom-Light Interaction

All optical-based atom surface traps for use in atom interferometry need to have long trap lifetimes and coherence times. Far off resonant optical dipole traps (FORTs) are attractive because, due to their large detuning, dissipative effects are negligible and the interaction is conservative [45, 46]. This conservative potential can be made spatially varying to create a potential minimum or maximum [47] and has been used to trap atoms in optical tweezers [45, 48], hollow beams [49], near surfaces [27, 28], and reflect atoms from surfaces [50, 51]. FORTs have been realized with atom trap storage times of seconds to hours [52, 53]. Although, for nanofiber-based traps [27, 28] the lifetime has been limited to 10's of milliseconds, cooling has been able to extend the lifetime substantially [30], presumably limited by fiber vibrations [54, 55]. This requirement is crucial for guided atom interferometry as increasing the interferometric time also increases its sensitivity to inertial forces.

In this chapter, I discuss the atom-light interaction and present the theory underlying a dual-color atom nanofiber trap. In addition, I give an overview of the theory of Raman transitions and the effects that arise when driving such transitions using nanofiber-guided Raman beams interacting with trapped atoms around the nanofiber. The final section discusses the application of Raman transitions to light

pulse atom interferometry.

3.1 AC Stark Shift

The interaction of an atom with a far off resonant light field results in a light shift. Here the semi-classical formalism is used to describe this interaction where the field is a classical field and the atom's energy levels are quantized. This discussion closely follows [43, 26]. Consider the interaction of an atom with a classical light field of the form

$$\vec{E}(\vec{r},t) = \frac{1}{2}E\vec{\epsilon}e^{-i\omega t} + c.c \tag{3.1}$$

where E is the amplitude, $\vec{\epsilon}$ is the polarization, ω is the angular frequency, and c.c stands for complex conjugate. In the dipole approximation, the interaction of the atom with the light field can be described by

$$\begin{aligned}\hat{V} &= -\vec{\hat{d}}\cdot\vec{E} \\ &= -\frac{1}{2}E\vec{\hat{d}}\cdot\vec{\epsilon}e^{-i\omega t} + H.c \\ &= \hat{V}_{-}e^{-i\omega t} + \hat{V}_{+}e^{i\omega t}\end{aligned} \tag{3.2}$$

where $\hat{V}_{-} = -\frac{1}{2}E\vec{\hat{d}}\cdot\vec{\epsilon}$ and H.c. represents the Hermitian conjugate. Using second order perturbation theory, the AC Stark shift of a non-degenerate energy level $|g\rangle$ can be written as [56, 57, 43]

$$\begin{aligned}\delta E_g = &\frac{|\vec{E}|^2}{4}\sum_m \frac{\langle g|\,\vec{\epsilon}^{*}\cdot\vec{\hat{d}}\,|m\rangle\,\langle m|\,\vec{\epsilon}\cdot\vec{\hat{d}}\,|g\rangle}{E_g - E_m - \hbar\omega} \\ &+ \frac{|\vec{E}|^2}{4}\sum_m \frac{\langle g|\,\vec{\epsilon}\cdot\vec{\hat{d}}\,|m\rangle\,\langle m|\,\vec{\epsilon}^{*}\cdot\vec{\hat{d}}\,|g\rangle}{E_g - E_m + \hbar\omega}\end{aligned} \tag{3.3}$$

where the sum is over the eigenstates $|m\rangle$ of the unperturbed system. When considering cesium these states correspond to the hyperfine energy states, i.e. $|m\rangle =$

$|nJFM_F\rangle$ and the sum is over all parameters n, J, F, and M_F. The light shift in equation (3.3) can be written as the expectation value $\delta E_g = \langle g| \hat{V}^{EE} |g\rangle$ where the operator $\hat{V}^{EE}$ can be written in the spherical bases [57, 43]

$$\hat{V}^{EE} = \frac{|\vec{E}|^2}{4} \sum_{K=0}^{2} \{\vec{\epsilon}^* \otimes \vec{\epsilon}\}_K \cdot [\{\vec{\hat{d}} \otimes \mathcal{R}(\omega)\vec{\hat{d}}\}_K + (-1)^K \{\vec{\hat{d}} \otimes \mathcal{R}(-\omega)\vec{\hat{d}}\}_K] \tag{3.4}$$

and is decomposable in terms of the scalar ($K = 0$), vector ($K = 1$), and tensor ($K = 2$) components. This equation can then be written in terms of the dynamic polarizability of the atom $\alpha(\omega)$ (see reference [43] for details). In terms of the hyperfine states of the nJ manifold, the operator can be expressed as

$$\hat{V}^{EE} = \sum_{FMF'M'} V^{EE}_{FMF'M'} |(nJ)FM\rangle\langle(nJ)F'M'| \tag{3.5}$$

where the matrix elements are

$$\begin{aligned} \hat{V}^{EE}_{FMF'M'} = &\frac{1}{4}|E|^2 \sum_{\substack{K=0,1,2 \\ q=-K,\ldots K}} \alpha^{(K)}_{nJ}(\omega) \{\vec{u}^* \otimes \vec{u}\}_{Kq} \\ &\times (-1)^{J+I+K+q-M} \sqrt{(2F+1)(2F'+1)} \\ &\times \begin{pmatrix} F & K & F' \\ M & q & -M' \end{pmatrix} \begin{Bmatrix} F & K & F' \\ J & I & J \end{Bmatrix} \end{aligned} \tag{3.6}$$

The scalar ($K = 0$), vector ($K = 1$), and tensor ($K = 2$) components of the polarizability are

$$\begin{aligned} \alpha^{(K)}_{nJ}(\omega) = &(-1)^{(K+J+1)} \sqrt{2K+1} \\ &\times \sum_{n'J'} (-1)^{J'} \begin{Bmatrix} 1 & K & 1 \\ J & J' & J \end{Bmatrix} |\langle n'J'| |\mathbf{d}| |\mathbf{nJ}\rangle|^{\mathbf{2}} \\ &\times \frac{1}{\hbar} \mathrm{Re}\left(\frac{1}{\omega_{n'J'nJ} - \omega} + \frac{(-1)^K}{\omega_{n'J'nJ} + \omega} \right) \end{aligned} \tag{3.7}$$

The potential can be further written as

$$\begin{aligned} \hat{V}^{EE} = &-\frac{|\vec{E}|^2}{4} \left\{ \alpha^s_{nJ} - i\alpha^v_{nJ} \frac{[\vec{\epsilon}^* \times \vec{\epsilon}] \cdot \vec{J}}{2J} \right. \\ &\left. + \alpha^T_{nJ} \frac{3[(\vec{\epsilon}^* \cdot \vec{\hat{J}})(\vec{\epsilon} \cdot \vec{\hat{J}}) + (\vec{\epsilon} \cdot \vec{\hat{J}})(\vec{\epsilon}^* \cdot \vec{\hat{J}})] - 2J^2}{2J(2J+1)} \right\} \end{aligned} \tag{3.8}$$

where the reduced polarizability components are given by

$$\begin{aligned}\alpha^{s}_{nJ} &= \frac{1}{\sqrt{3(2J+1)}}\alpha^{(0)}_{nJ} \\ \alpha^{v}_{nJ} &= -\sqrt{\frac{2J}{(J+1)(2J+1)}}\alpha^{(0)}_{nJ} \\ \alpha^{T}_{nJ} &= -\sqrt{\frac{2J(2J-1)}{3(J+1)(2J+1)(2J+3)}}\alpha^{(0)}_{nJ}\end{aligned} \tag{3.9}$$

These components effect the light shifts in different ways. The scalar component affects all hyperfine multiplets in the same way, such that all the sub-levels experience a global light shift and is proportional to the intensity of the field $I \propto |\vec{E}^2|$. The vector part of the polarizability shifts the sub-levels of a hyperfine state linearly with a value dependent on the magnetic quantum projection number, M_F and is dependent on the degree of ellipticity of the polarization of the light [57]. The tensor component is zero when $J = 1/2$ due to the Wigner 6j symbol being zero for $J = 1/2$ and $K = 2$. Thus, this term is zero for the ground state $6S_{1/2}$ and excited state $6P_{1/2}$ of cesium so that only the scalar and vector shifts participate.

In Figure (3.1) and Figure (3.2), the polarizability for the states $6S_{1/2}$ and $6P_{3/2}$ of cesium are shown. In Figure (3.1) a plot of the two relevant terms of the polarizability, scalar and vector, are plotted for the $6S_{1/2}$ state. To make these plots, coupling to higher n states were included by using the tables provided in [43]. The black vertical lines indicate the nanofiber trapping laser's wavelength's of 685 nm and 937 nm used in this work and the gray dotted lines are the two resonances at 852 nm and 895 nm, the D1 and D2 lines respectively. From these plots, we can discern the light shift of the states and, comparing these shifts, we can find wavelengths where the scalar light shifts are the same for both states resulting in a zero differential light shifts which are known as magic wavelengths. More specifically, the magic wavelengths for cesium are 686.3 nm and 935.2 nm [58, 43] for the D2 transition. In our experiment, we use 937 nm and 685 nm which are near the magic wavelengths.

Another interesting feature, is the region between the D1 and D2 resonances. At

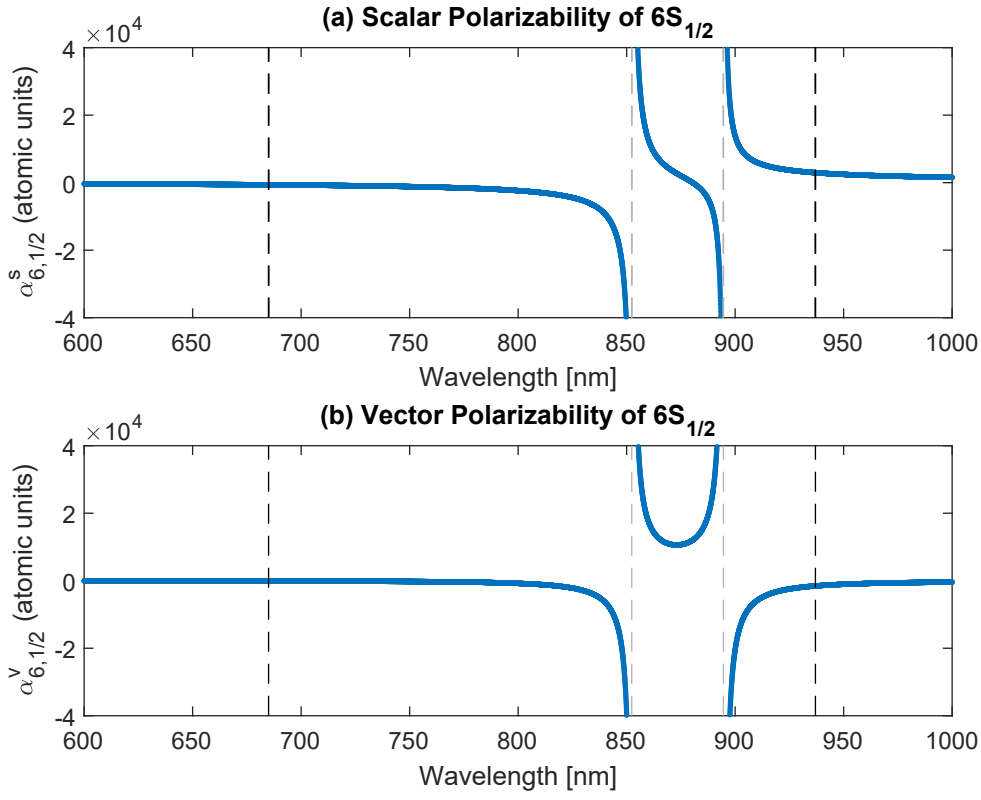

Figure 3.1: The scalar and vector polarizabilities of cesium for the the $6S_{1/2}$ state.

about 880 nm the scalar polarizability is zero and the vector polarizability is far from zero. This is called a tune-out wavelength [59]. At this wavelength, the vector light shift can be used to manipulate the internal states of nanofiber trapped atoms on different sides of the fiber even when they are initially prepared in the same state [60].

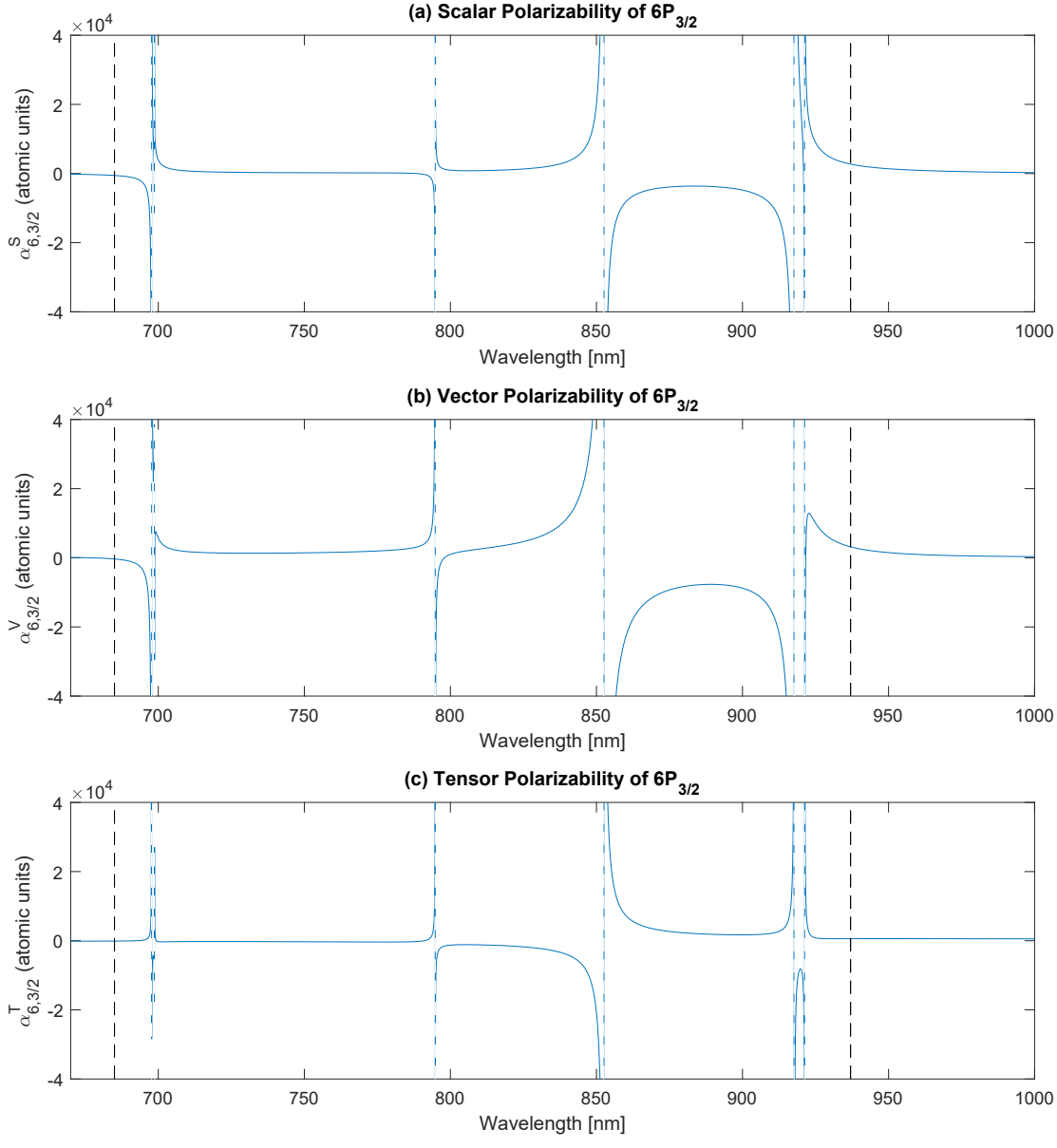

Figure 3.2: The scalar, vector, and tensor polarizabilities of cesium for the $6P_{3/2}$ state.

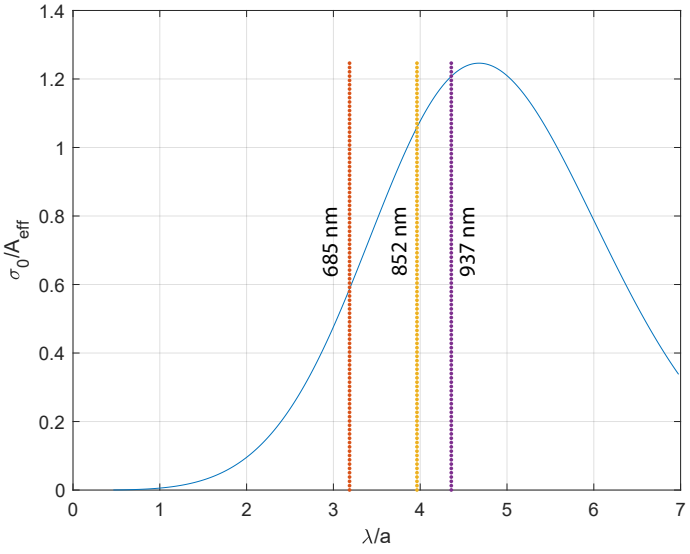

Figure 3.3: The ratio of the atom's resonant cross section, $\sigma_0 = 3\lambda^2/2\pi$, and the effective area of the evanescent field, $A_{\text{eff}} = P/I(r = a)$, as function of the ratio coupled wavelength, λ and fiber radius, $a = 215$ nm. The vertical lines show various wavelengths used in our experimental realization of the nanofiber trap.

3.2 Atom-Light Interaction Efficiency

The most impressive feature of the nanofiber for atom interferometry is the low power required for trapping and atom manipulation. The reduction in power is due to the small effective mode area of the evanescent mode defined by $A_{\text{eff}} = P/I(r = a)$, where P is the total field power and $I(r = a)$ is the field intensity at the fiber surface. This area is comparable to the atom's resonant absorption cross section $\sigma_0 = 3\lambda^2/2\pi$ [47] and is on the order of μm^2. In Figure (3.3), we plot the ratio σ_0/A_{eff} as a function of the ratio of the guided beam's wavelength, λ, and the radius of the nanofiber, a. As can be seen, there is a peak at around $\lambda/a = 4.5$ indicating that for a fixed radius λ can be chosen to optimize the interaction efficiency. For reference, the plot indicates the two trapping wavelengths 685 nm and 937 nm and the absorption probe and Raman field wavelength 852 nm. For our experiment, we chose the fiber radius to

optimize the attractive field interaction for the 937 nm trapping laser.

3.3 Trapping Potential

Trapping neutral atoms in the vicinity of the nanofiber surface is possible due to the spatial variation of the evanescent field [31, 27, 28]. Our nanofiber trap makes use of two co-propagating trapping fields, one at 685 nm and the other at 937 nm with parallel quasi-linear polarization. The ground state potential can be calculated by

$$U(r,\phi,z) = -\frac{1}{4}\left(\alpha_g^s(\omega_{\text{red}})E_{\text{red}}^2 + \alpha_g^s(\omega_{\text{blue}})E_{\text{blue}}^2\right) \tag{3.10}$$

The 685 nm field is blue detuned field with respect to the $6P_{3/2}$ transition. The scalar polarizability for this wavelength is negative as shown in Figure (3.1)(a) and the resulting potential will repel atoms from the surface. This repulsive force is indicated by the positive potential shown by the blue curve in Figure (3.4)(a). Conversely, the 937 nm laser field is red detuned with respect to the $6P_{3/2}$ state and will attract atoms to the surface as shown by the red trace in Figure (3.4)(b) which exhibits a negative potential. The total potential, calculated using equation (3.10), is shown as a black curve in Figure (3.4)(a). By varying the relative powers of each of these two fields, a potential minimum can be attained. For this plot, the following parameters were used, $P_{\text{blue}} = 25$ mW, $P_{\text{red}} = 2.5$ mW, a = 215 nm. The calculated trap depth is 350 μK. The trap frequencies can be approximated by assuming the atom's are close to the trap minimum and fitting a harmonic trap to the potential. Using this procedure we find that the trap frequencies are 289 kHz in the radial direction and 47 kHz in the azimuthal direction. A dipole trap utilizing two fields in this way was first proposed by Ovchinnikov et al. in 1991 [61] and was theoretically described for use with nanofibers by Le Kien et al. in [31].

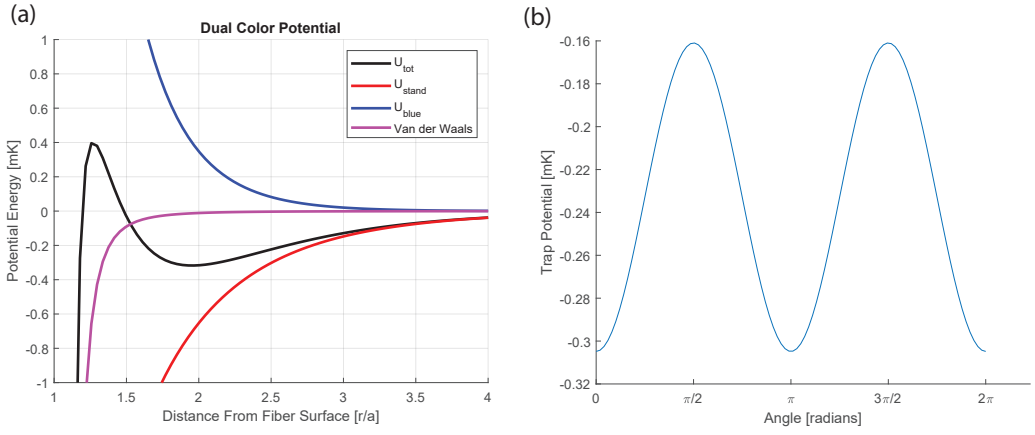

Figure 3.4: (a) The trapping potential (black curve) produced by two fields red and blue detuned, red and blue curves respectively. The Van der Waals interaction due to the atom interacting with the nanofiber surface is shown in purple. (b) The potential depth along the azimuthal direction.

3.4 Raman Transitions

The most basic configuration for an atom interferometer uses Raman transitions [15]. Consider an atom with two ground states $|g_1\rangle$ and $|g_2\rangle$ and an excited state $|e\rangle$ as shown in Figure (3.5). The two states $|g_1\rangle$ and $|g_2\rangle$ can be two of the hyperfine states in the ground state manifold of alkali atoms. These states cannot be coupled using a single laser field due to the dipole selection rules [46]. However, to couple the two states we can use two laser fields, one at frequency ω_1 that couples $|g_1\rangle \rightarrow |e\rangle$ and the other at frequency ω_2 that couples $|g_2\rangle \rightarrow |e\rangle$. The Hamiltonian for this system consists of three parts

$$\hat{H} = \hat{H}_{\text{atom}} + \hat{H}_{\text{mot}} + \hat{H}_{\text{int}} \tag{3.11}$$

where

$$\begin{aligned} \hat{H}_{atom} &= \hbar\omega_e \left|e\right\rangle\left\langle e\right| + \hbar\omega_{g_2} \left|g_2\right\rangle\left\langle g_2\right| \\ \hat{H}_{mot} &= \frac{\hat{p}^2}{2m} \\ \hat{H}_{int} &= -\hat{d} \cdot \vec{E}(z,t) \end{aligned} \tag{3.12}$$

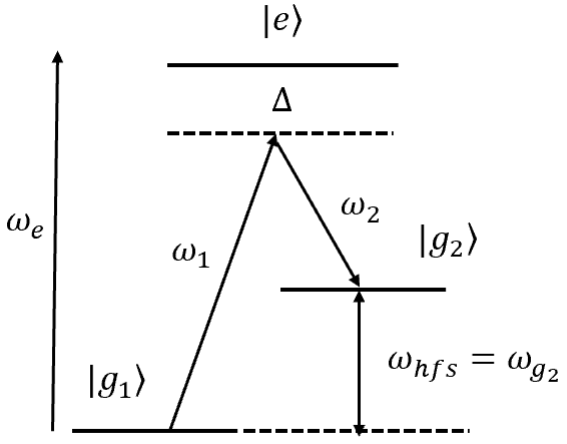

Figure 3.5: Lambda type three-level system.

The interaction Hamiltonian $\hat{H}_{\text{int}}$ was written in the dipole approximation where the total field is $\vec{E}(z,t) = \sum_{j=1}^{2} E_j \vec{\epsilon}_j \cos(\omega_j t + \phi_j - k_j z)$. Considering that $\vec{E}_i$ only couples $|g_i\rangle \rightarrow |e\rangle$, we can ignore the small cross coupling terms. Under this approximation, the Hamiltonian can be written as (see Appendix (A))

$$\hat{H}_{\text{int}} = \sum_{j=1}^{2} \left(\hbar \Omega_{g_j,e}^{(j)} |g_j\rangle\langle e| + h.c \right) \left(e^{i(\omega_j t + \phi_j - k_j z)} + e^{-i(\omega_j t + \phi_j - k_j z)} \right) \tag{3.13}$$

To further simplify the dynamics, we transform to a frame rotating at the laser frequencies. For details see Appendix (A). After making the rotating wave approximation the Hamiltonian becomes

$$\hat{H}^{rot} = \frac{\hat{p}^2}{2m} - \hbar\Delta |e\rangle\langle e| - \hbar\delta |g_2\rangle\langle g_2| + \sum_{j=1}^{2} \left(\hbar \Omega_{g_j,e}^{(j)} |g_j\rangle\langle e| \, e^{i(\phi_j - k_j z)} + H.c \right) \tag{3.14}$$

where $\Delta = \omega_1 - \omega_e$ is the single photon detuning and $\delta = (\omega_1 - \omega_2) - \omega_{g_2}$ is the two photon detuning. This Hamiltonian describes the coupling between the two levels $|g_1\rangle$ and $|g_2\rangle$ via the excited state $|e\rangle$. The position dependence of the phase of the field has also been kept in this derivation. Considering the z parameter as a an operator, we can see that the interaction of the field also couples the momentum

states of the atom [62]. The expansion of the complex exponential in momentum space is

$$e^{\pm ik\hat{z}} = \int |p\rangle \langle p \mp \hbar k| \, dp \tag{3.15}$$

Inserting this into the rotating interaction Hamiltonian equation (3.14), we get terms such as $|g_j, p\rangle \langle e, p + \hbar k|$ and $|e, p\rangle \langle g, p - \hbar k|$. Thus for absorption the momentum increases by $\hbar k$ such as for the transition from $|g_j\rangle$ to $|e\rangle$. On the other hand if emission occurs the momentum decreases by $\hbar k$ such as when a transition from $|e\rangle$ to $|g_j\rangle$ occurs.

It is instructive to look at the set of differential equations that result from equation (3.14)

$$\begin{aligned}
i\hbar \dot{c}_{g_1} &= \frac{p^2}{2m} c_{g_1} + \hbar \Omega^{(1)}_{g_1,e} c_e e^{i(\phi_1 - k_1 z)} \\
i\hbar \dot{c}_{g_2} &= \frac{p^2}{2m} c_{g_2} - \hbar \delta c_{g_2} + \hbar \Omega^{(2)}_{g_2,e} c_e e^{i(\phi_2 - k_2 z)} \\
i\hbar \dot{c}_e &= \frac{p^2}{2m} c_e - \hbar \Delta c_e + \hbar \Omega^{(1)}_{g_1,e} c_{g_1} e^{-i(\phi_1 - k_1 z)} + \hbar \Omega^{(1)}_{g_1,e} c_{g_1} e^{-i(\phi_1 - k_1 z)}
\end{aligned} \tag{3.16}$$

When the detuning is large, this set of differential equations can be further simplified by adiabatically eliminating the excited state. Thus we make the approximation that $\dot{c}_e = 0$.

$$\begin{aligned}
c_e &= \frac{-\frac{\hbar \Omega^{(1)}_{g_1,e}}{2} c_{g_1} e^{-i(\phi_1 - k_1 z)} - \frac{\hbar \Omega^{(2)}_{g_2,e}}{2} c_{g_2} e^{-i(\phi_2 - k_2 z)}}{\frac{p^2}{2m} - \hbar \Delta} \\
&\approx \frac{\Omega^{(1)}_{g_1,e}}{2\Delta} c_{g_1} e^{-i(\phi_1 - k_1 z)} + \frac{\Omega^{(2)}_{g_2,e}}{2\Delta} c_{g_2} e^{-i(\phi_2 - k_2 z)}
\end{aligned} \tag{3.17}$$

where we have also used $\frac{p^2}{2m} \ll \hbar\Delta$ which is the case for $p = \hbar k$ where $\lambda = 852$ nm and $\Delta = 1$ GHz which is the case for the work in this thesis. Inserting equation (3.17) into equation (3.16) we get

$$\begin{aligned}
i\hbar \dot{c}_{g_1} &= \frac{p^2}{2m} c_{g_1} + \frac{\hbar |\Omega^{(1)}_{g_1,e}|^2}{4\Delta} c_{g_1} + \frac{\hbar \Omega^{(1)}_{g_1,e} \Omega^{(2)}_{g_2,e}}{4\Delta} c_{g_2} e^{i(\phi_1 - \phi_2)} e^{-i(k_1 - k_2)z} \\
i\hbar \dot{c}_{g_2} &= \frac{p^2}{2m} c_{g_2} - \hbar \delta c_{g_2} + \frac{\hbar |\Omega^{(2)}_{g_2,e}|^2}{4\Delta} c_{g_2} + \frac{\hbar \Omega^{(2)}_{g_2,e} \Omega^{(1)}_{g_1,e}}{4\Delta} c_{g_1} e^{i(\phi_2 - \phi_1)} e^{-i(k_2 - k_1)z}
\end{aligned} \tag{3.18}$$

The system reduces to a two level system with an effective Rabi rate

$$\Omega_{\text{eff}} = \frac{\Omega^{(1)}_{g_1,e}\Omega^{(2)}_{g_2,e}}{2\Delta} \tag{3.19}$$

Equation (3.18) can also be written in terms of an effective Hamiltonian

$$\begin{aligned}\hat{H}_R = &\frac{p^2}{2m} + \frac{\hbar|\Omega^{(1)}_{g_1,e}|^2}{4\Delta}\left|g_1\right\rangle\!\left\langle g_1\right| + \frac{\hbar|\Omega^{(2)}_{g_2,e}|^2}{4\Delta}\left|g_2\right\rangle\!\left\langle g_2\right| \\ &+ \frac{\hbar\Omega_{\text{eff}}}{2}\left(\left|g_1\right\rangle\!\left\langle g_2\right| e^{i(\phi_1-\phi_2)}e^{-i(k_1-k_2)z} + \left|g_2\right\rangle\!\left\langle g_1\right| e^{i(\phi_2-\phi_1)}e^{-i(k_2-k_1)z}\right)\end{aligned} \tag{3.20}$$

In this form, it is easy to see that there is also an AC Stark shift that arises from the interaction (the diagonal terms)

$$\Delta E_i = \frac{\hbar|\Omega^{(1)}_{g_i,e}|^2}{4\Delta} \tag{3.21}$$

The solutions to this system of equations are

$$\left|\psi(t)\right\rangle = \cos\left(\frac{\Omega_{\text{eff}}}{2}t\right)\left|g_1\right\rangle - i\sin\left(\frac{\Omega_{\text{eff}}}{2}t\right)e^{i\phi}\left|g_2\right\rangle \tag{3.22}$$

for the initial conditions $c_{g_1}(0) = 1$ and $c_{g_2}(0) = 0$. Also, $\phi = \phi_1 - \phi_2$ is the laser's phase imprinted onto the atom during the interaction. For instance, if the atom undergoes a transition from $\left|g_1\right\rangle$ to $\left|g_2\right\rangle$, the state picks up this phase. This phase is used as a memory of the interaction and is also the dominant contribution to the atom interferometer phase. This is discussed further in section (3.5).

3.4.1 Effects of the Evanescent Field Decay

The fundamental mode of the nanofiber has an evanescent tail that decays away from the fiber surface. This spatially dependent intensity gives rise to coupling between the atom's internal states and its motional states [29, 32, 33, 47] while in the nanofiber trap. Atoms undergoing Raman transitions in the trap will experience a momentum kick perpendicular to the $\vec{k}$ vector of the fields for co-propagating Raman field and in addition to the $2\hbar k$ momentum kick along $\vec{k}$ for counter-propagating Raman fields.

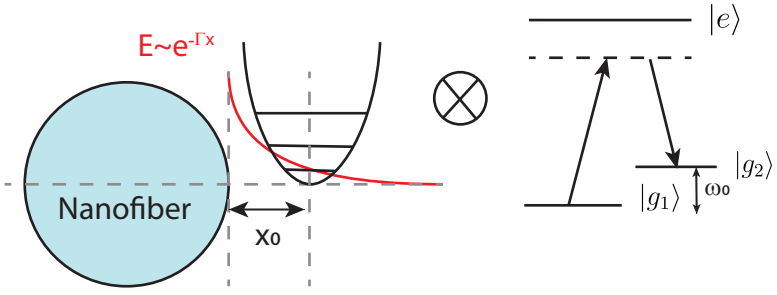

Figure 3.6: This figure shows a model of an atom in a nanofiber trap interacting with a fiber-guided field. The trap is approximated as a harmonic potential and the guided field decays radially outward (shown in red). The state space consists of the internal states of the three-level atom and the harmonic oscillator states.

In this section, numerical simulations are presented to analyze the effect of this motional coupling on the efficiency of the Raman transitions.

Assuming the trapped atoms have a low enough temperature we can approximate the trap as a harmonic potential. The state space of the system is the set of motional states of the harmonic oscillator and that of a three-level atom, $\{|n\rangle\}\otimes\{|g\rangle_1, |g\rangle_2, |e\rangle\}$ as shown in Figure (3.6). The Hamiltonian has the following contributions as before

$$\hat{H} = \hat{H}_{mot} + \hat{H}_{atom} + \hat{H}_{int} \tag{3.23}$$

The atomic motion includes the atom's kinetic energy and the harmonic trap potential with frequency ω_T. The harmonic trap Hamiltonian can be written as

$$\begin{aligned} \hat{H}_{mot} &= \frac{\hat{p}^2}{2m} + \frac{1}{2}m\omega_T^2\hat{x}^2 \\ &= \hbar\omega_T\left(\hat{N} + \frac{1}{2}\right) \end{aligned} \tag{3.24}$$

where $\hat{N} = \hat{a}^\dagger\hat{a}$. We have introduced the annihilation $\hat{a}$ and creation $\hat{a}^\dagger$ operators such that $\hat{a}\,|n\rangle = \sqrt{n}\,|n-1\rangle$ and $\hat{a}^\dagger\,|n\rangle = \sqrt{n+1}\,|n+1\rangle$. As in the previous section, the atomic three-level system has an excited state $|e\rangle$ and two ground states $|g_1\rangle$ and $|g_2\rangle$. The Hamiltonian, $\hat{H}_{atom}$, is the same as before and is given in equation (3.12). The

interaction term includes a dipole interaction of the atom with an electric field with an exponentially decaying amplitude. To model this effect, we use the approximation that the evanescent tail of the HE_{11} field behaves as a decaying exponential $K_m(x) \propto \exp(-\Gamma x)$ for $x \gg 1$.

$$\hat{H}_{int} = -\hat{\vec{d}} \cdot \left(\vec{E}_1(t,r) + \vec{E,r}_2(t) \right) \tag{3.25}$$

where the electric field is $E_i(t) = E_i \mathrm{e}^{-\Gamma r} \cos(\omega_i t + \phi)$. The field amplitude decays with a decay constant Γ.

By adiabatically eliminating the excited state, $|e\rangle$, we can reduce the dynamics to a two level system that includes transitions between $|g_1\rangle$ and $|g_2\rangle$. In a frame rotating at the difference resonance frequency ω_0 for the ground states and a rate ω_T for the motional degrees of freedom and after making the rotating wave approximation, we get the following Hamiltonian

$$\hat{H} = \frac{\Omega_0}{2} \left(\hat{\sigma}_+ e^{-i(\Delta t - \phi)} + \hat{\sigma}_- e^{i(\Delta t - \phi)} \right) \exp\left(-\eta (\hat{a} e^{-i\omega_T t} + \hat{a}^\dagger e^{i\omega_T t}) \right) \tag{3.26}$$

where $\Omega_0 = \Omega_{\text{eff}}$ defined in equation (3.19), Δ is the detuning, $\hat{\sigma}_+ = |g_2\rangle\langle g_1|$, $\hat{\sigma}_- = |g_1\rangle\langle g_1|$, and $\eta = \Gamma \Delta x_0$. This parameter is similar to the Lamb-Dicke parameter in that it compares the extent of the wave function $\Delta x_0 = \sqrt{\hbar / 2m\omega_T}$ with the characteristic decay of the evanescent field. Here, m is the mass of the atom. The characteristic decay is dependent on the geometry of the fiber and is typically $\Gamma^{-1} = 200$ nm. For a trap of frequency $\omega_T = 2\pi 100$ kHz, $\eta = 0.135$. This justifies considering the case when $\eta \ll 1$ so that the exponential can be Taylor expanded to first order in η [32]. For this case

$$\hat{H} = \frac{\Omega_0}{2} \left(\hat{\sigma}_+ e^{-i(\Delta t - \phi)} + \hat{\sigma}_- e^{i(\Delta t - \phi)} \right) \left(1 - \eta (\hat{a} e^{-i\omega_T t} + \hat{a}^\dagger e^{i\omega_T t}) \right) \tag{3.27}$$

From this expression, we see that the evanescent field decay couples the internal degrees of freedom with external degrees of freedom (i.e., the atomic motion). This Hamiltonian is similar to the motional coupling used in ion traps [32, 63]. For $\Delta = 0$, the carrier transition is strongest. The off-resonant terms can be ignored i.e.,

no motional transitions arise, if the coupling strength $\Omega_0\eta \ll \omega_T$. The Hamiltonian is then given by

$$\hat{H} = \frac{\Omega_0}{2}\left(\hat{\sigma}_+ e^{i\phi} + \hat{\sigma}_- e^{-i\phi}\right) \tag{3.28}$$

The approximation can be understood in terms of a spectroscopy argument. The coupling strength of the off-resonant terms is equal to $\Omega_0\eta$ which doesn't provide enough energy to drive the motional state transitions if it meets the condition $\Omega_0\eta \ll \omega_T$. Similarly, red (blue) sideband transitions can be driven if $\Delta = -(+)\omega_T$. We can neglect off-resonant terms if $\Omega_0 \ll \omega_T$. The Hamiltonian for the blue sideband transitions is

$$\hat{H} = -\frac{\Omega_0\eta}{2}\left(\hat{\sigma}_+ \hat{a}^\dagger + \hat{\sigma}_- \hat{a}\right) \tag{3.29}$$

In the cases presented, the relative values between Ω_0 and ω_T were important for neglecting off-resonant terms. This relationship is important and typically shows up in the context of ion traps [32]. In the resolved regime, $\omega_t \gg \Omega$, and specific transitions (carrier or sidebands) can be addressed. In the unresolved regime $\omega_t \ll \Omega$, off-resonant terms and higher order sidebands have a non-negligible coupling strength resulting in population transfer to other motional states.

To explore this further, a numerical simulation using the Hamiltonian in equation (3.26) was performed using the QuantumOptics Julia toolbox. Figure (3.7) shows the results for an atom initially prepared in the state $|\psi_0\rangle = |n = 0, g_1\rangle$ and $\Delta = 0$. The transfer of population between the states $|g_1\rangle$ and $|g_2\rangle$ is shown for the resolved and unresolved regimes. In (a), the trap frequency is $\omega_T = 10\Omega_{\text{eff}}$. Here, transitions between two levels can be driven exactly. In (3.7)(b), we see that the motional state doesn't couple to other motional states. In Figure (3.7)(c), we plot the results for $\omega_T = 0.1\Omega_{\text{eff}}$ and the same conditions as in (3.7)(a). Here, we see that even if we start in the same state, there are non-zero coupling strengths between $|g_1, n\rangle \rightarrow |g_2, n+1\rangle$ states. Each of these transitions has a different Rabi frequency given by

$$\Omega_{n',n} = \Omega_0 \left| e^{\eta^2/2}\sqrt{\frac{n_<!}{n_>!}}(-\eta)^{\Delta n} L_{n_<}^{\Delta n}[-\eta^2] \right| \tag{3.30}$$

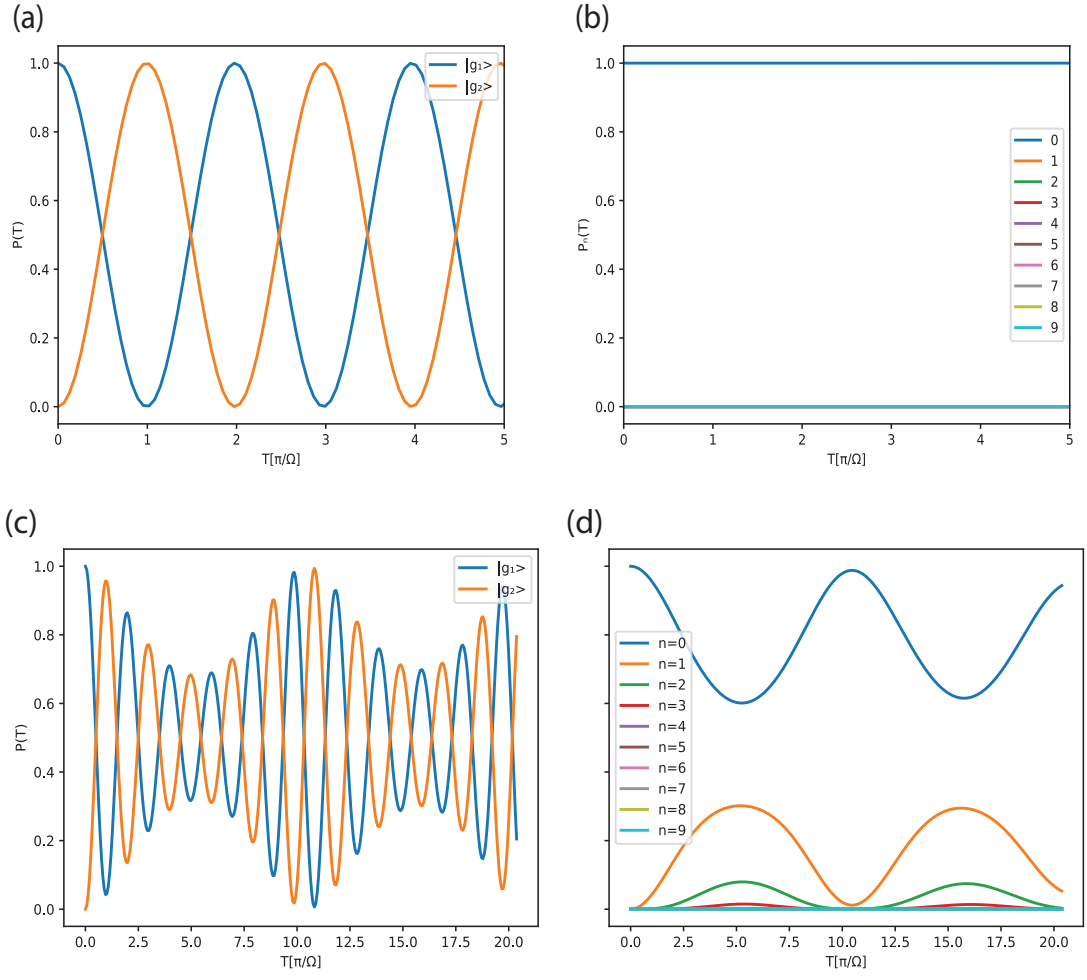

Figure 3.7: Simulation results for the interaction of a guided Raman field with a two level atom. The first column displays the Rabi oscillations between the internal states for (a) the resolved regime $\omega_T = 10\Omega_{\text{eff}}$ and (c) the unresolved regime $\omega_T = 0.1\Omega_{\text{eff}}$. The atom's initial state is $|g_1, n = 0\rangle$. In the second column, (b) and (d) display the dynamics of the Fock states during the evolution shown in (a) and (c). We see that in the unresolved regime transitions to higher order Fock states occur.

Due to the different Rabi frequencies associated with the different couplings $|g_1, n\rangle \rightarrow |g_2, n+1\rangle$, we see a inhomogeneous dephasing occur. These decay mechanisms are reversible and we see revivals after the initial decay.

The above ideal cases exemplify the importance of the relationship between the

Ω_{eff} and ω_T. However, in the laboratory it is often difficult to prepare atoms in the ground state of the confining potential, $|n\rangle = |0\rangle$. To get a better understanding of the dynamics with an initial thermal distribution, consider the case where the atom is initially in a thermal state

$$\begin{aligned}\rho_0 &= e^{-\hat{H}_{mot}/k_bT}/Z \\ &= \sum_n \frac{e^{-\hbar\omega_T\left(\hat{N}+1/2\right)/k_bT}}{Z}\,|n\rangle\langle n|\end{aligned} \tag{3.31}$$

where

$$Z = \sum_n \exp\left(-\hbar\omega_T\left(\hat{N}+1/2\right)\right) \tag{3.32}$$

is the partition function, k_b is Boltzmann's constant, and T is the temperature. This state describes a statistical mixture of motional states whose distribution is dependent on the temperature T. Consider an initial thermal distribution of Fock states as shown in Figure (3.8) where for a trap frequency of $\omega_T = 2\pi$ 100 kHz, we have a temp of 38 μK. This temperature is consistent with experimentally measured values for nanofiber trapped cesium atoms [26, 64]. To study the dynamics of the system in the resolved and unresolved regime with the initial thermal state, the QuantumOptics Julia toolbox is used. The evolution of the system is now numerically solved using the Liouville equation

$$i\hbar\dot{\rho}t = [H, \rho] \tag{3.33}$$

where the Hamiltonian H is given in equation (3.26). The simulation results are shown in Figure (3.9). For the resolved regime, the effect of the state dependent Rabi frequency and the initial distribution of Fock states causes a dephasing effect that damps down the oscillations as shown in Figure (3.9)(a). This is a notable difference when compared to the ideal evolution shown in Figure (3.7)(a). The damping is more severe in the unresolved regime as shown in Figure (3.9)(b). In both cases, revivals appear since these damping mechanisms are reversible.

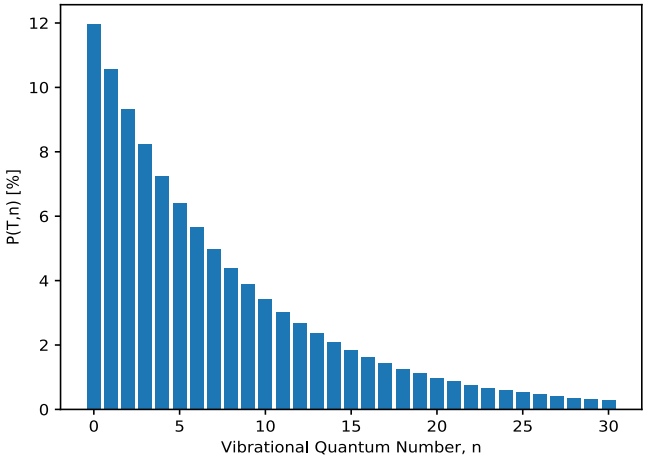

Figure 3.8: The initial population distribution in the Fock states $|n\rangle$ for a thermal state with initial temperature $T = 8\frac{\hbar\omega_T}{k_B}$ is shown. For $\omega_T = 2\pi 100$ kHz this indicates a temperature $T = 38$ μK.

3.4.2 Polarization Considerations

In free space, the typical Raman transition polarization configurations are $\sigma_+ - \sigma_+$, $\sigma_- - \sigma_-$ or a combination of these two in lin $\perp$ lin with the quantization axis chosen along the direction of $\vec{k}$. When driving Raman transitions with a guided HE_{11} mode, the multiple polarization components that are present can drive several Raman paths simultaneously. Consider the HE_{11} field (equation (2.30)) written in the Cartesian basis then in the spherical basis

$$\begin{aligned}\vec{E}^{lin}(r,\phi,z) &= A\sqrt{2}\left(X(r,\phi)\hat{x} + Y(r,\phi)\hat{y} + fZ(r,\phi)\hat{z}\right)\exp(if\beta z - i\omega t) \\ &= A\sqrt{2}\left(\frac{iX(r,\phi) - fZ(r,\phi)}{\sqrt{2}}\hat{e}_+ + \frac{iX(r,\phi) + fZ(r,\phi)}{\sqrt{2}}\hat{e}_- + fY(r,\phi)\vec{e}_0\right) \\ &\times \exp(if\beta z - i\omega t)\end{aligned} \tag{3.34}$$

where the spherical basis components are given in Appendix (B) and the quantization axis has been chosen along y. This expression shows that, in general, all three

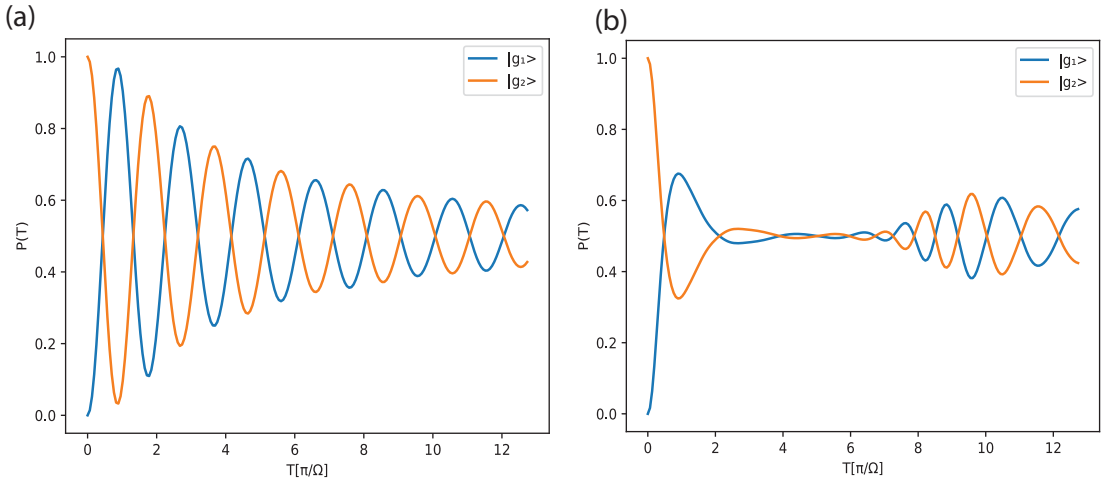

Figure 3.9: Simulation of the internal state evolution for an initial internal state $|g_1\rangle$ and motional state given by a thermal state with initial temperature $T = 38\ \mu$K for (a) the resolved regime $\omega_T = 10\Omega_{\text{eff}}$ and (b) the unresolved regime $\omega_T = 0.1\Omega_{\text{eff}}$.

spherical basis components are non-zero. The functions $X(r,\phi)$, $Y(r,\phi)$, and $Z(r,\phi)$ are used to simplify the expressions and are given by

$$\begin{aligned} X(r,\phi) &= e_r \cos(\phi - \phi_0)\cos(\phi) - i e_\phi \sin(\phi - \phi_0)\sin(\phi) \\ Y(r,\phi) &= e_r \cos(\phi - \phi_0)\sin(\phi) + i e_\phi \sin(\phi - \phi_0)\cos(\phi) \\ Z(r,\phi) &= e_z \cos(\phi - \phi_0) \end{aligned} \tag{3.35}$$

where the field amplitudes e_r, e_ϕ, and e_z are given in equation (2.32). The quantization axis has been chosen along y to emphasize one of the paramount differences between driving Raman transitions in free space and with fiber-guided fields. In the latter, the longitudinal component of the HE_{11} mode allows for the quantization axis to be perpendicular to the effective field wave vector, $\vec{k} = \vec{k}_1 - \vec{k}_2$. This situation will be analyzed at the end of this section.

The effective Rabi frequency for the Raman transition between states $|g_1\rangle$ and $|g_2\rangle$ is given by [62, 65]

$$\Omega_{\text{eff}} = \sum_i \frac{\Omega_{g_1,i}\Omega^*_{g_2,i}}{2\Delta} \tag{3.36}$$

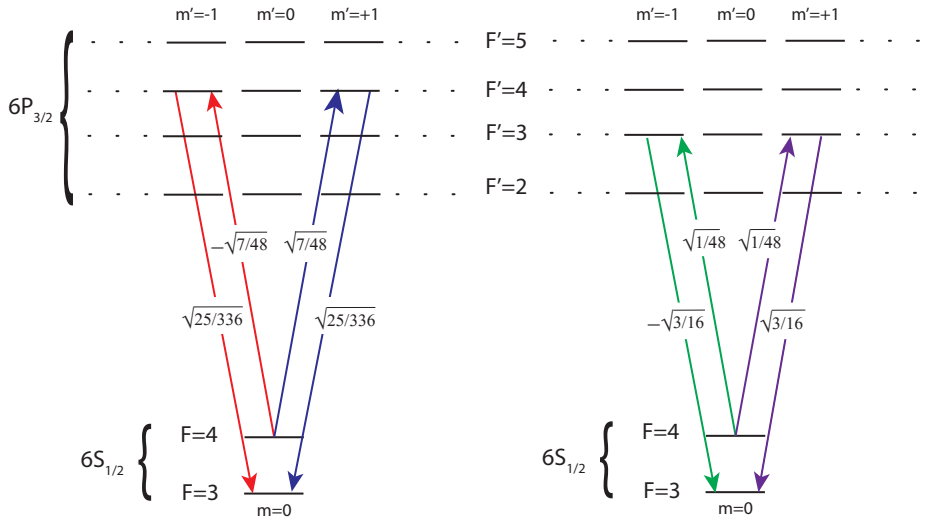

Figure 3.10: The allowed channels for Raman coupling of the two clock states of cesium given that can be driven with σ_+ and σ_- polarization components present in the laser fields.

where we have introduced the multi-level structure of the excited state manifold by summing over all possible intermediate states $|i\rangle$ [66]. Considering the multi-level structure is important as destructive interference can occur when there is a relative phase difference between transition paths. This phase is manifest through either the coupling strength or field polarization and can cause complete cancellation of the coupling amplitude [67] or reduce its strength [68]. In Figure (3.10), the relevant Raman channels for cesium are presented for transitions between the clock states, $|g_1\rangle = |F = 3, m = 0\rangle$ and $|g_2\rangle = |F = 4, m = 0\rangle$, coupled via the $6P_{3/2}$ manifold. In practice, the clock state transitions can be isolated with a suitably strong magnetic field so other ground state magnetic sub-levels can be neglected. Due to dipole selection rules, namely $\Delta F = 0,\ \pm 1$, only the sub-manifolds $|F' = 3, 4, m\rangle$ can contribute to Raman transitions. An example of destructive interference occurs for the blue and red paths in Figure (3.10). This is due to the π phase shift between the two paths when summing the effective Rabi frequencies in equation (3.36) which cancels the

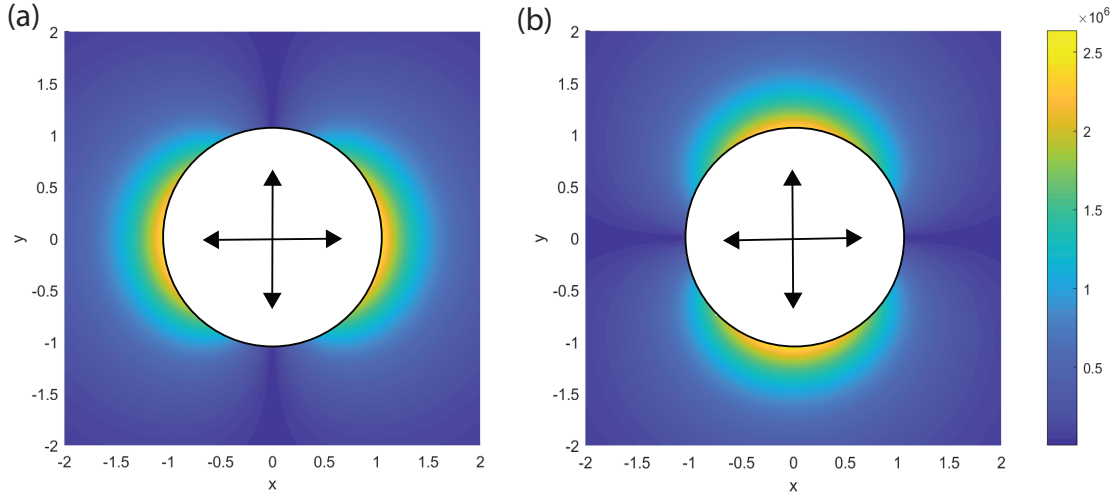

Figure 3.11: The magnitude of the effective total Raman coupling strength in equation (3.36) is calculated for counter-propagating fiber-guided beams, each with a power of 9 nW. The lin-⊥-lin configuration is indicated by the black arrows. The quantization axis is chosen as $\vec{y}$ in (a) and $\vec{x}$ in (b). The color bar indicates the coupling strength in units of rad*Hz.

Raman coupling amplitudes. The π transitions are not included as the transition strength between $|F, m\rangle \rightarrow |F', m\rangle$ vanishes when $F = F'$ [46], where the prime indicates the intermediate states.

Equation (3.34) shows that all three polarization components are present in the HE_{11} mode and therefore is able to drive $\sigma_+ \rightarrow \Delta m = +1$, $\sigma_- \rightarrow \Delta m = -1$, and $\pi \rightarrow \Delta m = 0$ magnetic sub-level transitions. The magnitude of equation (3.36) using equation (3.34) for each field $\vec{E}_1$ and $\vec{E}_2$ is shown in figure (3.11). Two counter-propagating fields each with a power of 9 nW and orthogonal polarization (lin-⊥-lin) are considered. The color bar indicates the coupling strength with a maximum of 2π 2.5 MHz. The non-zero coupling strength is due to the longitudinal components of the field. In order to drive Raman transitions with this configuration, the atom trap beam polarization should be chosen such that the atoms are trapped along the direction of the quantization axis to maximize the coupling amplitude.

3.5 Atom Interferometry

In light pulse atom interferometry (LPAI), a Raman transition using counter-propagating fields is used to impart a momentum of $\hbar k_{\text{eff}}$ onto the atom conditioned on its internal state. A sequence of three pulses applied to the atoms is used to split, reflect, and recombine the atomic wavepackets [15]. The three pulses are temporally separated as shown in the diagram in Figure (3.12)(a). Each pulse imprints the laser's phase onto the atomic wavefunction. The optical wavefronts then provide a ruler oriented along the propagation direction of the field, $\vec{k}_{\text{eff}}$ with tick spacing of $\lambda/2$. The sequence consists of the three pulses, a $\pi/2$, π, and $\pi/2$ pulse. The first pulse splits the atomic wavepacket resulting in a quantum superposition state $|\psi\rangle = |g_1, p\rangle + |g_2, p + \hbar k\rangle$. The split wavepacket is allowed to evolve freely for a time T, called the interrogation time. Then a π pulse flips the internal states of the atom taking $|g_1, p\rangle \rightarrow |g_2, p + \hbar k\rangle$ and $|g_2, p + \hbar k\rangle \rightarrow |g_1, p\rangle$. The wavepacket is again allowed to evolve for an interrogation time T and a final $\pi/2$ pulse is applied to cause the two paths to interfere.

The total phase shift between the arms of the interferometer has three contributions [69, 70]

$$\Delta\phi_{total} = \Delta\phi_{\text{prop}} + \Delta\phi_{\text{laser}} + \Delta\phi_{\text{sep}} \tag{3.37}$$

where $\Delta\phi_{\text{prop}}$ is the difference in phase due to the propagation of the wavepackets between interrogation pulses, $\Delta\phi_{\text{laser}}$ is the shift acquired during the atom-light interactions, and $\Delta\phi_{\text{sep}}$ is a shift due to a possible separation of the wavepackets during the final pulse of the interferometer. For a uniform gravitational field $\Delta\phi_{\text{prop}} = 0$ [69]. Also, assuming perfect overlap between the atomic wavefunctions at the end of the pulse sequence results in $\Delta\phi_{\text{sep}} = 0$. Higher order terms and corrections to non-uniform gravitational fields are available in [70]. The laser phase is imprinted onto the atomic wavepacket during the interaction where the sign of the phase is

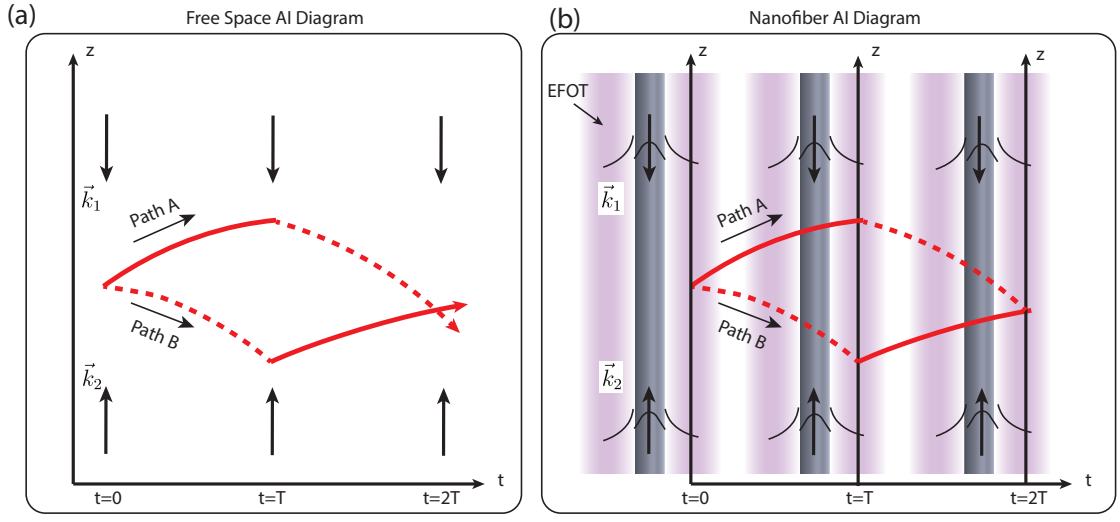

Figure 3.12: Spacetime diagram of a light pulse atom interferometer sequence for (a) the atom cloud in free space and (b) atoms trapped around a nanofiber. The evanescent field optical trap confines atoms 215 nm away from the fiber surface. The fiber-guided Raman beams exhibit an evanescent tail with decaying intensity away from the fiber. Trapped atoms are free to move along the z direction.

dependent on the initial state. The transitions can be written as

$$\begin{aligned} |g_1\rangle &\rightarrow e^{i\vec{k}_{\text{eff}}\cdot\vec{z_p}(t_p)-i\Delta\omega t_p}\,|g_2\rangle \\ |g_2\rangle &\rightarrow e^{-i\vec{k}_{\text{eff}}\cdot\vec{z_p}(t_p)-i\Delta\omega t_p}\,|g_1\rangle \end{aligned} \tag{3.38}$$

where $\vec{k}_{\text{eff}} = \vec{k}_1 - \vec{k}_2$, $\Delta = \omega_1 - \omega_2$, and t_p is the time at which the p^{th} pulse is applied. The total phase difference between the wavefunctions along the different paths after the three pulse sequence is

$$\Delta\phi_{total} = \phi(z_1^A, t_1) - \phi(z_2^A, t_2) - \phi(z_2^B, t_2) + \phi(z_3^A, t_3) \tag{3.39}$$

where

$$\phi(z,t) = \vec{k}_{\text{eff}} \cdot \vec{z}(t) - \Delta\omega t \tag{3.40}$$

When the pulses are applied symmetrically, the term $\Delta\omega = 0$ so that

$$\Delta\phi_{total} = \vec{k}_{\text{eff}} \cdot \vec{g}\, T^2 \tag{3.41}$$

The probability of finding the atom in the state $|g_1\rangle$ after the pulse sequence is

$$P(\Delta\phi) = \frac{1}{2}\left(1 - \cos(\Delta\phi)\right) \tag{3.42}$$

As was mentioned in section (3.4.1), if the Raman Rabi frequency is limited such that the interferometer operates in the resolved regime, i.e., $\Omega_{\text{eff}} \ll \omega_T$ the evanescent field of the guided Raman beam will not excite transverse motional states. In this regime, only momentum along the beam axis is imparted onto the atomic wavepacket and an atom interferometer utilizing fiber-guided fields can be realized.

Chapter 4

Nanofiber Fabrication

Some compact atom interferometers use an interrogation time of several milliseconds to leverage a high data rate [9, 10, 11]. Applying this concept to an atom interferometer based on a nanofiber indicates the length of the nanofiber waist can be a limiting factor. Conceptually, in such an interferometer atoms would be trapped at the waist and guided by the evanescent field that extends along its length setting limits on the interrogation time. For instance, a waist length of 10 mm allows for an interrogation time of 20 ms when the fiber is positioned vertically. With this in mind, our nanofiber pulling rig was designed with the capability of varying the waist length from a few millimeters to several centimeters. In addition, the pulling rig can produce double taper nanofibers which help shorten the taper section and adds rigidity. Another important condition is the reproducibility of nanofibers with a predetermined waist radius. Measuring the nanofiber radius typically involves a destructive process such as coating the fiber with a conductive material for SEM imaging, rendering the fiber unusable. In this chapter we discuss the details of our nanofiber pulling rig and the repeatability of nanofiber fabrication.

4.1 Tapered Nanofiber Design

A tapered nanofiber has three main sections: the non-modified fiber, taper, and waist (nanofiber section) as shown in Figure (4.1). The geometry of a nanofiber atom guide needs to be optimized for implementing atom interferometry. First, the radius of the fiber needs to be optimized so that the evanescent field efficiently interacts with the surrounding atoms. In our experiment, there are several different wavelengths coupled into the fiber for trapping atoms and state manipulation. Our nanofiber radius of 215 nm was chosen to optimize the extent of the evanescent field for the red (937 nm) trapping laser as discussed in section (3.2). At this radius the Raman laser wavelength of 852 nm is also close to optimal.

Second, the waist has to be long enough so atoms fall for a maximal time which is possible if they are trapped near one end of the waist and allowed to fall to the other end during the atom interferometry sequence. In section (3.5), the sensitivity of an atom interferometer was shown to be quadratically dependent on the interrogation time, T, and is given by $\Delta\phi = 2kgT^2\cos(\theta)$, where θ is the angle between the $\vec{k}$ and $\vec{g}$. A straight forward method of increasing the sensitivity is to increase T. The total interferometric time is roughly $T_{\text{Tot}} = 2T$. Consider $\theta = 0^\circ$ then the distance the atoms fall during this time is $\Delta x = gT_{\text{Tot}}^2/2$. If atoms are instead guided by the nanofiber trap, the waist length required is $\Delta l = 2gT^2$. The sensitivity then becomes

$$\Delta\phi = k\Delta l\cos(\theta) \tag{4.1}$$

where θ is now the angle between the fiber axis and $\vec{g}$. The above equation shows that the sensitivity is linearly proportional to the length of the waist of the nanofiber. As further discussed in the next section, our apparatus has been designed with the capability of varying the waist length.

Finally, high transmission through the nanofiber can reduce laser power require-

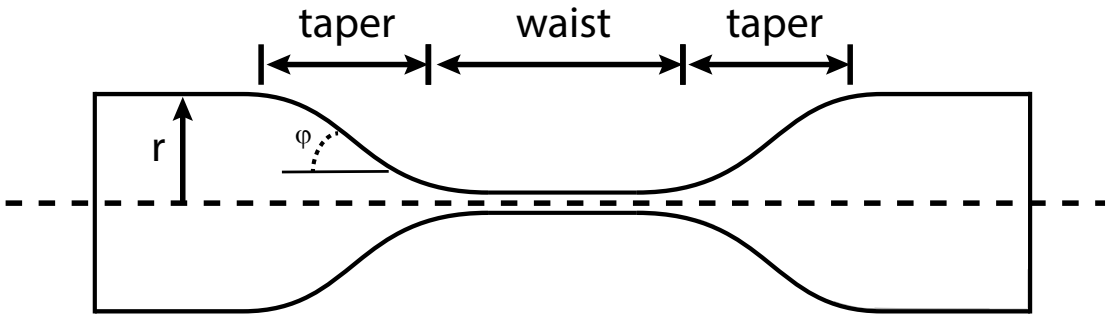

Figure 4.1: A tapered fiber has three main sections. The unmodified fiber, taper, and waist. The angle ϕ is the linear taper angle.

ments when performing atom trapping and atom manipulation experiments [71]. High transmission relies on the adiabatic transfer of energy between higher order modes and the fundamental mode [72]. Efficient energy transfer between modes is optimized by considering the adiabatic condition which places limits on the taper angle ϕ (see Figure (4.1)) [73]. It was shown in [74] that restricting the taper angle in the milliradian range is required to reach a transmission $> 99\%$. The design of the nanofibers used in our experiment consist of $\phi = 2$ mrad which results in total lengths of about 11 cm including the two tapered regions and the waist and a transmission $> 99.7\%$. Although, we don't have this capability, shorter total lengths can be achieved by considering fiber profiles with varying radii instead of a constant taper angle as demonstrated in [75].

4.2 Fiber Pulling Rig

With the design criteria discussed in the previous section in mind, we based our fiber pulling rig on [71]. The rig uses a simulated fiber brushing technique to fabricate the nanofibers which is a proven technique for producing ultra-high transmission tapered

optical fibers with sub-micron radii [71, 76]. In our system, a 780HP optical fiber is first clamped down onto two independent XML210 motorized stages (see Figure (4.2)). The optical fiber is then heated to its softening point using an oxy-hydrogen gas torch that is placed a distance 500 μm away. In the standard flame brushing method, the torch is placed on a motorized stage that moves it in an oscillating motion to sweep it across the fiber while the fiber is simultaneously stretched [76]. In the simulated fiber brushing version, the torch stays stationary and the pulling stages both stretch and sweep the fiber across the torch tip. This is done by having the motor stages perform a reciprocating motion while simultaneously pulling further apart which is equivalent to jumping into the torch's frame of reference. Although this method requires greater control of the motor stages trajectory, air currents are reduced around the flame that can result in non-uniform waist diameters [76, 71].

A necessary criteria for fabricating ultra-high transmission nanofibers is to keep them free of dust during and after fabrication [71]. Therefore the entire rig resides inside a clean room as shown in Figure (4.2). In addition, the rig sits on top of an optics breadboard inside a plexiglass enclosure that further shields it from dust and other contaminants. The additional enclosure was needed as many other unrelated experiments are also performed in the clean room that could produce contaminants. To keep the inside of the enclosure clean from dust we installed a table top air purifier inside the enclosure as well.

The two XML210 motor stages sit on top of a 200 lb granite slab in order to reduce mechanical vibrations resulting from their motion. They have a maximum travel range of 210 mm which allows us to fabricate nanofibers with waist lengths from a few millimeters to several centimeters. In addition, the trajectory of the motor stages can be controlled with a script indicating its position and velocity at a time t (PVT). We use an algorithm developed by [77] which provides the PVT trajectories required to produce a constant angle taper down to the nanofiber waist. The algorithm also provides the option of generating two linear tapers with different

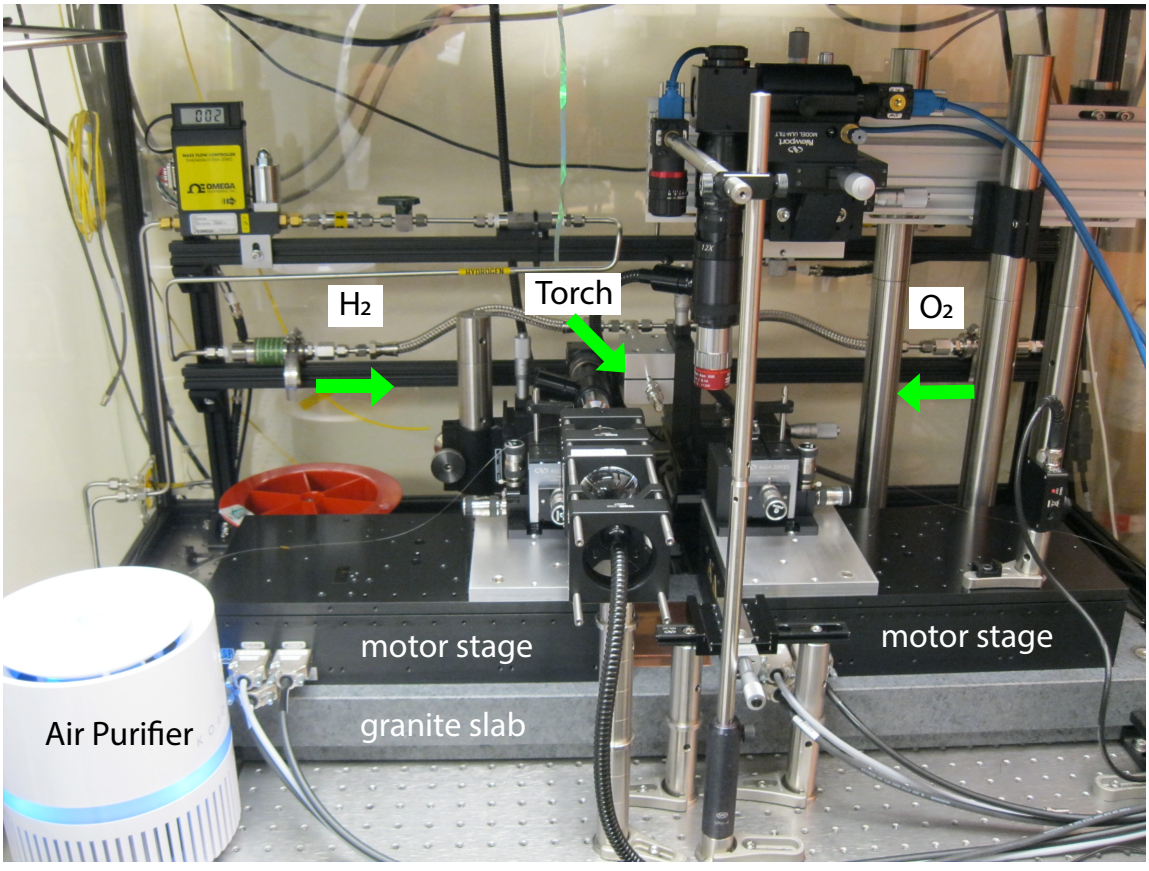

Figure 4.2: An image of the fiber pulling apparatus displaying the cameras used to prepare the nanofiber before the pull. The apparatus sits in an enclosure in clean room. A table top air purifier on the bottom left ensures the air stays clean when the enclosure is closed.

angles however we found a single taper results in optimal transmission. The oxygen and hydrogen gas flow is controlled by Omega flow meters set to 30 mL/min and 60 mL/min, respectively. The flow rate is computer controlled via our control system. This feature is used to turn on(off) the gas flow right before(after) pulling a fiber. The torch tip is custom fabricated with the design described in [77]. The effective flame width is measured experimentally and is required as an input parameter for the algorithm. This value is measured periodically and can vary by 10's of microns. The measurement involves stretching the fiber without a reciprocating motion which keeps the hot zone constant. The radius of the fiber as a function of the pulling

length is described by [78]

$$r(L_{\text{pull}}) = r_0 e^{-L_{\text{pull}}/2L_0} \tag{4.2}$$

where r_0 is the initial fiber radius, L_{pull} is the pulled length of the fiber, and L_0 is the flame width. Using the 780 HP fiber $r_0 = 125\ \mu m/2$. The fiber pulling length is $L_{\text{pull}} = 2tv_{\text{stage}}$ where t is the time elapsed during the pull and v_{stage} is the constant motor stage velocity. A sample data set is shown in Figure (4.3). A fit using equation (4.2) yields a flame width of 728 μm.

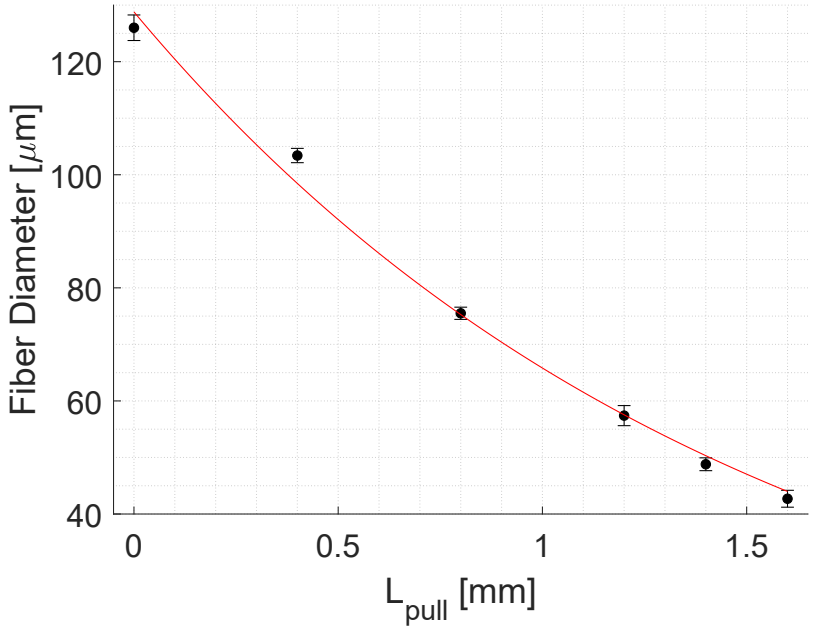

Figure 4.3: Data (black circles) taken to experimentally measure the flame width of the torch. A decaying exponential function is used to fit the data set. From the red curve the torch flame width was determined to be 728 μm.

4.3 Control System

The control system was written in LabVIEW and was structured to follow the fiber pulling procedure starting with fiber preparation to inspection. The diagram in

Figure (4.4) summarizes the control system design. First, the PVT file directory is specified. The torch is positioned several inches away from the fiber and the gas flow is off. After the fiber is inspected for dust, properly aligned, and tensioned, the torch gas flow is turned on and it is manually ignited. A start button initiates the fiber pull which loads the PVT file to the motor stages controller. The torch then moves into its final position 500 μm away from the fiber and the motor stages begin their trajectory. The total time for the pull takes about 7 minutes and is determined by the PVT stage trajectories. At the end of the pull, the gas flow turns off and the torch repositions itself at its home position (away from the fiber). At this point, the operator can re-tension the fiber to reduce slack introduced by the flame's air pressure pushing on the fiber during the pull.

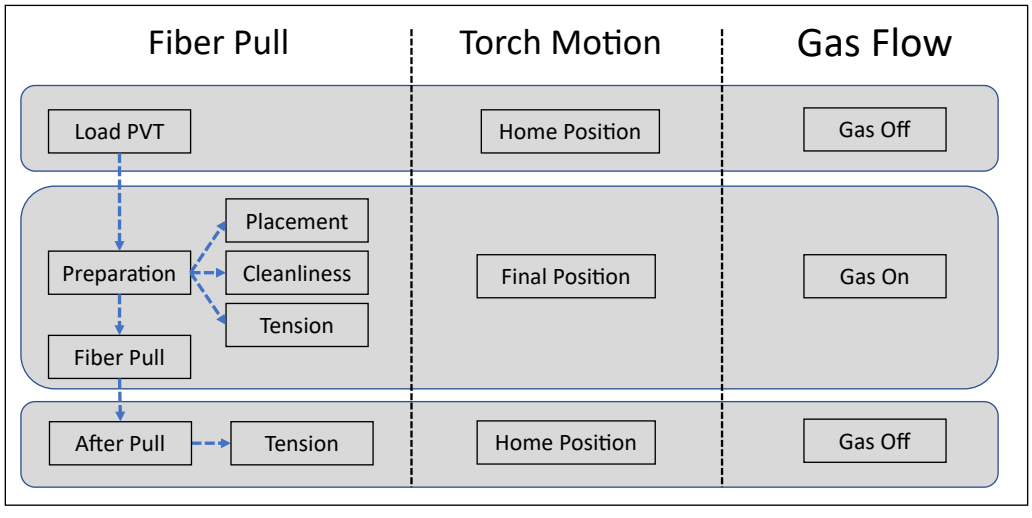

Figure 4.4: The control system has three basic components: fiber pull, torch motion, and gas flow. The horizontal gray rows indicate the action during the progression of a pull.

4.4 Fiber Pulling Procedure

The nanofiber fabrication process starts with a single mode non-polarization maintaining fiber. In our experiment we use the 780 HP fiber from Thorlabs. The protective buffer layer is stripped off in a small section typically 1" long and any remaining residue on the surface is wiped off using acetone and then methanol. Acetone helps remove any remaining buffer while the methanol is used to clean off any remaining residue.

The fiber is then mounted onto the motor stages using two New Focus flexure stages. A microscope consisting of a Mitutoyo NIR 5x objective and a Navitar 12x zoom system is used to view the fiber from above. The large zoom range is useful for two key steps: to ensure the fiber properly sits in the v-grooves of the flexure stages and to observe that the fiber is free of contaminants. The v-groove center is used as the alignment reference when aligning the motors to each other therefore it is important for the fibers to sit properly in these grooves. Using the control system, we can move the fiber from left to right to view both v-grooves. An image of this alignment is shown in Figure (4.5). As can be seen, translating the stages in front of the camera indicates proper alignment at this point. We found that clamping down the fiber with the arms of the flexure stages wasn't enough to keep the fiber from sliding during the pull causing errors in the final fiber diameter. To secure the fiber further, we also used an additional clamping arm (Thorlabs PM4) on each mount that added an additional force and eliminated slippage.

Next, the fiber is translated in front of the camera to inspect it for dust or other contaminants deposited on the surface. The zoom is maximally set to view contaminants down to about 5 microns which is limited by our microscope resolution. If contaminants were found, the fiber would be cleaned again using methanol. This procedure was repeated until no contaminants were found. When ready, the pull was started by running the corresponding PVT file as mentioned in the previous section.

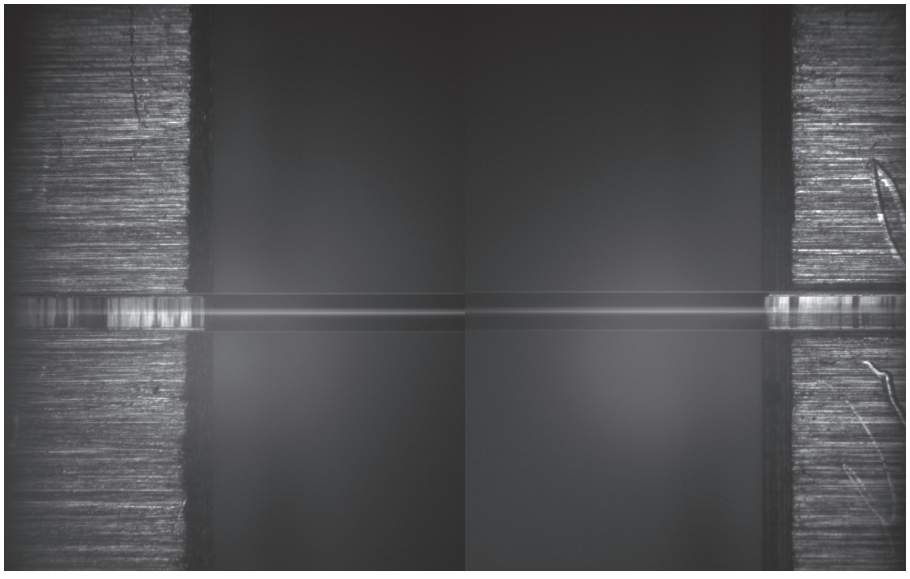

Figure 4.5: The left and right v-grooves are translated in front of the CCD camera to ensure the fibers are properly aligned. This image shows the left and right side of a fiber before being stretched.

After the pull, the fiber sags due to its wait under gravity and the pressure from the torch flame. We added a tensioning step where the fiber can be tensioned in 10 μm steps while observing its profile with a separate microscope.

4.4.1 Transmission Measurements

The transmission of a nanofiber designed with a 2 mrad taper angle, waist length of 5 mm, and a diameter of 430 nm as a function of pulling time is shown in Figure (4.6). To measure the transmission and reduce unwanted noise, a 50:50 fiber beam splitter is used. One arm is coupled into the fiber being pulled and the other is used as a reference. The light coupled into the fiber pulling rig is typically lower than the reference due to coupling losses. During data analysis, we re-scale this signal to match the reference before normalization. A typical result is shown in Figure (4.6). In part (a) the transmission of the fiber for the duration of the approximately 7

minute pull is shown. The red line indicates the point when the pulling stops. The final transmission of the fiber is greater than 99.7% which is typical for our device. Part (b) shows the fast oscillations that appear near the end of the pull. These oscillations indicate spatial mode beating between the fundamental mode and higher order modes [74, 72, 71]. At around 400 s the fast oscillations stop indicating that the fiber diameter has been reduced to the single mode regime where only the HE_{11} mode is supported (see Chapter (2)). The large oscillations observed after the fiber pull has stopped are due to the fiber bending as the flame, and thus the pressure exerted on the fiber, are extinguished electronically.

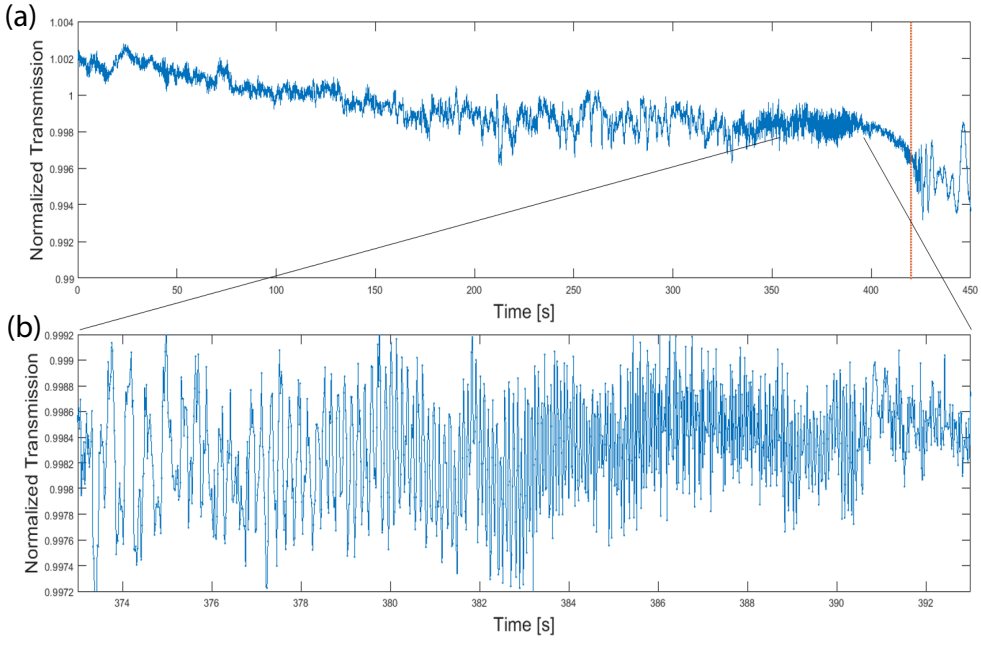

Figure 4.6: Transmission measurement of an 852 nm laser coupled into the fiber during the pull of a 430 nm diameter nanofiber. The transmission signal is normalized to a reference signal. The vertical redline in (a) indicates the end of the fiber pull. (b) is a zoomed in image showing the fast oscillations due to multimode beating.

4.5 Fiber Diameter Measurements

The diameters of the fabricated nanofibers are determined using a scanning electron microscope (SEM). This measurement scheme is destructive because the fibers are coated with gold-paladium in order to make them conductive as part of the measurement process. The metal coating makes them unusable for our experiments, so it is important to ensure our fiber pulling rig can reliably and consistently fabricate nanofibers with predetermined diameters. As an alternative, several groups have focused on developing nondestructive techniques to measure these diameters [79, 80]. Although impressive, these techniques require extra equipment and add to the complexity of the apparatus.

In order to verify the reliability of our device, we fabricated several fiber samples and had their diameters measured. We fabricated a set of 5 samples with designed diameters of 500 μm and a waist length of 10 mm. The measurement results are shown in Figure (4.7)(a). For each sample a subset of about 20 data points were selected for the waist. The average and standard deviations are shown in Figure (4.7)(b). The average of the 5 samples is about 516 nm and is shown as a blue dotted horizontal line. Although there is a small offset when compared to the target 500 nm diameter, there is less than 10 nm standard deviation between samples, showing the reproducibility of fabricating nanofibers with our device. In Figure (4.7)(c) we show samples for nanofibers with designed diameters of 430 nm that were fabricated about 1 year after those shown in (4.7)(a). In (4.7)(d), the average value between samples is about 433 nm shown as a blue dotted line. Here, the standard deviation is within 15 nm of the average sample diameter, showing the reliability of our device.

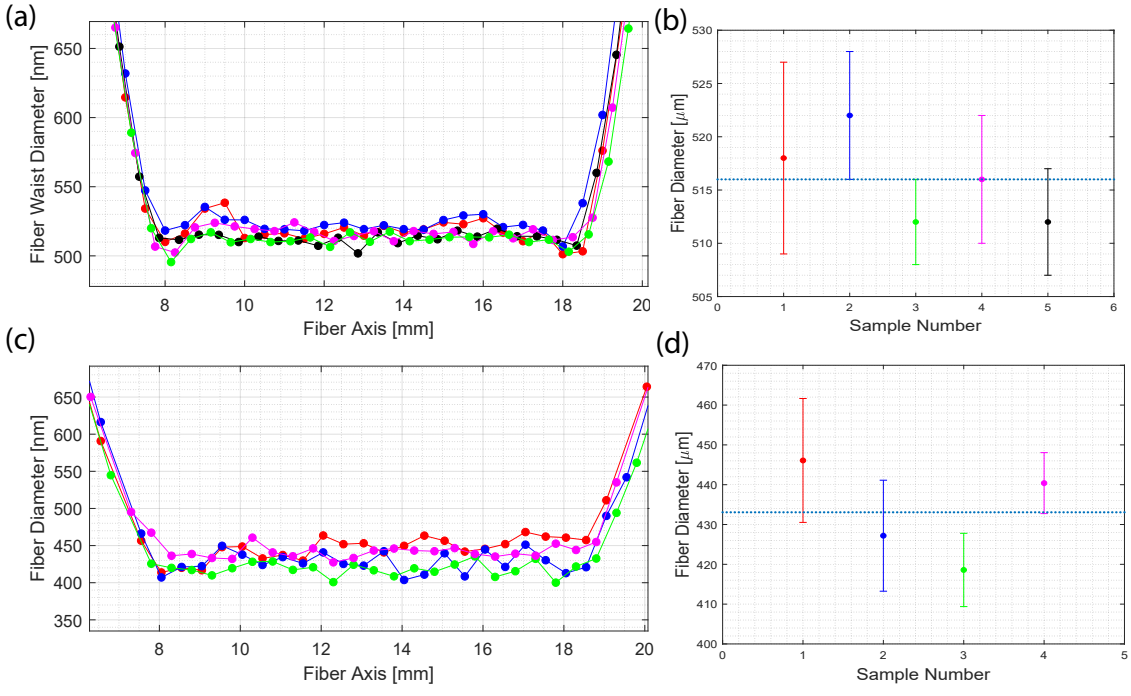

Figure 4.7: Fiber diameter measurement results using SEM for several nanofiber samples fabricated by our nanofiber pulling rig. (a) displays results for a fiber designed to have 500 nm diameter with the average value per sample and the standard deviation shown in (b). The colors in (a) and (b) indicate the same sample. (c) and (d) show results for a fiber designed to have a 430 nm diameter. The samples in (c) were fabricated a year after those shown in (a). The dotted blue line indicates the average diameter for the corresponding set of samples.

Chapter 5

Nanofiber Trap

In this chapter, I discuss the nanofiber experimental apparatus and various laser systems that were built to control and manipulate the source of cesium atoms around the nanofiber. In the first section, I discuss the atom cooling lasers and optics used to generate a source of atoms for the nanofiber trap in a magneto-optical trap (MOT). Next, the nanofiber trap laser optics are presented. The chapter concludes with the details of the main apparatus and experimental data characterizing our nanofiber-based atom trap.

5.1 Magneto-Optical Trap

A trapped cloud of cesium atoms in a magneto-optical trap (MOT) is used as the source of atoms for the nanofiber trap. Therefore a description of how this trap works is discussed in this section with a focus on the relevant concepts important for the nanofiber platform.

As the name suggests, the MOT makes use of magnetic and optical forces to trap and cool atoms. Figure (5.1) shows a conceptual diagram of this process. A

quadrupole magnetic field is produced by two coils in the anti-Helmholtz configuration. The resulting quadrupole magnetic field has a zero point midway between the coils and a linear gradient at distances away from this point. This gradient spatially splits the magnetic sub-levels of the atom which is exploited by properly setting the polarization and detuning of the cooling beams. Setting the polarization to σ_+ or σ_- ensures the atoms stay in a cycling transition. This is due to the dipole selection rules $\Delta F = 0, \pm 1$. For the transitions $J \to L + 1/2$, exciting the highest level in the excited state manifold results in spontaneous emission to the highest ground state manifold [46]. For cesium this is the transition $\left|6S_{1/2}, F = 4\right\rangle \to \left|6P_{3/2}, F' = 5\right\rangle$. Additionally, setting the detuning below resonance makes it more likely for atoms moving toward the laser beam and in the opposite direction of the cooling k vector to Doppler shift into resonance gaining a momentum kick $\hbar k$ in the opposite direction to their initial motion.

In trap in three dimensions, three counter-propagating pairs of laser beams are used. Atoms on either side of the zero-point will come into resonance if they are moving away from the trap center and spontaneously radiate resulting in a momentum kick that drives them back toward the center of the trap. Atoms with a position $\vec{r}$ and velocity $\vec{v}$ close to the center of the MOT experience a force that can be described by a damping and position dependent contribution [46].

$$\vec{F} = -\beta\vec{v} - \kappa\vec{r} \tag{5.1}$$

where β is the damping constant and κ is the spring constant. There are two different timescales describing the atom motion. A slow time scale that results from the damping motion that is on the order of several ms. A fast time scale on the order of nanoseconds is due to spontaneous emission. Loading of atoms into the nanofiber takes several milliseconds (as discussed in section (5.4)). Compared to the ms loading time, this interaction is essentially continuous. Therefore reducing the MOT parameters (quadrupole field and repump and cooling beam intensities) optimizes the loading process [81, 28]. In addition, reducing these quantities results

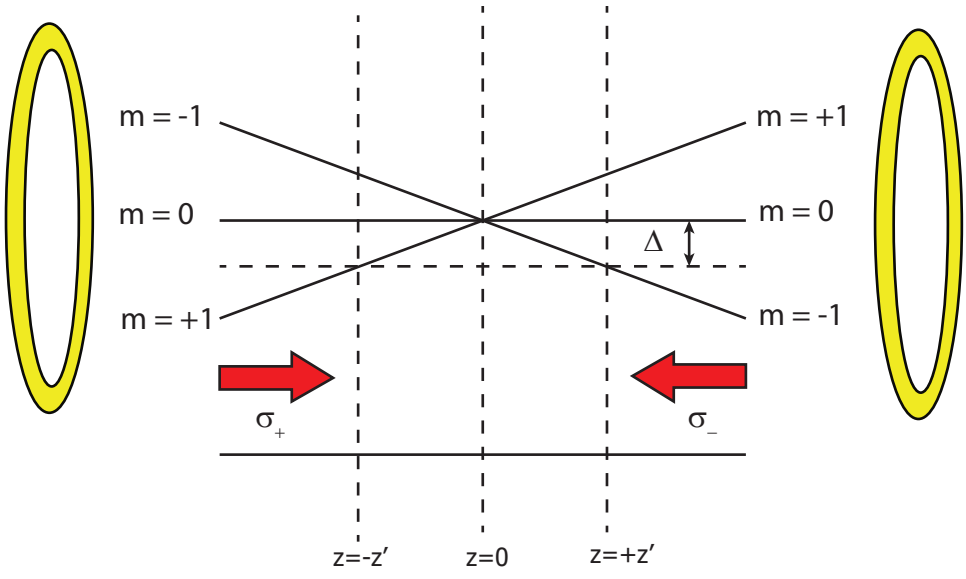

Figure 5.1: Energy level diagram with an idealized $J = 0$ to $J = 1$ transition too show important concepts. The two anti-Helmholtz coils are depicted by yellow rings. We focus on the symmetry access of the quadrupole field. Away from $z = 0$ the magnetic sub-levels experience a Zeeman shift. For atoms in a position $z > 0$ the laser is closer to resonance for σ_- transitions.

in polarization gradient (PG) cooling, reducing the atom temperature.

The MOT is implemented using two coils of around 40 turns each being driven by 4 A producing a gradient of about 10 G/cm. The cooling beams are sourced from an 852 nm TAPro Toptica laser. This laser consists of an external-cavity diode laser (ECDL) and tapered amplifier and is set to output about 500 mW. With this setting, we get 12 mW out each MOT cooling beam that has a 15 mm $1/e^2$ diameter. The cooling beams are in a retro-reflection configuration which makes alignment easier and reduces the complexity of the optics system. However, we find that there is an intensity imbalance between the two counter propagating beams due to transmission losses through the cell. Although the cell has anti-reflection coating on the outer surfaces, reflections from the inner surfaces reduces the relative intensity

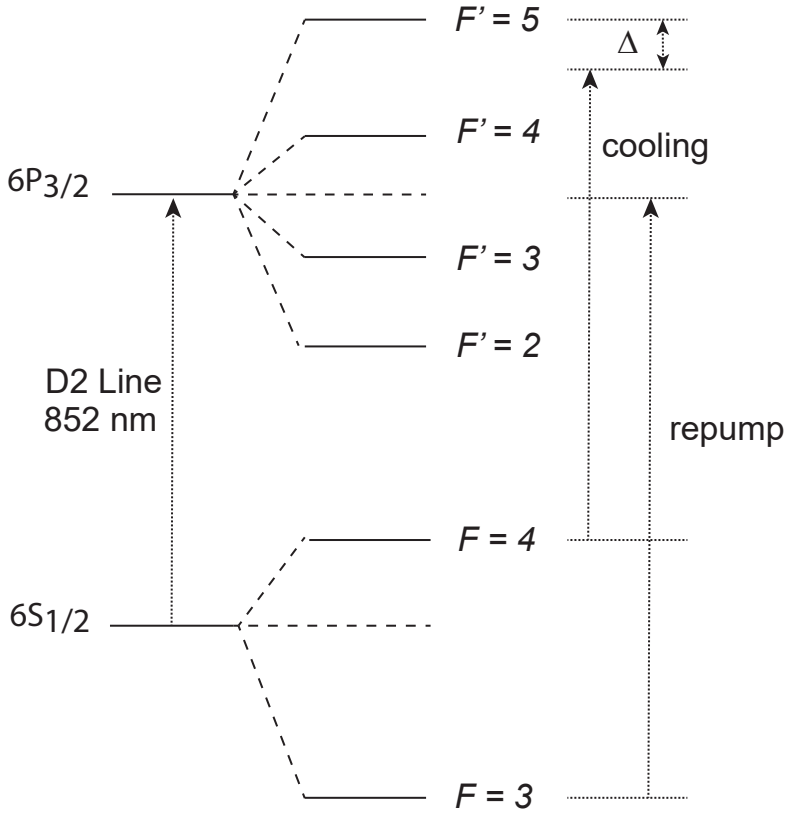

Figure 5.2: The relevant energy levels for the operation of the magneto-optical trap. The cooling beam is detuned from the $\left|6P_{3/2}, F' = 5\right\rangle$ transition and the repump pumps atoms that fall in the $\left|6S_{1/2}, F = 3\right\rangle$ state.

of the transmitted and reflected beams by about 15%. In steady state, the MOT cloud is centered on the nanofiber, however during ramping down of the cooling beam intensities for PG cooling, the MOT can shift due to this imbalance. In order to reduce this effect, we intentionally focused down the MOT beams to increase the intensity of the reflected beam with respect to the initial beam.

The cooling laser is locked using saturation spectroscopy and an electro-optic modulator (EOM). The relevant energy levels are shown in figure (5.3). A 10 MHz detuning below the $6P_{3/2} : |F' = 5\rangle$ hyperfine transition is used. We sweep the red-

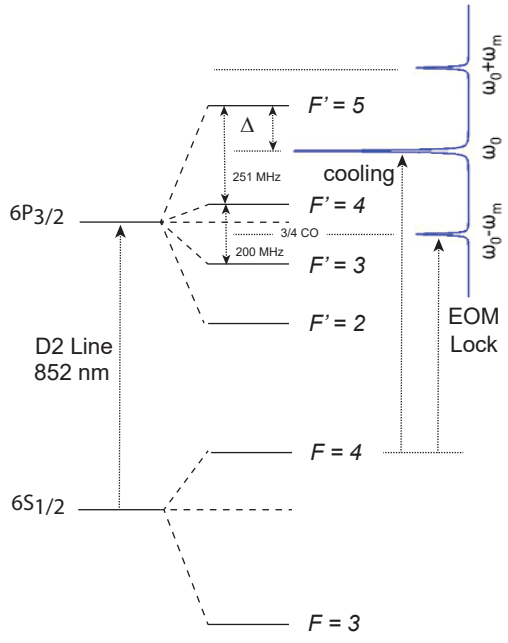

Figure 5.3: The energy levels used to lock the cooling beam laser using an EOM for large detuning sweeps of the cooling beams are shown. The carrier ω_0 is modulated at a frequency ω_m such that the detuning $\Delta = 10$ MHz. The -1 sideband is locked to the $F' = 3 \rightarrow F' = 4$ crossover. When the modulation frequency changes, the -1 sideband remains locked and the carrier frequency follows.

detuning by 60-80 MHz for the loading step for nanofiber atom trapping (see section (5.4)). The EOM modulates the input beam to the spectroscopy module (Vescent D2-210) with a frequency ω_m. After modulation, the -1 sideband is locked to the $F' = 3$ to $F' = 4$ crossover transition [47]. As the modulation frequency is changed, the carrier frequency changes accordingly to remain locked. In order to sweep the detuning on a ms timescale, the servo modulates the laser current. We find that we can sweep up to 80 MHz to the red for a minimum of 1-2 ms. Sweep times below this result in losing the lock. A limitation of this technique is the overlapping of several transition peaks during the frequency ramp. For instance, we modulate the cooling beam at 340 MHz. The FWHM Doppler width of the D2 line is about 380 MHz at room temperature, so there is overlap between the different saturation peaks

generated by each EOM frequency. While ramping, the modulation frequency is decreased resulting in a larger overlap between the Doppler broadened peaks. When two peaks cross the lock is lost. We find that we can still sweep the frequency up to 80 MHz without two peaks ever crossing. An improvement of this technique would be to use an etalon to filter out the desired sideband (-1 in our case).

Due to the small detuning of the cooling beams, the atoms can fall out of this transition and the repump is used to pump them back into the cycling transition. The repump laser is realized using a DLC Pro from Toptica with a maximum output of 40 mW. It is coupled into the same path as one of the cooling laser beams using a 2x2 evanescent fiber optic coupler (Evanescent Optics) and has a power of 0.5 mW at the experiment.

5.2 Nanofiber Trap Laser System

The nanofiber trapping lasers are 937 nm and 685 nm and are near the magic wavelengths of 686.8 nm and 935.5 nm [58, 82, 28]. Both of our trapping lasers are not frequency locked and are allowed to free run in order to simplify the optics system. The 937 nm laser is a Photline distributed feedback (DFB) laser with a linewidth of about 1 MHz. The 685 laser is an ONDAX volume holographic grating which results in a linewidth < 50 MHz.

The trapping laser's power and polarization need to be optimized for the nanofiber trap. In order to optimize these parameters, we use motorized Thorlabs rotation mounts (ELL14K) that are controlled using our control system. By rotating the polarization of the trapping laser entering the fiber and monitoring the absorption, we can optimize the polarization. Each trapping laser has polarization control optics which is either a Berek compensator or a quarter-waveplate and half-waveplate combination (see section (5.4.1)).

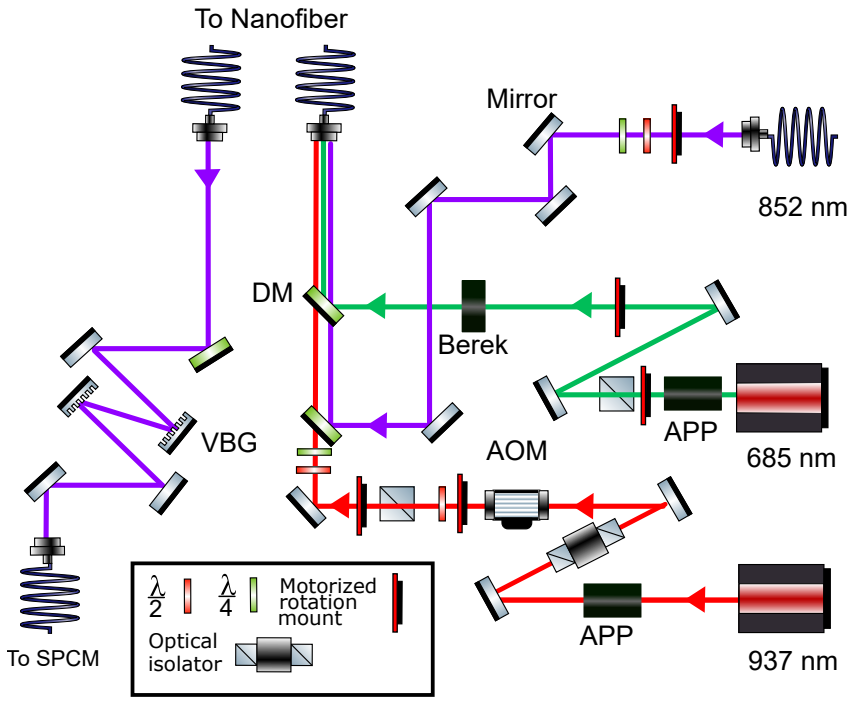

Figure 5.4: Diagram of the trapping laser optics.

5.3 Apparatus

The experimental apparatus sits inside a MuMETAL shield with dimensions 20" x 20" x 28" to shield the experiment from any stray environmental magnetic fields. The apparatus consists of a small vacuum system with several components: a 5 L/s ion pump (Heatwave), cesium dispensers (SAES), and a custom glass cell from Precision Glassblowing (Figure (5.6)). After baking the chamber at about 130 °C, the 5 L/s ion pump is sufficient to maintain an ultrahigh vacuum pressure (UHV) of around $1\text{x}10^{-9}$ Torr. Using UHV pressures helps reduce collisions between atoms in the background gas and atoms in the MOT or nanofiber trap. The cell is designed with an extended cylindrical end in order to get a 1" diameter bend of the nanofiber to reduce optical attenuation due to bending losses as shown in Figure (5.5). The small vacuum chamber sits on top of a Newport xy translation stage and a Newport

lab jack. The lab jack has a maximum translation of 76 mm. The xy stage has a maximum translation of 25 mm. This is adequate to optimize the atom cloud and fiber overlap (see section (5.4)) The fiber is mounted on a custom 3-D printed titanium mount (Protolabs) which mounts onto a 1" stainless steel tube as shown in Figure (5.5). The nanofiber mount was designed to detach from the adapter piece

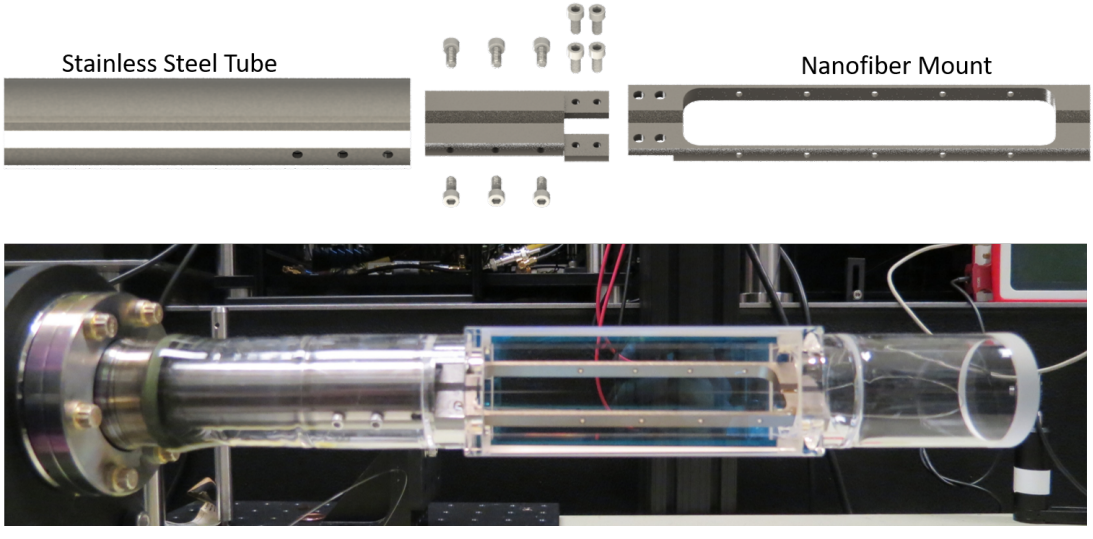

Figure 5.5: The custom glass cell for the nanofiber experiment is shown. The cell was designed with an extended cylindrical glass component to allow the fiber to bend with a minimum of 1" diameter to reduce attenuation due to bending losses.

used to attach it to the SS tube. This design made mounting the fiber much easier after fabrication due to the symmetric position of the pulling motors with respect to the fiber waist (see chapter (4)). A Kimball physics groove grabber was used to fix the SS tube onto a 2-3/4" CF flange. This design was chosen for its rigidity in an effort to reduce high frequency vibrations of the nanofiber.

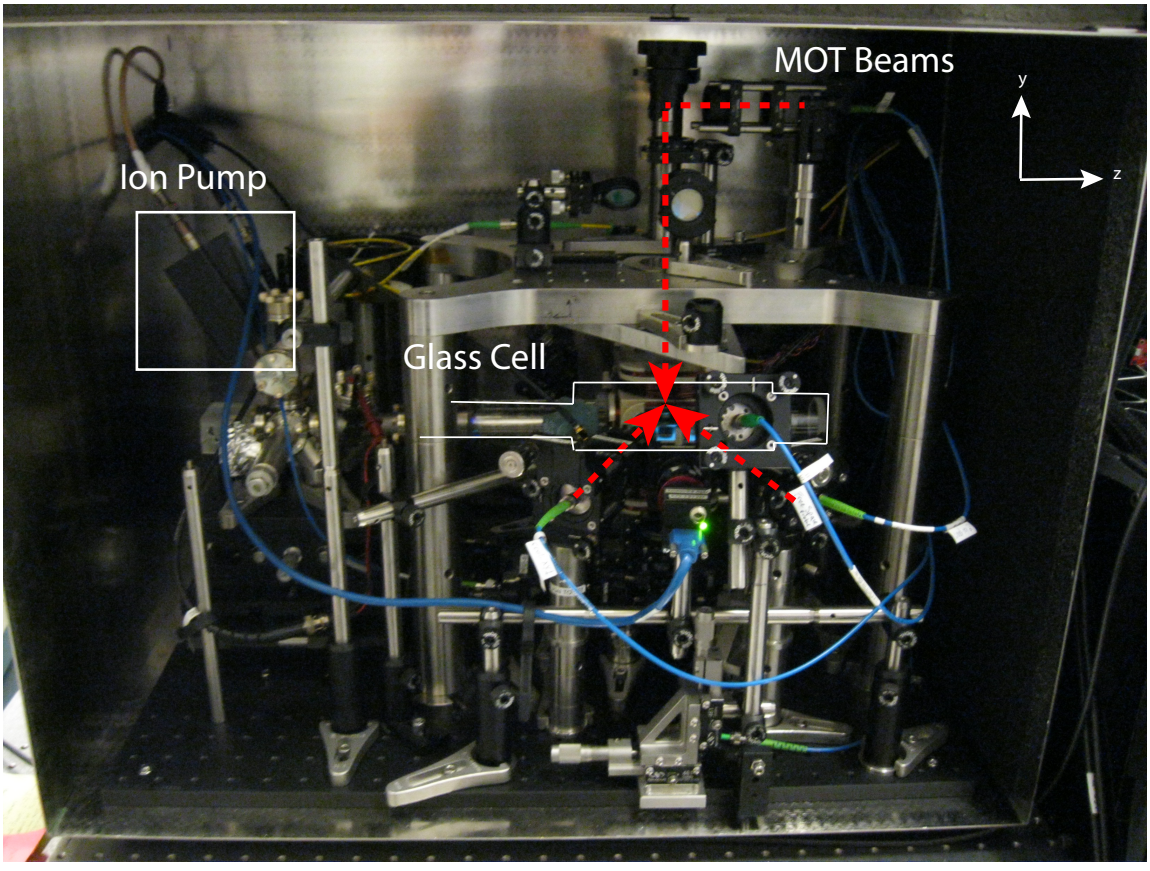

Figure 5.6: Diagram representing the core components of the fiber pulling rig.

5.4 Trapping Atoms around a Nanofiber

It's important to maximize the atomic density of atoms around the nanofiber to increase the probability of trapping them. The absorption of a resonant fiber guided probe can be used to optimize the atomic cloud and nanofiber overlap [83]. For this procedure it is important to have the capability of translating the small vacuum chamber and thus the nanofiber with respect to the atomic cloud. The absorption of the probe laser is monitored while shifting the nanofiber transverse to the fiber axis. The probe signal is monitored using a single photon counting module (SPCM). The nanofiber is translated while monitoring this signal until the absorption is maximized.

5.4.1 Polarization of Guided Light

Impurities or surface imperfections at the nanofiber surface allow the measurement of the polarization of the nanofiber guided field [27, 84]. These scatterers emit Rayleigh scattered light in a dipole radiation pattern. The intensity of the radiation for linearly polarized light follows $I(\phi) \propto \sin(\phi - \phi_0)$. To measure the polarization, we used two orthogonally placed cameras equipped with polarizers. For instance, for camera 1, $\phi_0 = 0$ and for camera 2, $\phi_0 = \pi$. Each camera is used to measure the polarization in the transverse plane (xy plane). The polarizers are necessary to block the z-component of the fundamental mode [27]. The measurement consists of taking images of the nanofiber and defining a region of interest (ROI) and then summing the total pixels which is proportional to the intensity of the scattered light. The polarization of the input light to the nanofiber is rotated over a full oscillation (typically 0 to 2π) using a half waveplate mounted on a computer controlled rotation mount. The data for a single run using the 937 nm laser is shown in Figure (5.7). A measure of the visibility indicates the degree of linear polarization [84]. The visibility is defined as

$$V = \frac{I_{max} - I_{min}}{I_{max} + I_{min}} \tag{5.2}$$

where I_{max} is the maximum intensity measured and I_{min} is the minimum intensity measured. For the data in Figure (5.7), the calculated visibilities were $V_{horiz} = 0.9$ and $V_{vert} = 0.8$. The discrepancy between these values could be attributed to the alignment of the polarizers in front of each camera. Here vertical indicates polarization along the y axis and horizontal along the x axis as defined in Figure (2.1).

In our experiment, we consistently observed a suboptimal visibility. In [84], further analysis of the polarization indicates that the radiation pattern differs from the free space case. In addition, the maximum visibility is dependent on the wavelength of the light. The pattern is modified due to the distribution of scatterers on the

surface or the bulk of the nanofiber.

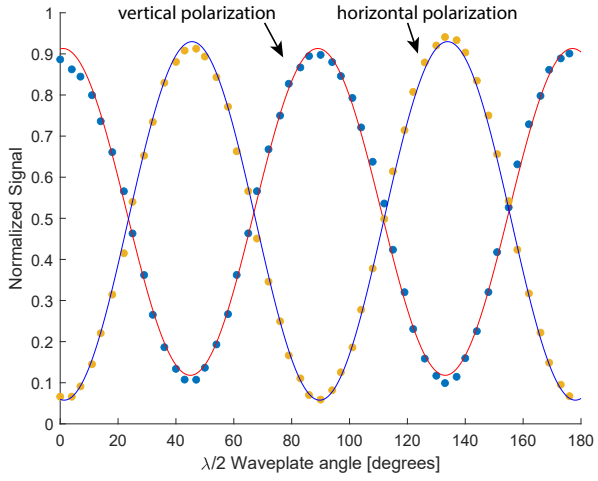

Figure 5.7: The visibility is calculated from each camera signal and plotted against the rotation angle of a motorized waveplate mount.

5.4.2 Trap Loading Sequence

The experimental sequence for loading atoms into the nanofiber trap and there subsequent measurement involves two steps: the MOT loading stage and the absorption measurement. The loading stage involves overlapping the MOT cloud with the nanofiber. During this stage, we reduce the quadrupole field, cooling beam intensity, and repump intensity at the same rate linearly. For our goal of trapping atoms and performing coherent control, we would like to optimize the total number of trapped atoms which involves both having a short loading time and strong absorption signal. The short loading time allows higher repetition of experiments to build up statistics. A larger absorption signal indicates there are more trapped atoms. While optimizing the loading stage, we tried to ramp down the MOT parameters both linearly and exponentially. We found that for millisecond timescales a linear ramp was beneficial in controlling inductive oscillations from reducing the MOT coil current. When using

exponential ramps, we found that a longer load time was needed for the quadrupole field to damp out.

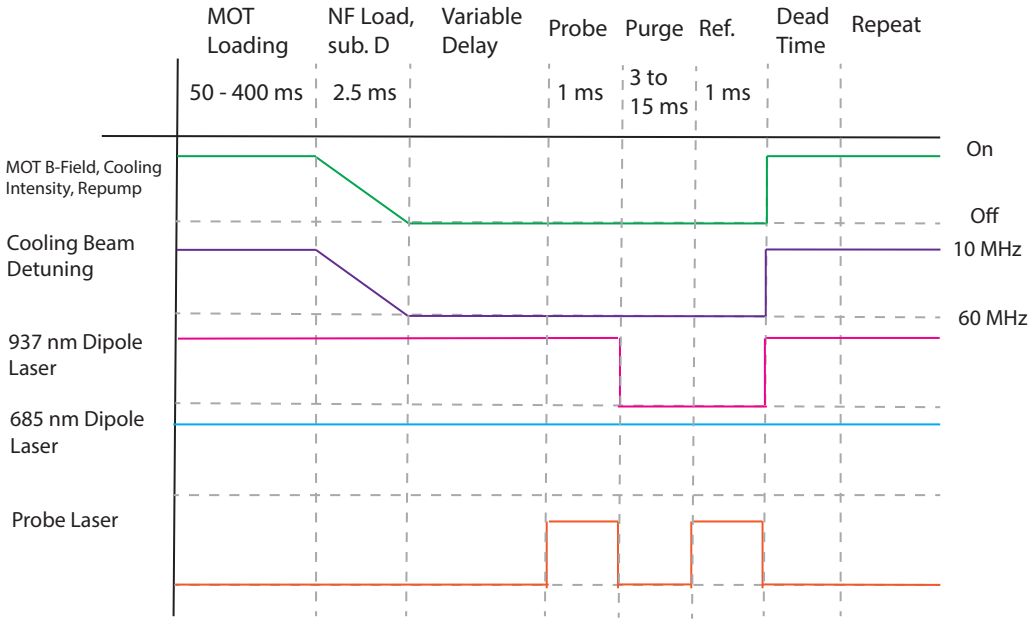

Figure 5.8: The experiment timing sequence showing the change in the experimental parameters for loading the nanofiber trap.

5.4.3 Absorption Spectroscopy of Trapped Atoms

To measure the number of trapped atoms, a probe resonant with the $6S_{1/2}$ F = 4 $\rightarrow$ $6P_{3/2}$ F' = 5 D2 transition is coupled to the nanofiber. As the resonant fiber guided probe travels through the nanofiber trapped atoms, it is absorbed. As more atoms are trapped around the nanofiber, we see a stronger absorption of the probe signal. In figure (5.9) we plot the absorption signal immediately after loading the nanofiber trap. The transmission of the probe as a function of its detuning is given by [27, 85].

$$T(\Delta) = \exp\left(-\frac{\mathrm{OD}}{1+(2\Delta/\Gamma_0)^2}\right) \tag{5.3}$$

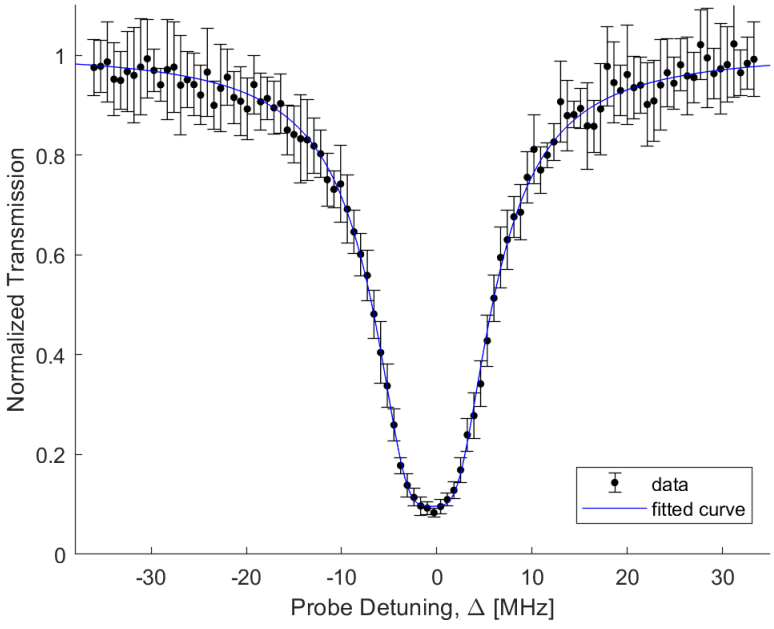

Figure 5.9: Transmission of a fiber guided probe as a function of frequency. The absorption signal is measured immediately after loading the nanofiber trap.

where OD is the optical depth, $\Delta = \omega - \omega_0$ is the detuning from resonance with ω being the probe laser frequency and ω_0 the atoms resonant frequency in free space, and $\Gamma_0 = 5.2$ MHz is the natural linewidth of the transition. A curve fit of the data in figure (5.9) with an equation with the same form as (5.3) is used to determine the atom number. The fit function used is $T(\Delta) = a\exp\left(-\frac{b}{1+(2\Delta/\Gamma_0)^2}\right) + c$. The fit results in OD $= 5.5 \pm 0.3$ which can be used to infer the total number of trapped atoms by calculating the optical depth per atom, $\mathrm{OD}_{\mathrm{atom}} = \sigma_0/A_{\mathrm{eff}} = 0.08$. The effective mode area was calculated at the trap minimum (260 nm from the fiber surface) and is $A_{\mathrm{eff}} = 4.36\,\mu m^2$ and the atom's resonant absorption cross section is $\sigma_0 = 3\lambda^2/2\pi = 0.35\,\mu m^2$. The total atom number is then $\mathrm{N} = \mathrm{OD}/\mathrm{OD}_{\mathrm{atom}} \approx 70$ atoms.

5.4.4 Trap Lifetime

The trap lifetime is measured by varying the delay time between loading the trap and detection. Detection is performed by measuring the transmission of a fiber guided probe field resonant with the $|F = 4\rangle \rightarrow |F' = 5\rangle$ D2 transmission. The probe pulse is typically 1 ms long (see Figure (5.8)). As the delay increases, atom heating mechanisms in the trap raise the temperature of trapped atoms causing them to overcome the trapping potential and be ejected. It is important to note that our trap lifetime has not been consistent. We have had successes in reaching trap lifetimes up to almost 26 ms but typically it is in the 7-10 ms range. In order to investigate this effect, we have applied two different trap configurations to increase the lifetime. First, we couple two independent free-running counter-propagating blue detuned fields in order to increase the trap depth. These fields are generated from two independent lasers and are free running so we don't expect a standing wave.

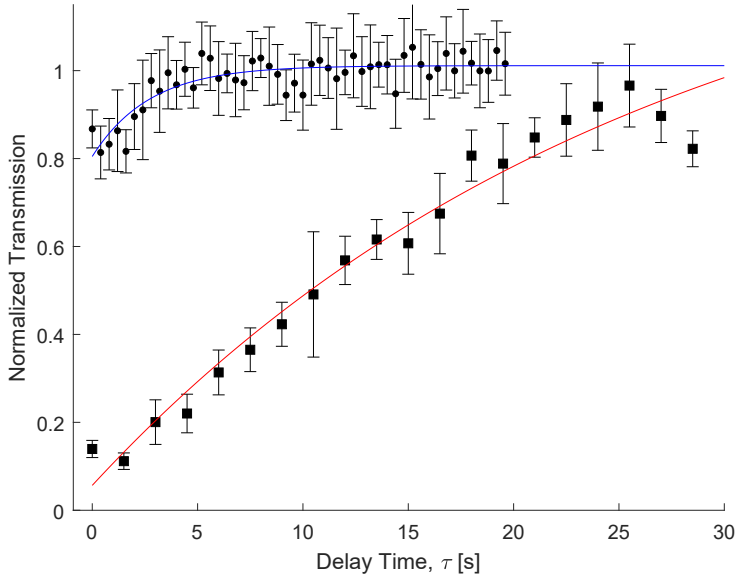

Figure 5.10: The lifetime of the nanofiber trap decays with a characteristic time of 26 ms while that of the MOT cloud is about 2 ms.

Second, following the work of [1], it was shown that the lifetime of the nanofiber trap can be increased by reducing the total trap laser power while keeping their ratio fixed. We found that using two beams results in longer trap lifetimes due to increasing the trap depth and use this method for most of the experiments in this thesis. A figure of the data collected is shown in Figure (5.10). The characteristic 1/e time was obtained from fitting the data to an exponential of the form a*exp(-x/b)+c with fitting parameters a, b, and c, red curve in the figure. Additionally we measured the signal from the MOT atom cloud and found a characteristic decay of 2 ms. This value depends on the density of the MOT cloud and can vary depending on the current running through our cesium dispenser.

5.5 Microwave Control of Trapped Atoms

The coherent control of atoms trapped around a nanofiber has been studied using microwaves [64] and nanofiber guided Doppler free Raman beams [29, 86]. In this chapter, we discuss the microwave coherence control of atoms using our magic wavelength nanofiber trap and our efforts toward building up a Raman laser system to interrogate the trapped atoms using free space beams and in the future, fiber guided fields.

To generate the microwave frequency at the hyperfine frequency ω_{HF} for cesium, we used a low noise 9.2 GHz dielectric resonator (DRO) from Microwave Dynamics (PLO-2000-09.20) and mix it with a signal from a direct digital synthesizer (Novatech 409b) output using a single sideband mixer from Polyphase Microwave (SSB70100A). The required 10 MHz clock input for the DRO is generated from a Rb atomic clock source. A schematic of the RF circuit is shown in Figure (5.11). The output is shared between the microwave horn and the Raman electro-optic modulator (EOM). A high frequency switch (UMCC SW-S010-2S) is used to change the output to the Raman EOM or the microwave horn using a TTL signal from the control system (see chapter

(4)). The signal is amplified and sent to the corresponding unit. The microwave horn (Narda) is placed near the cell ≈ 3" from the MOT cloud. The observed π times are around 80 μs. To see a signal from the atoms trapped around the nanofiber, it

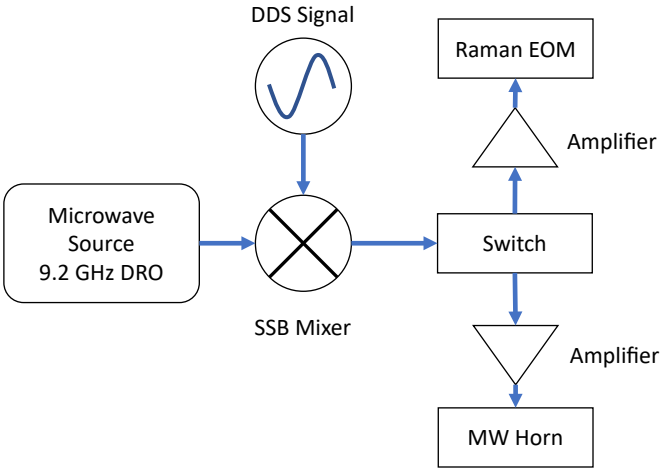

Figure 5.11: A single RF chain is used as source for both the Raman and microwave fields. A low phase noise dielectric resonator (DRO) at 9.2 GHz is mixed with a DDS signal using single-sideband mixer. The -1 sideband is used. The output is fed into a high frequency switch where both or one output can selected with a TTL signal.

is important to be able to distinguish between atoms trapped around the nanofiber and MOT atoms. In order to distinguish between them, we can either make use of a long lifetime compared to the motion of the falling MOT cloud or implement a distillation procedure. In the following subsections, I discuss the implementation and result of these procedures.

5.5.1 Falling MOT Cloud

The atom cloud generated by our MOT has a $1/e^2$ diameter of 0.5 mm. If properly centered around the fiber, it would take about 7 ms to fall out of the nanofiber area, no longer contributing to the absorption signal. In section (5.4.4), we measured the

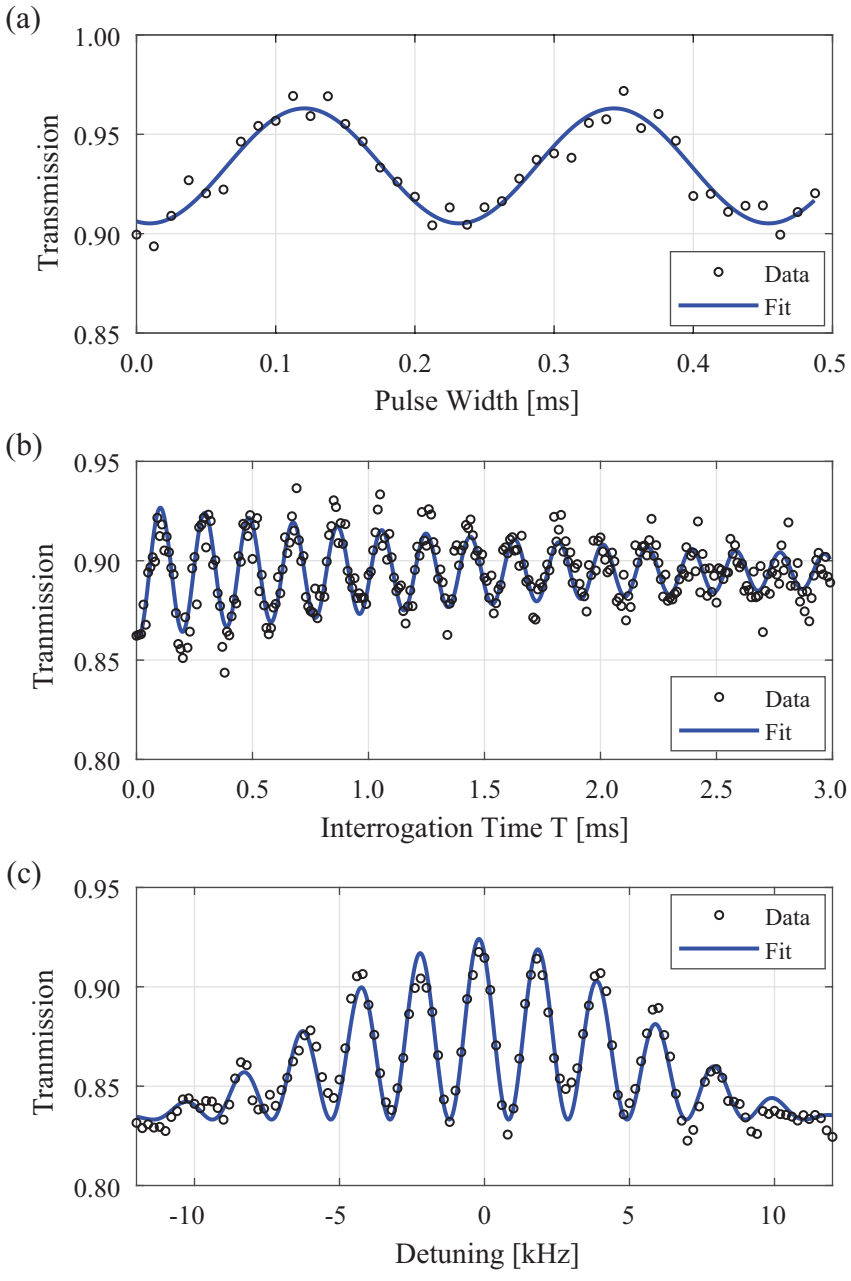

Figure 5.12: (a) Microwave Rabi oscillations of nanofiber trapped atoms. $T_{2\pi} = 222.5 \pm 3.2$ μs. Although not shown, the signal decays with a 1/e time of $\approx$ 1 ms. (b) Microwave Ramsey interferometry as a function of the interrogation time scan (δT). The Ramsey sequence is $\pi/2 - T + \delta T - \pi/2$. The coherence time $T_2^* = 2.3 \pm 0.2$ ms. The microwave $\pi/2$ pulse time is $\approx$80 μs. (c) Ramsey sequence while scanning the microwave frequency. The interrogation time T is $\approx$ 0.5 ms, and the frequency separation in the Ramsey fringes is $\approx$ 2 kHz. The normalized transmission was measured with a guided absorption probe for all the measurements shown.

reduction of the MOT cloud absorption signal to be 2 ms, ($1/e$ characteristic time). This is faster than the expected 7 ms and is likely due to thermal expansion. The atoms have a finite temperature, and while in free fall, thermal expansion reduces the density of atoms around the nanofiber. The difference in time scales between the MOT cloud absorption signal and the nanofiber trap lifetime allows a distinction between these two signals. Using a time delay between loading the nanofiber trap and the atom state manipulation, we apply microwave spectroscopy to study the microwave coherence.

In the experiment, atoms are first loaded into the nanofiber trap after which a delay of typically 10 ms is added before atomic state manipulation with microwaves. The delay insures that spectator atoms initially trapped by the MOT are not contributing to the nanofiber trap signal and allows adequate time to ramp up the magnetic field to define a quantization axis. An optical pumping step that includes a free-space repump and depump beam is applied after this delay for 600 us. The depump beam is resonant with the $6S_{1/2} \rightarrow 6P_{1/2}$ D1 transition. It is important to optically pump the atoms to increase the atomic coherence signal. The atoms are optically pumped to the magnetically-insensitive $|F = 4, m = 0\rangle$ ground state.

Figure (5.12) shows the results for Rabi and Ramsey experiments. To obtain this data, we divide out the decaying signal due to the nanofiber trap lifetime from the raw signal. In Figure (5.12)(a), we show microwave Rabi oscillations with a $\mathrm{T}_{2\pi} = 222\ \mu$s. The small transmission signal is due to the decrease in nanofiber trapped atoms due to the delay. We also apply a Ramsey sequence of $\pi/2 - T - \pi/2$ to measure the inhomogeneous decay time T_2^*, where T is the interrogation or waiting time. The results are shown in (5.12)(b). A fit to the data with a sinusoid and a decaying exponential envelope give a $T_2^* = 2.3$ ms. In addition, we perform a frequency sweep of the microwave signal for the Ramsey sequence as shown in (5.12)(c). The frequency separation between the Ramsey fringes is ≈ 2 kHz.

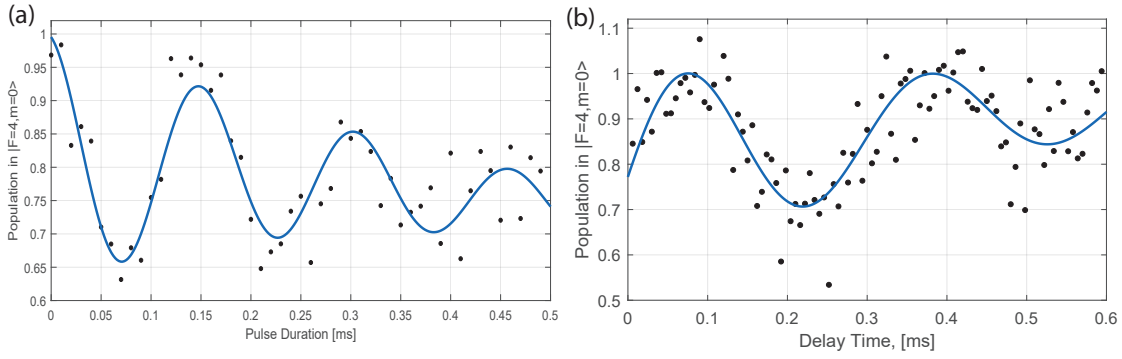

Figure 5.13: (a) Microwave Rabi oscillations of nanofiber trapped atoms. The oscillations decay in a characteristics 1/e time of 300 μs.(b) A Ramsey sequence applied to nanofiber trapped atoms using microwaves shows the signal decay on a time scale similar to the Rabi oscillations of 350 μs.

5.5.2 Distillation Procedure

The longest nanofiber trap lifetime measured in our experiment was 26 ms (see section (5.4.4)). However, the lifetime was not consistent from day to day. The lifetime of the trap was more often $\approx$ 7-10 ms. Optimizing the trap took several hours and yet the longer lifetime of 26 ms was still not attainable some days. The cause of this inconsistency is still under investigation. Additionally, the transmission of the fiber used in the experiments in section (5.5.1) degraded and a new fiber had to be installed. The fiber showed localized scattering in the tapered region that were not present when the fiber was first installed. The cause of these scattering spots was not found. The inconsistency with the lifetime has also been observed in other dissertation research involving a magic wavelength nanofiber trap. In [55] it is mentioned that the lifetime varied from 100 ms down to less than 10 ms. Some of the possible explanations of the drop in power is heating of the nanofiber leading to increases in mechanical vibrations. The vibrations could have a larger effect here and in [55] due to a smaller nanofiber diameter than in [27] where lifetimes of $\approx$ 100s of ms were observed. In our trap, vibrations of the nanofiber are also present and seem to depend on the blue trap beam power however, a more rigorous study

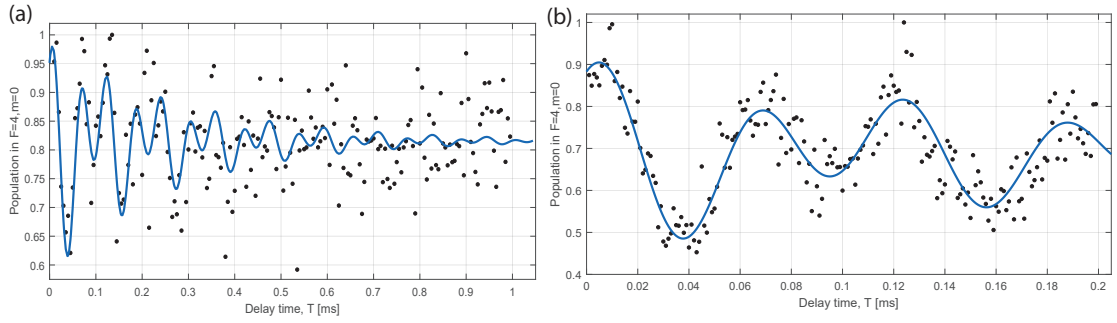

Figure 5.14: (a) A microwave echo pulse sequence applied to the nanofiber trapped atoms shows a characteristics decay of 400 us. (b) A closer scan of the echo sequence showing the doubly period structure.

wasn't implemented. Due to the limitations mentioned above, we implemented a preparation procedure to eliminate the need to wait for the MOT atoms to fall out of the nanofiber area. We dubbed this procedure "the distillation procedure". First, cesium atoms are loaded into the trap with most of the population in the F=4 manifold. Next, a fiber guided 895 nm laser beam locked to the $|F = 4\rangle \rightarrow |F' = 4\rangle$ D1 transition is pulsed on for 500 μs to optically pump atoms around the fiber to the F=3 manifold. The polarization of this field is unknown and mostly likely not quasi-linear (see chapter (2)). Afterward, a quantization axis along y is turned on and a σ_- polarized free space push-out beam propagating along this same axis is pulsed on for 40 μs. This laser is resonant with the D2 $|F = 4\rangle \rightarrow |F' = 5\rangle$ transition and blows away any atoms left in the F=4 manifold. A free space depump and repump beam is then turned on to optically pump atoms to the $|F = 4, m = 0\rangle$ state for 500 μs. The distillation procedure takes about 1 ms to perform. With this procedure we are able to remove MOT atoms and keep atoms trapped around the nanofiber.

After implementing the distillation procedure, we performed microwave experiments to characterize the coherence of the nanofiber trapped atoms. First we performed Rabi and Ramsey experiments. In Figure (5.13)(a), decaying Rabi oscillations were observed with a 1/e time constant of 300 μs.

5.6 Raman Laser System

The Raman laser system (see Figure (5.15)) consists of a DBR laser at 852 nm (Vescent D2-040-DBR) that is amplified using a tapered amplifier (BoosTA, Toptica Photonics). With this system we can generate more than 500 mW of laser power. However, for our current system, we only use about 120 mW at the output of the TA. The single photon detuning is controlled via an offset lock. The Raman laser is overlapped with a pick-off of the repump laser using a evanescent fiber coupler (Evanescent Optics Inc.) and directed to a fast photodiode. The RF beatnote signal is amplified and sent to a Vescent D2-135 servo to offset lock the Raman and repump

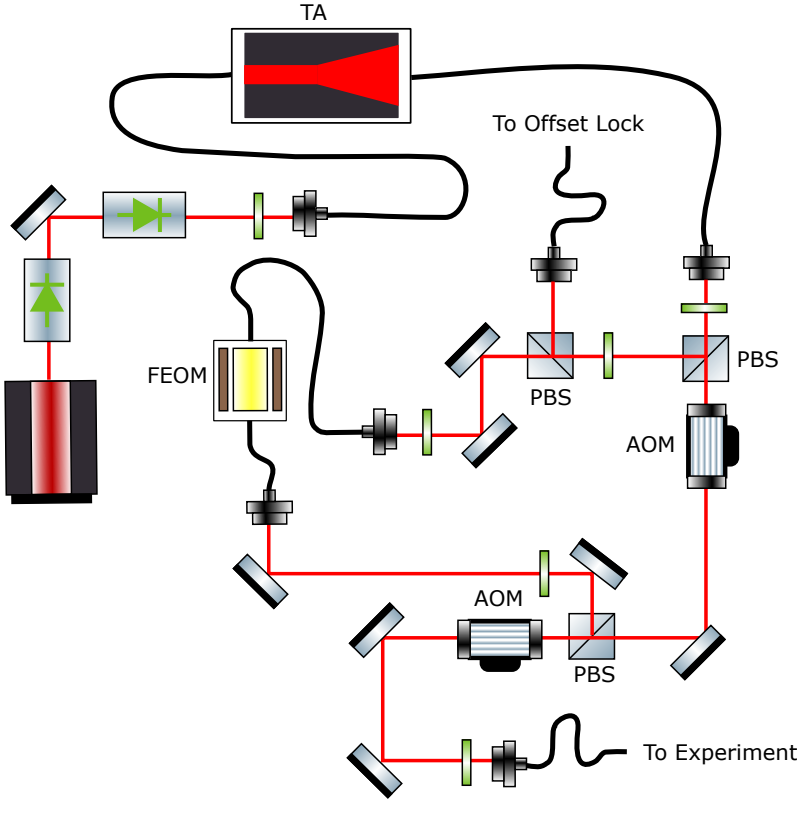

Figure 5.15: The Raman laser system is shown. TA : Tapered Amplifier, FEOM : Fiber Electro-Optic Modulator, PBS : Polarizing Beam Splitter, and AOM : Acousto-Optic Modulator.

lasers.

A 100 MHz signal derived from the same Rb clock source used for the 9.2 GHz DRO (see section (5.5)) was used as a reference to the offset servo. With this servo, the offset frequency can be set at multiples of the clock frequency. For our experiments, the Raman beams are 800 MHz detuned below the D2 transition in cesium.

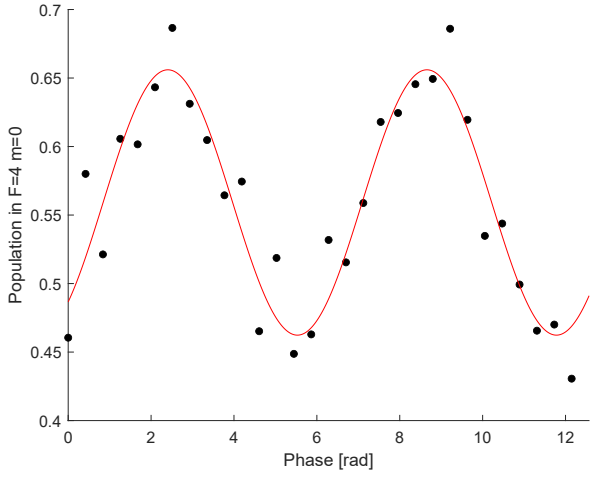

Figure 5.16: Three pulse sequence applied while scanning the phase of the last Raman pulse. The black dots are data from a single run of the experiment and the red curve is a fit to the data. The interrogation time T = 2 ms and the π pulse time was 5.5 μs giving a Rabi frequency $\Omega = 2\pi$ 91 kHz.

To prepare our system for use with the nanofiber trapped atoms, we applied a three pulse atom interferometry sequence ($\pi/2 - T - \pi - T - \pi/2$) to the MOT cloud. The beams are oriented horizontally, so we expect the signal to be independent of the gravitational acceleration and hence do not observe a chirped sine wave [10]. In figure (5.16), results are shown for a interferometric sequence with a constant interrogation time, T = 2 ms, where we scan the phase of the last pulse. With this system, we have applied the interferometric sequence onto nanofiber trapped atoms but haven't observed a coherent response. With our studies of the coherence using

Microwaves, it is likely that this issue is technical in nature and atomic coherence is not a limiting factor.

Chapter 6

Waveguide on a Chip

The nanofiber has been a successful platform for trapping neutral atoms using only optical fields [27, 28]. However, such traps have not yet been realized using all-optical waveguides fabricated on chips which have a much desired property of scalability. In this chapter, I discuss several designs for optical waveguides we developed that can handle the power necessary to trap atoms in a dual color trap similar to the nanofiber. The goal was to design a waveguide on a chip that has similar capabilities as an optical fiber but can improve upon its drawbacks such as polarization rotation due to birefringence. The fundamental modes in a rectangular waveguide are either TE or TM. In contrast to the nanofiber, these modes have a well defined transverse polarization. Another feature that makes the nanofiber successful is the ability to overlap a dense cold cloud of atoms from the MOT and use as a source for trapping atoms. Therefore, large open areas around the waveguide for the formation of the MOT cloud are essential. However, the large open areas reduce material that can help dissipate energy from the coupled light leading to damaged or broken waveguides.

6.1 Design

The design of the waveguide was centered around several important characteristics. First, the waveguide trap requires a source of atoms. The MOT provides a dense source and was successfully implemented with the nanofiber trap. Therefore, the chip was designed with a large open area that allows the laser beams required for a MOT to transmit through as shown in Figure (6.1)(a). The cooling beams are shown in red and transmit through the cutouts on the chip. Second, due to the large

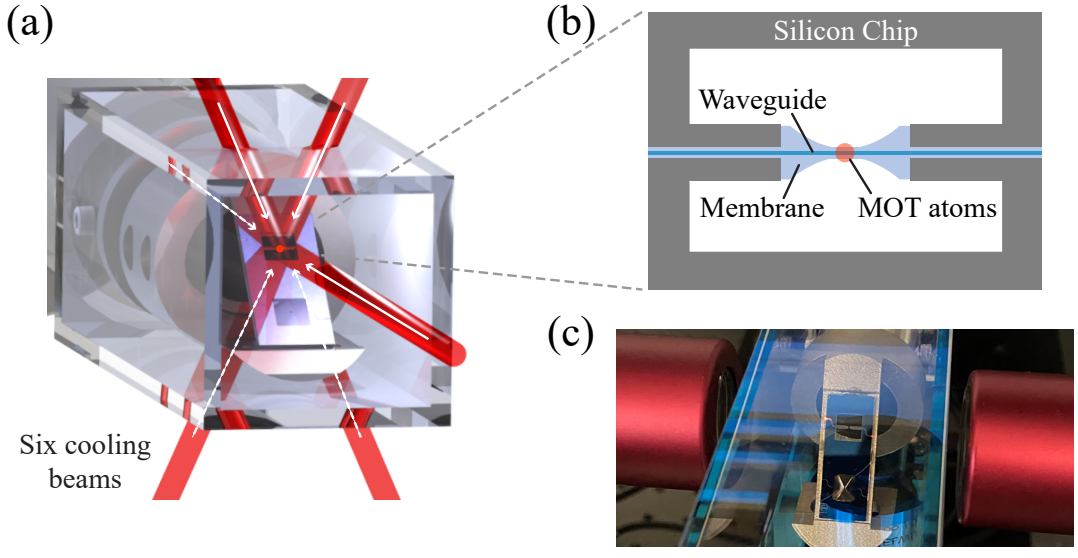

Figure 6.1: (a) Conceptual image of the waveguide chip and the cooling beams used to form a MOT atom cloud.(b) The chip cutout allows for the formation of the cloud around the waveguide. (c) An image of the chip installed in a glass together with the high numerical aperture objectives used to couple light into the waveguide.

opening, a thermal sink is required to overcome excessive heating of the waveguides. This heating is due to impurities in the material or contaminants on the surface that scatter the guided light. Therefore, a thin membrane is connected to the waveguide to help dissipate heat. An example of the membrane is shown conceptually in Figure (6.1)(b). Other designs are discussed in the next section.

Third, a method of coupling light into the waveguide is required. Although there

are several ways to couple light into the waveguide such as grating couplers or vertical tapers, we opted for a free space coupling scheme using high numerical aperture (NA = 0.4) objectives. Figure (6.1)(c) shows an image of an experimental realization of this approach.

Fourth, the waveguide transmission can degrade due to coating of alkali atoms once it is suspended in the atomic vapor. Aluminum oxide (Al_2O_3) has been used to protect the underlying waveguide structure against degradation due to alkali atom deposition [87]. We take this a step further and fabricate the waveguide itself from Al_2O_3.

Finally, the design should incorporate the aforementioned constraints while simultaneously producing an evanescent field that can be used to trap atoms similarly to the nanofiber platform. The optical rib waveguide [88] combines a large thin substrate with a waveguide of the same material as shown in Figure (6.2)(a). Furthermore, the membrane thickness can be chosen to optimally transmit incident light. Figure (6.2)(b) shows the evanescent field trap potential. For this calculation, we consider two fields with wavelengths 937 nm and 793 nm with a total power of 6 mW realizing a maximum trap depth of 350 μK.

6.2 Fabrication

The waveguide chip dimensions are 12.3 mm $\times$ 13 mm and the square cutout at the center has dimensions of 5.4 mm $\times$ 5.4 mm. I will sometimes refer to the cutout as the cooling beam window. All designs are based on aluminum oxide membranes and waveguides on a silicon substrate. We explore two primary designs: the "infinity design" and the "hybrid needle design." Both designs are shown in Figure (6.3). The "infinity design" features a continuous membrane which extends across the large cooling beam window. At the center of the cooling beam window, two circular

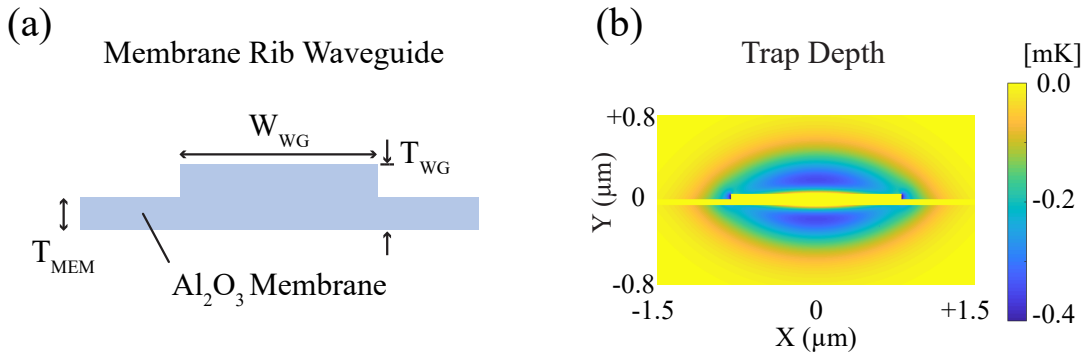

Figure 6.2: (a) The membrane rib waveguide has height T_{WG} with a membrane width of T_{MEM}. The width of the waveguide is given by W_{WG}. (b) The calculated trapping potential and field pattern around the rib waveguide using two fields with wavelengths 937 nm (2.73 mW) and 793 nm (3.27 mW). The maximum trap depth is 350 μK. The waveguide parameters for this calculation are $W_{WG} = 1.6\ \mu m$, T_{WG} = 200 nm, and T_{MEM} = 50 nm.

openings are formed in the membrane on opposite sides of the waveguide. The "needle" structure minimizes the extent of the membrane to be near the waveguide only. The underlying silicon structure extends into the cutout region in the form of "needles" as shown in Figure (6.3)(b). The thickness of the alumina membrane

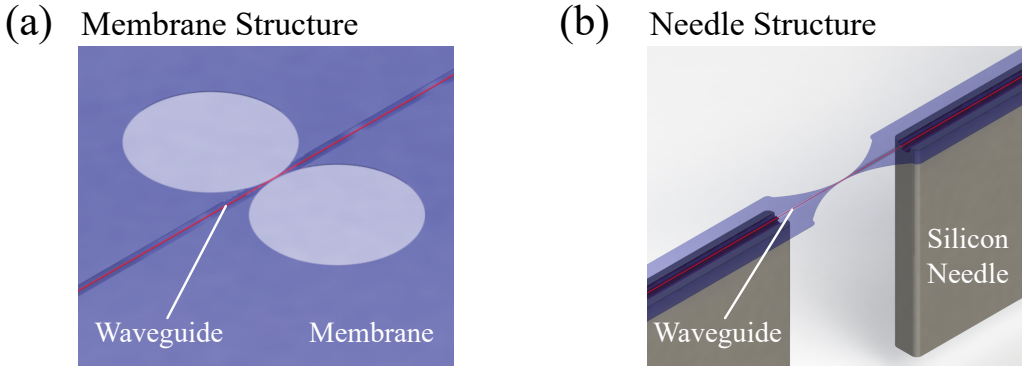

Figure 6.3: (a) The infinity design consists of two circles cutout on each side of the waveguide.(b) The needle structure consists of silicon needle structures that extend into the chip cutout to support the membrane.

is important as it can have drastic effects on the transmission of the MOT laser beams. Considering an alumina membrane surrounded by vacuum, a thickness near 265 nm produces an anti-reflection minima leading to >98% transmission for the 852 nm cooling beams. Unfortunately, this thickness is not optimal for the evanescent optical trap and thinner membranes are required. Therefore, we experimentally investigated the transmission properties for thinner membrane thickness of 25, 50 and 75 nm, leading to, 96.2%, 88.0% and 80.3% transmission, respectively for the circularly polarized 852 nm beams. Although not quite optimal, a high degree of transmission is still attained.

The process of fabricating the chip is shown in Figure (6.4). First, aluminum oxide is deposited on a silicon wafer via atomic layer deposition (ALD). The front side is patterned by conventional photolithography with photoresist (no hard mask). The films are then etched by inductively-coupled plasma reactive-ion etching (ICP-RIE) to define the waveguide and membrane geometries. To form the cooling beam window, the silicon wafer is etched using a deep-reactive ion etch (DRIE) Bosch process, stopping short of the alumina membrane by a few tens of microns. A final XeF2 etch is used to completely open these windows. At the same time, in regions outside of the large cooling beam windows, small membrane openings along the length of the waveguide allow local undercutting of the waveguide.

6.3 Thermal Properties and Power Handling Capabilities

The temperature distribution when coupling 10 mW of power into the waveguides was simulated using COMSOL. The simulated temperature distributions for both the infinity and needle structure designs are shown in Figure (6.5). The thermal conductivity for the aluminum oxide membrane is dependent on the thickness of the

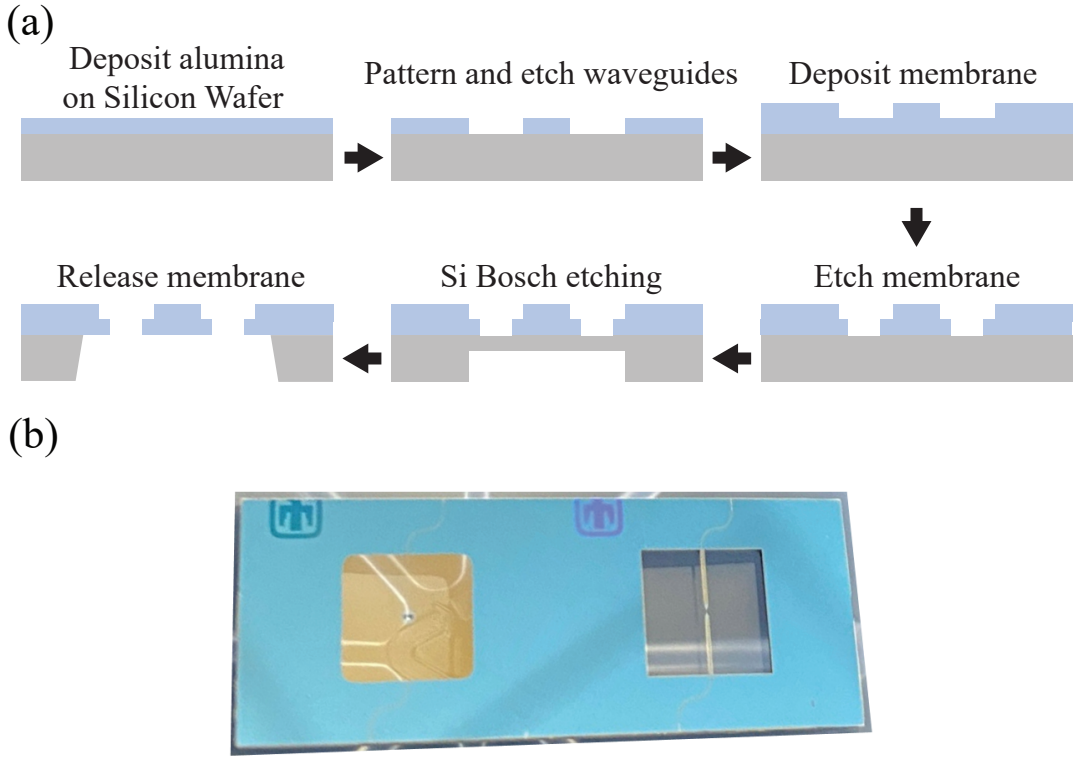

Figure 6.4: (a) The fabrication process for the chip includes depositing alumina onto a silicon wafer. The waveguides are patterned an etched using photolithography and photoresist. The membrane is released leaving no silicon behind the membrane. (b) An fabricated chip with the infinity and needle designs.

deposited layer and the substrate its deposited on [89]. A conservative value of 1 $Wm^{-1}K^{-1}$ was used for the simulations. The peak temperature is located near the opening of the membrane due to having less material to dissipate the thermal energy. The peak temperatures are 1200 °C and 1400 °C for the infinity and hybrid needle designs, respectively. These temperatures are below the melting point of aluminum oxide, 2072 °C. Several smaller waveguides were made to test their power-handling capabilities. For this test, laser light is coupled into the waveguide using lensed fibers and its power is increased until the waveguide fails (brake or become damaged). A 937 nm external cavity diode laser (ECDL) with a tapered amplifier providing several hundreds of milliwatts of optical power (Figure (6.6)) is used as the source. The fiber-

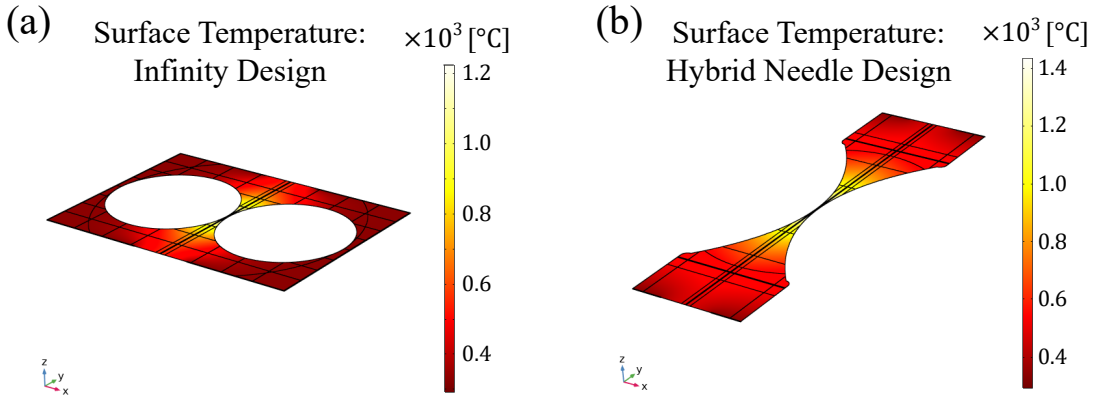

Figure 6.5: Simulation of the temperature distribution of the membrane with the (a) infinity design and (b) needle structure design, when 10 mW is coupled into the waveguide.

coupled light passes through a fiber paddle to adjust the polarization to optimize the coupling into the waveguide. After this, the input power, P_{IN}, was monitored by using a fiber splitter to split it into two paths, one with a 80% transmission and the other with 20% transmission. The path with 20% transmission is directed to a photodiode and used as a reference monitor. The other path is coupled into the waveguide using a lensed fiber. The transmitted light through the waveguide under test was collected with another lensed fiber at the output and monitored by a second photodiode (P_{OUT}). By assuming equal fiber to waveguide coupling on both sides of the device, we can estimate the power at the waveguide as $P_{WG} = \sqrt{P_{IN}P_{OUT}}$. We tested several devices and observed a consistent transmission of $\approx 20\%$, which gives confidence in this assumption. Figure (6.7) shows the output power measured as a function the input power for the hybrid needle design. The several abrupt jumps in the data occur due to thermalization of the waveguide which reduced the coupling efficiency and had to be readjusted during the measurement. The blue trace is the transmitted power out of the waveguide and the red trace is the estimated power at the center of the waveguide. The sudden drop of power at around $P_{in} = 45$ mW is

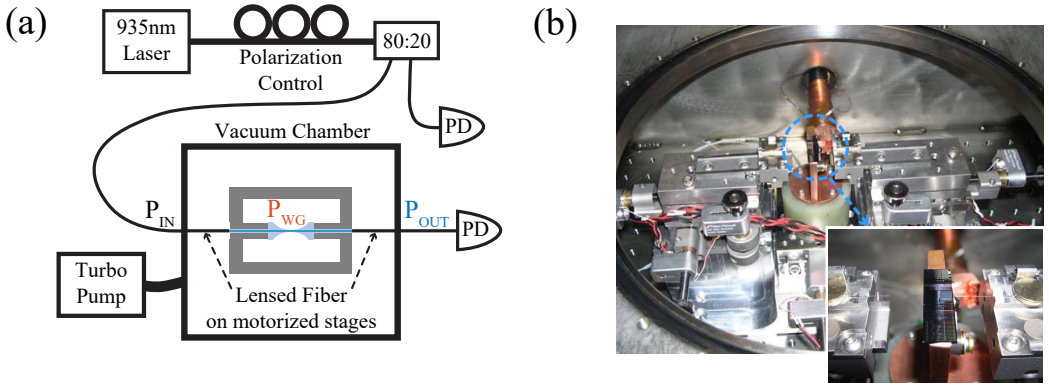

Figure 6.6: (a) Diagram displaying the experimental setup used to measure the maximum power handled by the waveguide. (b) Image of the vacuum chamber housing the chip to reduce the ambient pressure to roughly 10^{-6} Torr.

due to the waveguide breaking under the large thermal load. The power, P_{WG}, is recorded as the maximum power-handling capability for the waveguide under test.

6.4 Atom Cloud and Waveguide Overlap

As mentioned previously, each waveguide is designed with a 5.4 mm $\times$ 5.4 mm window. The MOT cooling beams transmit through these openings. The cooling beams are angled with respect to the opening in the waveguide and therefore the effective area will not be 5.4 mm $\times$ 5.4 mm. For instance, if the beams are 45 degrees from a vector normal to the surface, the effective area is $A_{\text{eff}} = A/\sqrt{2}$. Here, A is the area at normal incidence and equal to 5.4 mm $\times$ 5.4 mm without a needle structure. In addition, the needle structure reflects the cooling beams reducing the effective area further. Figure (6.9) shows a calculation taking into account the needle structure area. At zero degrees (normal incidence) the area is maximized. Increasing the tilt angle reduces the area and is minimal at a tilt angle of 72.3 degrees. The MOT cooling beam's diameter of 4 mm was chosen in order to maximize its size while

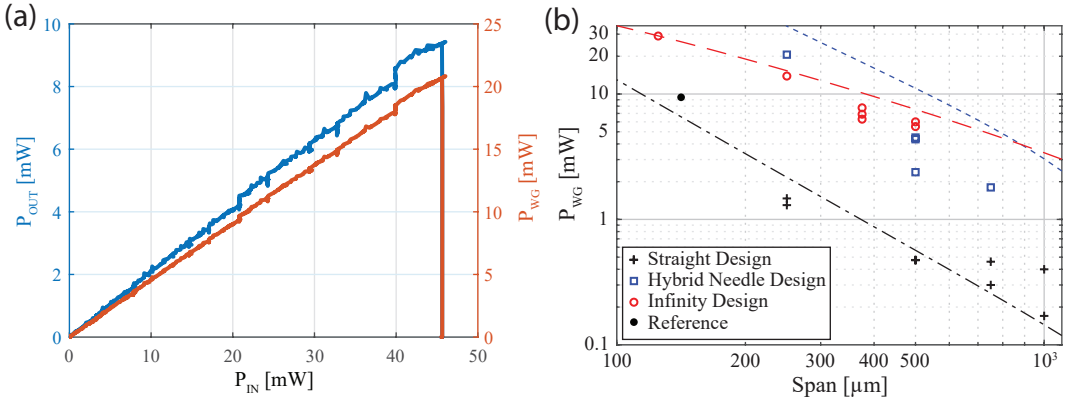

Figure 6.7: (a) An example of the data from the power-handling measurement for the "hybrid needle design". The red trace is the input power of the laser light coupled into the waveguide. The blue trace is the power measured out of the waveguide. (b) The optimal power before failure is compared for different waveguide designs and spans. The span is defined in Figure (6.8).

being small enough to transmit through the chip's opening without much scatter from the opening's edges.

To align the MOT cloud with the waveguide, we used two CCD cameras to view the atom cloud from two points of view. While observing its position, we moved the cell with the chip using x, y, and z translation stages similar to the nanofiber setup. For fine adjustment, the current of the bias magnetic field coils in the x, y, and z directions were manually tuned to change the MOT cloud position. Even with the loss of scattering due to the silicon needles, we are still able to see an atom cloud at the waveguide which is verified by using several viewing angles. In Figure (6.10), we show CCD images after aligning the MOT cloud with the waveguide.

We tried two methods to measure the number of atoms in the MOT cloud while inside the waveguide cutout but away from the waveguide. First, we used an absorption probe. The beam had a $1/e^2$ diameter of 1 mm and a wavelength of 895 nm. It was locked to the $F = 4 \rightarrow F' = 4$ D1 transition. Using an 895 nm wavelength helps to distinguish between the light scatter from the cooling beams and the probe

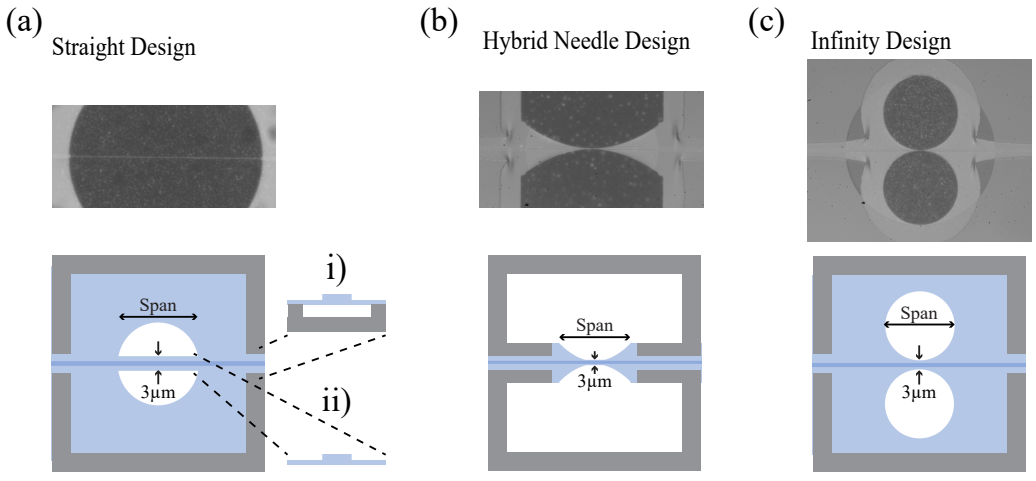

Figure 6.8: Test structures were fabricated for the power-handling measurement. (a) is the straight design, (b) is the needle design, and (c) is the infinity design. The top row are fabricated devices and the bottom row are conceptual drawings.

beam by spectral filtering. The probe was directed toward the MOT cloud and the output was fiber coupled and sent to an APD. Due to the small absorption signal, we used a modulation technique that is similar to lock-in detection. For this technique, we modulated the current to the MOT quadrupole field at 1 Hz. This allowed enough time for the MOT to load. The 895 nm light was kept constantly on and its transmission measured. The Fourier transform of the signal had a signature of the modulation and its amplitude was compared to that of the steady state signal. Using the equation

$$N = A\frac{\pi\omega_0^2}{2\sigma_0^2} \tag{6.1}$$

where N is the number of atoms, A is the probe absorption, ω_0 is the waist of the laser beam, and σ_0 is the resonant absorption cross section. In principle, this technique should distinguish between the small MOT absorption signal and the background. We were not successful in using this technique to measure the number of MOT atoms while it was overlapped with the waveguide. It is likely due to the low atom number in the MOT cloud.

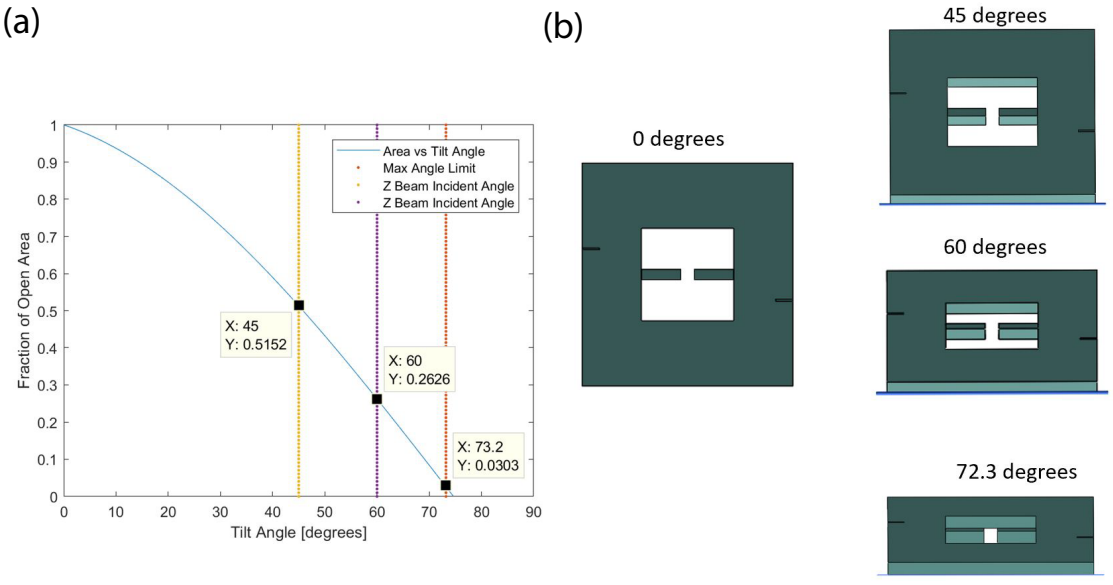

Figure 6.9: The cooling beams are directed through the chip cutout and, due to the angle of the chip, experience a reduced effective area to go through. The effective area is an important parameter in choosing the diameter of the cooling beams as excess scatter can cause a reduced atom number in the MOT and reduce visibility when using a CCD camera to view the MOT cloud.

Because we were able to see the MOT using a CCD camera, we used the camera to estimate the number of atoms. To do this, we calibrated the camera by directing a laser beam to the sensor with a known power and summed the all the pixel values. Using this calibration value, we estimated about an order of magnitude less atoms in the MOT when overlapped with the waveguide. The lower atom number can be attributed to two effects. As the cold atoms in the MOT get closer to the hot surface, they collide and gain enough energy to escape the trap. In addition, as we move the cell to overlap the MOT and waveguide the cooling beams are partially blocked by the needle structure reducing their intensity and consequently the number of atom scattering events which is needed to trap the atoms.

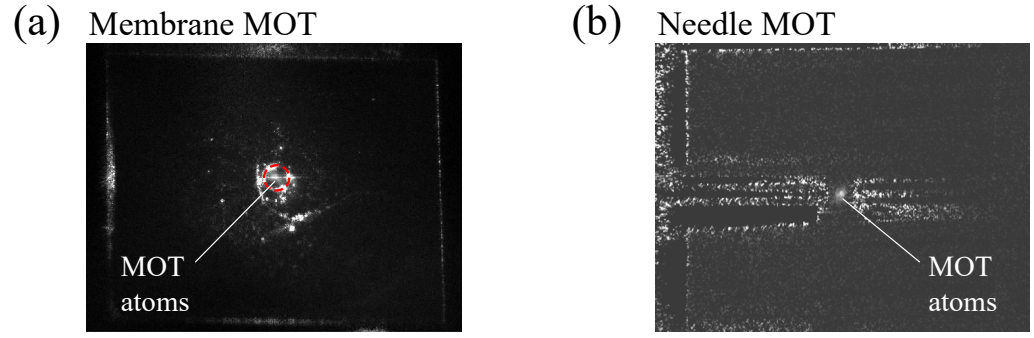

Figure 6.10: (a) The MOT cloud is centered in a hole in the membrane. (b) The MOT cloud is centered in between the two needle structures.

6.5 Waveguide Degradation

During several of the experiments, we coupled light into the waveguides in an effort to perform absorption measurements of the MOT cloud around the waveguide. During this process, we observed a loss of transmission that could be due to alkali atom deposition but we weren't able to confirm this hypothesis. On other devices we experienced a sudden breakage of the waveguide while coupling light that is most likely due to local heating due to impurities or imperfections in the material but could also be due to dust or other contaminants landing on the waveguide during installation.

6.6 Vacuum System with Loading Chamber

Each chip was installed in a separate vacuum chamber, baked, and coated with cesium which took several weeks to accomplish. In order to shorten this time, a larger more complex vacuum chamber was designed. A diagram of this system is shown in Figure (6.11). The load lock section is separated from the experiment section by a ultra-high vacuum compatible gate valve. During chip replacements,

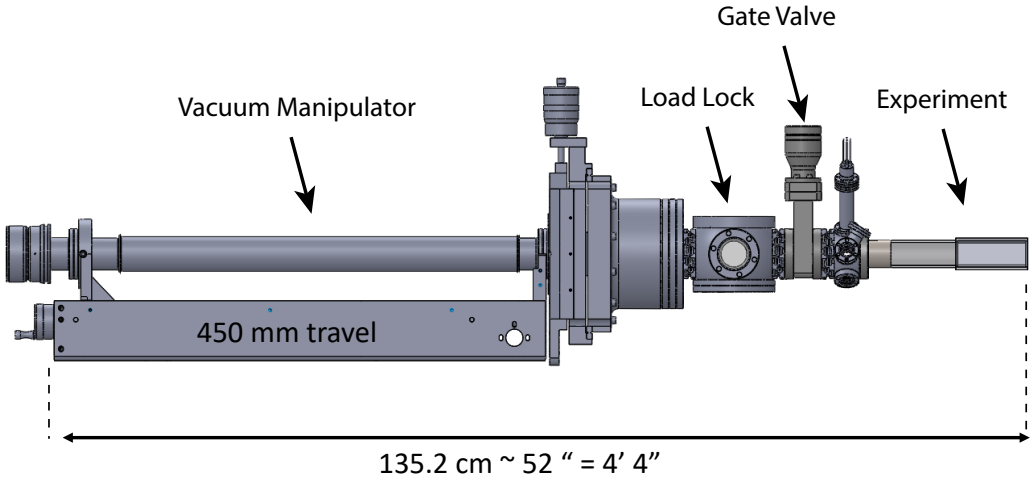

Figure 6.11: The vacuum package includes a load lock section separated from the experiment using a gate valve. This system will allow more efficient unloading/reloading of waveguide chips and reduce vacuum preparation time.

the arm of the vacuum manipulator (VACGEN) is retracted and the gate valve is closed leaving the experiment section under high vacuum. The benefit being that this part of the chamber doesn't have to be baked at high temperature after the initial bake. This process takes up to a week to reach ultra-high vacuum pressures of around 10^{-9} Torr. Also to prepare the vacuum cell for experiments with the cesium atomic vapor, a coating process where cesium is deposited on the inner walls of the vacuum system is also required. This process can take several weeks. After closing the gate valve, this section remains coated with cesium atoms as it no longer is required to be baked. This system is still under construction.

Chapter 7

Conclusion and Outlook

In thesis, I have described the construction of a pulling rig to fabricate optical nanofibers. In addition, we have realized a nanofiber based atom trap for Cesium atoms and characterized their coherence using microwave fields. The nanofiber pulling rig was built with the capability of designing nanofibers with applications to atom interferometry such as a variable waist, or nanofiber section, that would otherwise limit the interferometers sensitivity. The pulling rig was also shown to produce nanofibers with predetermined radii in a reliable way.

I have also discussed theoretical work describing the interactions of nanofiber trapped atoms with Raman beams guided in the nanofiber. These interactions resulted in non-trivial dynamics due to the spatial gradient of the evanescent field. The spatial intensity gradient couples the internal and external, i.e., trap states, of the atoms. Nevertheless, parameters were given such that the efficiency of transfer resembles the free atom case and makes driving Raman transitions possible.

Although efforts are still underway in realizing an atom interferometer with nanofiber trapped atoms, this thesis provides invaluable analysis toward the realization of such a device. Some enhancements of our device that would be helpful in this endeavor is an increase in trap lifetime. This can be achieved by implementing

cooling methods such as degenerate Raman cooling [30] or Raman sideband cooling [29].

Appendices

Appendix A

Raman Transition

In this appendix, I derive the Hamiltonian for a three-level atom interacting with an electromagnetic field. These derivations supplement the equations presented in Chapter 3.

A.1 Raman Interaction Hamiltonian

The system consists of three levels: two ground states $|g_1\rangle$ and $|g_2\rangle$, and one intermediate state $|e\rangle$. We assume there is no coupling between $|g_1\rangle$ and $|g_2\rangle$. The atom interacts with two electric fields $\vec{E}_1$ coupling $|g\rangle_1 \rightarrow |e\rangle$ and $\vec{E}_2$ coupling $|g\rangle_2 \rightarrow |e\rangle$. In the dipole approximation, the Hamiltonian is

$$\hat{H} = \hat{H}_{\text{atom}} + \hat{H}_{\text{mot}} + \hat{H}_{\text{int}} \tag{A.1}$$

where

$$\begin{aligned} \hat{H}_{atom} &= \hbar\omega_e |e\rangle\langle e| + \hbar\omega_{g_2} |g_2\rangle\langle g_2| \\ \hat{H}_{mot} &= \frac{\hat{p}^2}{2m} \\ \hat{H}_{int} &= -\hat{d} \cdot \vec{E}(z,t) \end{aligned} \tag{A.2}$$

The reference energy is taken to be zero at $|g_1\rangle$ and $\vec{E}(z,t) = \sum_{j=1}^{2} E_j \vec{\epsilon}_j \cos(\omega_j t + \phi_j - k_j z)$ is the total field. This interaction can be decomposed into its matrix representation by making use of the resolution of the identity $\hat{I} = \sum_n |n\rangle\langle n|$

$$\begin{aligned} \hat{d}\cdot\vec{\epsilon}_j &= \sum_{m=1}^{3}\sum_{n=1}^{3} \langle m|\, \hat{d}\cdot\vec{\epsilon}_j\, |n\rangle\, |m\rangle\, \langle n| \\ &= d^{(j)}_{g_1,e}\, |g_1\rangle\langle e| + d^{(j)}_{g_2,e}\, |g_2\rangle\langle e| + H.c \end{aligned} \tag{A.3}$$

where $d^{(j)}_{m,n} = \langle m|\, \hat{d}\cdot\vec{\epsilon}_j\, |n\rangle\, |m\rangle\, \langle n|$ and $h.c$ is the hermitian conjugate of the total expression to the left. The sum is over the basis states of the Hilbert space. Inserting equation A.3 into the expression for $\hat{H}_{\text{int}}$

$$\begin{aligned} \hat{H}_{\text{int}} &= \sum_{j=1}^{2} \left(-d^{(j)}_{g_1,e}E_j\, |g_1\rangle\langle e| - d^{(j)}_{g_2,e}E_j\, |g_2\rangle\langle e| + H.c\right)\cos(\omega_j t + \phi_j - k_j z) \\ &= \sum_{j=1}^{2} \left(-\frac{d^{(j)}_{g_1,e}E_j}{2}\, |g_1\rangle\langle e| - \frac{d^{(j)}_{g_2,e}E_j}{2}\, |g_2\rangle\langle e| + H.c\right)\left(e^{i(\omega_j t+\phi_j-k_j z)} + c.c.\right) \\ &= \sum_{j=1}^{2} \left(\hbar\Omega^{(j)}_{g_1,e}\, |g_1\rangle\langle e| + \hbar\Omega^{(j)}_{g_2,e}\, |g_2\rangle\langle e| + H.c\right)\left(e^{i(\omega_j t+\phi_j-k_j z)} + c.c.\right) \end{aligned} \tag{A.4}$$

where $|1\rangle \to |g_1\rangle$,$|2\rangle \to |g_2\rangle$,and $|3\rangle \to |e\rangle$ was used and $\hbar\Omega^{(j)}_{m,n} = -\frac{d^{(j)}_{m,n}E_j}{2}$. The above assumes cross couplings that are off resonant. Considering these contributions to be small, we can keep terms for each field $E_j(z,t)$ that couples $|g_j\rangle \to |e\rangle$ only.

$$H_{int} = \sum_{j=1}^{2} \left(\hbar\Omega^{(j)}_{g_j,e}\, |g_j\rangle\langle e| + h.c\right)\left(e^{i(\omega_j t+\phi_j-k_j z)} + e^{-i(\omega_j t+\phi_j-k_j z)}\right) \tag{A.5}$$

A.2 Rotating Frame Hamiltonian

Jumping into a rotating frame, we can separate the fast and slow dynamics. The rotating frame Hamiltonian $\hat{H}_{rot}$ is defined as

$$H^{rot} = U^\dagger H U + i\hbar\frac{\partial U^\dagger}{\partial t}U \tag{A.6}$$

where U is the rotation operator. The derivation of this equation is typically performed starting from the Schrödinger equation and defining $|\psi\rangle^{(rot)} = U|\psi\rangle$. The rotation operator for multiple level atoms can be written as

$$U = \sum_{l=1}^{3} e^{-i\lambda_l t} |l\rangle\langle l|$$

where $|l\rangle$ refers to all states in the system, $|g_1\rangle$, $|g_2\rangle$, $|e\rangle$. The exponents include a parameter λ_l that is yet to be determined. Another way to write this operator is as a product of three unitary operators. Using the Taylor expansion definition of a function of matrices and the states orthogonality,

$$\sum_{l=1}^{3} e^{-i\lambda_l t} |l\rangle\langle l| = \exp\left(\sum_{l=1}^{3} -i\lambda_l t |l\rangle\langle l|\right) = \prod_{\mathrm{l}=1}^{3} \exp\left(-i\lambda_l t |l\rangle\langle l|\right)$$

Using either definition above, we can apply the operator to the different terms in equation A.6 to evaluate the different terms so that

$$H^{rot} = H_{atom} + H_{mot} + U^\dagger H_{int} U + i\hbar \frac{\partial U^\dagger}{\partial t} U \tag{A.7}$$

The interaction term $\hat{H}_{int}$ consists of off diagonal elements due to the parity of the dipole operator. To evaluate these terms we use the result that $U^\dagger |g_j\rangle\langle e| U = e^{i(\lambda_{g_j} - \lambda_e)t} |g_j\rangle\langle e|$. Choosing $\lambda_e = \omega_1$, $\lambda_{g_2} = \omega_1 - \omega_2$ (where ω_1 and ω_2 are the two laser frequencies) we have

$$\begin{aligned} H_{int}^{rot} &= U^\dagger H_{int} U \\ &= \sum_{j=1}^{2} \hbar \Omega_{g_j,e}^{(j)} |g_j\rangle\langle e| \left(e^{i(\phi_j - k_j z)} + e^{-i(2\omega_j t + \phi_j - k_j z)}\right) + H.c \end{aligned} \tag{A.8}$$

Using the rotating wave approximation, we ignore fast rotating terms (terms with $2\omega_j$) to arrive at the result

$$H_{int}^{rot} = \sum_{j=1}^{2} \left(\hbar \Omega_{g_j,e}^{(j)} |g_j\rangle\langle e| e^{i(\phi_j - k_j z)} + H.c\right) \tag{A.9}$$

This Hamiltonian is just two two-level systems with a common excited state $|e\rangle$. The last term in the interaction picture transformation is

$$i\hbar\frac{\partial U^\dagger}{\partial t}U = -\hbar\omega_1 |e\rangle\langle e| - \hbar(\omega_1 - \omega_2) |g_2\rangle\langle g_2|$$

which leads to

$$H^{rot} = \frac{p^2}{2m} - \hbar\Delta |e\rangle\langle e| - \hbar\delta |g_2\rangle\langle g_2| + \sum_{j=1}^{2}\left(\hbar\Omega^{(j)}_{g_j,e} |g_j\rangle\langle e| e^{i(\phi_j - k_j z)} + H.c\right) \quad \text{(A.10)}$$

where $\Delta = \omega_1 - \omega_e$ is the single photon detuning and $\delta = (\omega_1 - \omega_2) - \omega_{g_2}$ is the two photon detuning.

A.3 Rabi Frequency

A guided field in the nanofiber has an evanescent tail that decays away from the surface of the fiber. This spatial gradient couples motional and internal atomic states. Here, a derivation of the Rabi frequency or coupling strength of these transitions is presented. This work closely follows [90]. The coupling strength is given by

$$\begin{aligned}\Omega_{n,n'} &= \Omega_0 |\langle n'| e^{-\Gamma x} |n\rangle| \\ &= \Omega_0 |\langle n'| e^{-\eta(a^\dagger + a)} |n\rangle|\end{aligned} \quad \text{(A.11)}$$

where $\Omega_0 = -\langle g|\hat{\vec{d}}\cdot\vec{E}|e\rangle/\hbar$ is the Rabi frequency between internal states $|g\rangle$ and $|e\rangle$, and the definition $\hat{x} = x_0(\hat{a} + \hat{a}^\dagger)$ where $x_0 = \sqrt{\hbar/2m\omega_T}$ was used. The annihilation $\hat{a}$ and creation operators $\hat{a}^\dagger$ have the following commutation relation $[a^\dagger, a] = -1$. To evaluate the action of the exponential operator on the motional states, the following identity is used

$$e^{A+B} = e^A e^B e^{-[A,B]/2} \quad \text{(A.12)}$$

which is valid if $[A,[A,B]] = [B,[A,B]] = 0$. Using this identity, the exponential operator can be written as

$$\langle n'| e^{-\eta(a^\dagger + a)} |n\rangle = e^{\eta^2/2} \langle n'| e^{-\eta a^\dagger} e^{-\eta a} |n\rangle \quad \text{(A.13)}$$

Now we can evaluate the action of $e^{-\eta a}\left|n\right\rangle$ by using the Taylor expansion definition of the exponential function $e^x = \sum_l x^l/l!$. The action of the annihilation operator on a Fock state applied m times is [90]

$$a^m\left|n\right\rangle = \begin{cases} (n!/(n-m)!)^{1/2}\left|n-m\right\rangle & ,m \leq n \\ 0 & ,m > n \end{cases} \tag{A.14}$$

then

$$e^{-\eta a}\left|n\right\rangle = \sum_{l=0}^{\infty} \frac{(-\eta)^l}{l!}\left(\frac{n!}{(n-m)!}\right)^{1/2}\left|n-m\right\rangle \tag{A.15}$$

Using the above in equation (A.13), we obtain

$$\begin{aligned} e^{\eta^2/2}\left\langle n'\right| e^{-\eta a^\dagger} e^{-\eta a}\left|n\right\rangle = e^{\eta^2/2}\sqrt{\frac{n_<!}{n_>!}}(-\eta)^{\Delta n} \\ \times \sum_{m=0}^{n_<} \frac{(n_< + \Delta m)!(-\eta)^{2m}}{m!(m+\Delta n)!(n_< - m)!} \end{aligned} \tag{A.16}$$

where $\Delta n = |n' - n|$ and $n_<(n_>)$ is the lesser(greater) of n and n'. Using the definition of the generalized Laguerre polynomial,

$$L_n^\alpha[X] = \sum_{m=0}^{n}(-1)^m\binom{n+\alpha}{n-m}\frac{X^m}{m!} \tag{A.17}$$

the final expression can be written as

$$\left\langle n'\right| e^{-\Gamma x}\left|n\right\rangle = e^{\eta^2/2}\sqrt{\frac{n_<!}{n_>!}}(-\eta)^{\Delta n} L_{n_<}^{\Delta n}[-\eta^2] \tag{A.18}$$

The Rabi frequency is then given by

$$\Omega_{n',n} = \Omega_0\left|e^{\eta^2/2}\sqrt{\frac{n_<!}{n_>!}}(-\eta)^{\Delta n} L_{n_<}^{\Delta n}[-\eta^2]\right| \tag{A.19}$$

Appendix B

HE_{11} Polarization

In atom interferometry and many atomic physics experiments, the polarization of the field is used to excite specific transitions. The field's polarization corresponds to its spin angular momentum and angular momentum conservation during the atom-light interaction limits which transitions are possible as summarized in the dipole selection rules [46]. Not having a good understanding of the polarization can be detrimental in an experiment because unwanted excitations can reduce the desired signal by distributing population into other undesired levels. The HE_{11} mode exhibits a polarization component along the propagation direction of the field which can lead to the aforementioned effects if not properly taken into account. The polarization orientation with respect to the quantization axis is the important parameter to consider giving rise to $\sigma_0,\ \sigma_-,$ or σ_+ transitions [46]. The quantization axis can be established in the $\vec{e}_n$ direction by applying an external static magnetic field $\vec{B} = B\vec{e}_n$, where B is the magnitude of the field. An intuitive way to look at the field polarization is to break it up into the spherical basis components which are defined with respect to a quantization axis [91]. Here I consider the coordinate system as defined in Figure (2.1). The relationship between the Cartesian basis and the spherical basis with the

quantization axis along $\vec{e}_z$ is

$$\begin{aligned}\vec{e}_+ &= -\frac{\vec{e}_x + i\vec{e}_y}{\sqrt{2}} \\ \vec{e}_- &= \frac{\vec{e}_x - i\vec{e}_y}{\sqrt{2}} \\ \vec{e}_0 &= \vec{e}_z\end{aligned} \tag{B.1}$$

The components $\vec{e}_+$, $\vec{e}_-$, and $\vec{e}_0$ describe the part of the field that is σ_+, σ_-, or σ_0 polarized, respectively. These components constitute a complete orthogonal basis with orthogonality defined by $\vec{e}_q \cdot \vec{e}^*_{q'} = 0$ if $q \neq q'$ and $\vec{e}_q \cdot \vec{e}^*_q = 1$. Thus the total electric field vector can be decomposed in terms of the spherical basis which is defined as [92]

$$\vec{E} = E_+\vec{e}^*_+ + E_-\vec{e}^*_- + E_0\vec{e}^*_0 \tag{B.2}$$

were $\vec{e}^*_q = (-1)^q\vec{e}_{-q}$ and the components are

$$\begin{aligned}E_+ &= -\frac{(E_x + iE_y)}{\sqrt{2}} \\ E_- &= \frac{E_x - iE_y}{\sqrt{2}} \\ E_0 &= E_z\end{aligned} \tag{B.3}$$

Consider a field traveling in the $+z$ direction that is quasipolarized along x. In Figure (B.1)(a) the polarization of the HE_{11} mode in the transverse plane of the fiber is shown with the quantization axis along $\vec{e}_z$. The components are normalized with respect to the magnitude of the total field at $r = a$, specifically $|E_q(r,\phi)|^2/|\vec{E}_{\text{tot}}(r = a,\phi)|^2$ for $q = 0,$ or $\pm$. The leftmost and center plots show that there are equal contributions from the σ_+ and σ_- polarization components of the field along the x axis. There is about a 10% increase in the strength of these components along the y axis. Additionally, the σ_0 component is almost zero at $\phi = \pi/2$ and $\phi = 3\pi/2$ and has a slightly larger value on the x axis.

It is instructive to see how the polarization components change when changing the quantization axis. To look at the effect of changing the quantization axis, we can permute the indices $\{x, y, z\} \rightarrow \{z, x, y\}$ for the quantization axis along y and $\{x, y, z\} \rightarrow \{y, z, x\}$ for the quantization axis along x. The second and third rows of (B.1) display the field's polarization components for the quantization axis along x and y, respectively. We see a different polarization distribution when choosing the quantization axis along y as shown Figure (B.1)(b). The strengths of the different contributions of circular polarization on each side of the fiber now favors σ_- or σ_+ depending on which side of the fiber is viewed. On the right side, σ_+ dominates and the left side σ_- dominates both reaching a maximum of 93% on the x axis on their respective sides. In [60] this effect was used to manipulate the optical pumping to opposite Zeeman states for atoms trapped on opposite sides of the fiber. In addition, by utilizing the difference in circular polarization handedness, atoms on one side of the fiber were cooled and on the opposite side they were heated [30]. Choosing the quantization axis along x, we see that purely linear polarization can dominate at $\phi = \pi/2$ and $\phi = 3\pi/2$ as can be seen in Figure (B.1)(c). This effect has been used to optically pump atoms using an 895 nm laser tuned to the D1 transition in cesium [1]. For completeness, this same calculation has been performed for a left-hand circularly polarized field traveling along the z axis as shown in Figure (B.2).

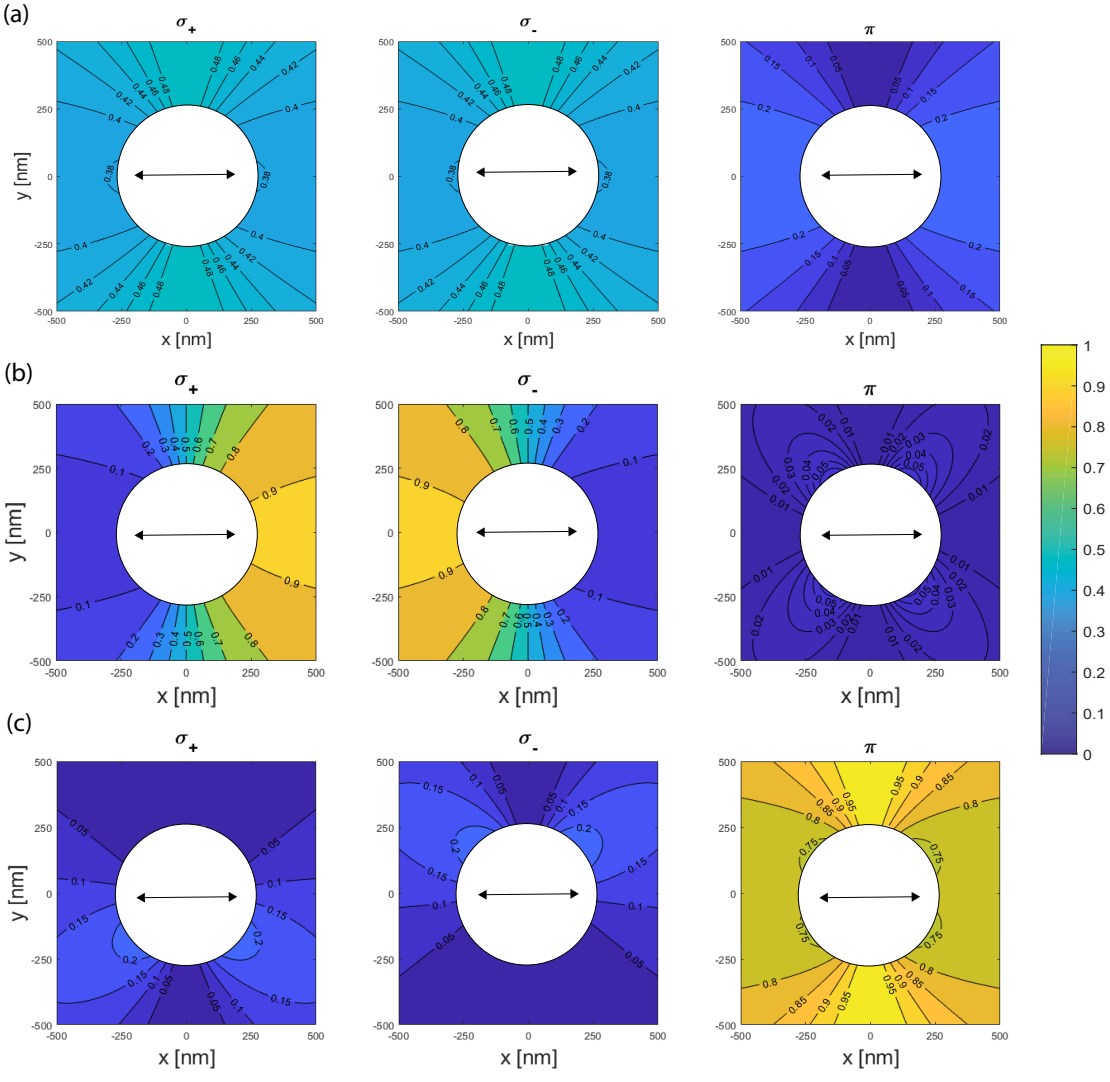

Figure B.1: Polarization distribution in term of the spherical basis (see text) for the HE_{11} fundamental mode traveling along the +z direction for different quantization axes. The quantization axis is along z, y, and x for (a), (b), and (c) respectively. The quasi-polarization of the field is along x as indicated for all the plots.

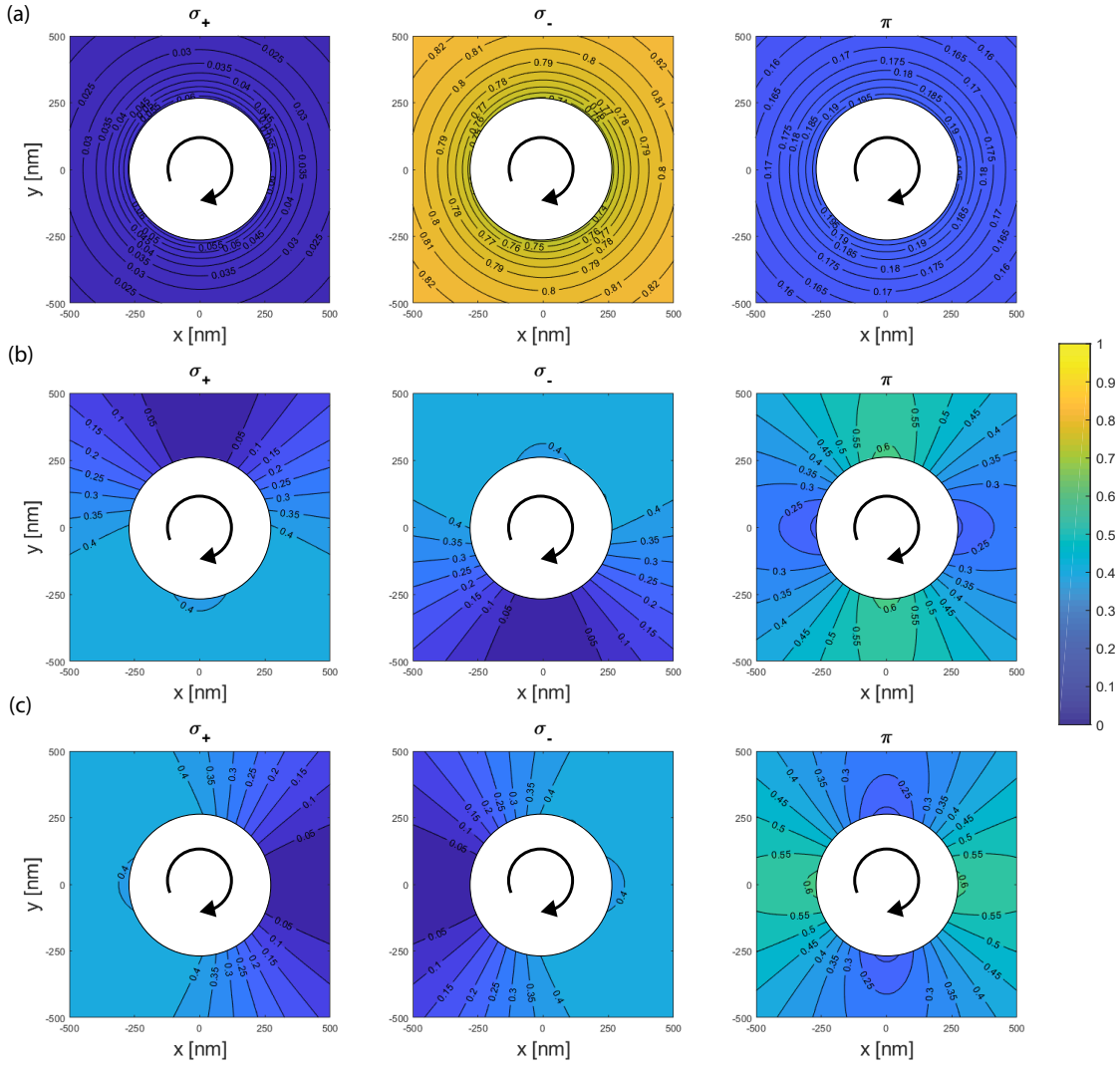

Figure B.2: Polarization distribution in term of the spherical basis (see text) for the HE_{11} fundamental mode traveling along the +z direction for different quantization axes. The quantization axis is along z, y, and x for (a), (b), and (c) respectively. The field is left-hand circularly polarized for all the plots as indicated by the black arrow.

References

[1] Rudolph Mitsch. *Interaction and Manipulation of Nanofiber-Trapped Atoms with Spin-Orbit Coupled Light*. PhD thesis, Vienna University of Technology, 2014.

[2] C. J. Davisson and L. H. Germer. Reflection of Electrons by a Crystal of Nickel. *Proceedings of the National Academy of Sciences*, 14(4):317–322, April 1928.

[3] M. Kasevich and S. Chu. Measurement of the gravitational acceleration of an atom with a light-pulse atom interferometer. *Applied Physics B Photophysics and Laser Chemistry*, 54(5):321–332, May 1992.

[4] Q. Bodart, S. Merlet, N. Malossi, F. Pereira Dos Santos, P. Bouyer, and A. Landragin. A cold atom pyramidal gravimeter with a single laser beam. *Applied Physics Letters*, 96(13):134101, March 2010.

[5] Xuejian Wu, Zachary Pagel, Bola S. Malek, Timothy H. Nguyen, Fei Zi, Daniel S. Scheirer, and Holger Müller. Gravity surveys using a mobile atom interferometer. *Science Advances*, 5(9):eaax0800, September 2019.

[6] J. M. McGuirk, G. T. Foster, J. B. Fixler, M. J. Snadden, and M. A. Kasevich. Sensitive absolute-gravity gradiometry using atom interferometry. *Physical Review A*, 65(3):033608, February 2002.

[7] G. W. Biedermann, X. Wu, L. Deslauriers, S. Roy, C. Mahadeswaraswamy, and M. A. Kasevich. Testing gravity with cold-atom interferometers. *Physical Review A*, 91(3):033629, March 2015.

[8] B. Canuel, F. Leduc, D. Holleville, A. Gauguet, J. Fils, A. Virdis, A. Clairon, N. Dimarcq, Ch. J. Bordé, A. Landragin, and P. Bouyer. Six-Axis Inertial Sensor Using Cold-Atom Interferometry. *Physical Review Letters*, 97(1):010402, July 2006.

[9] David L. Butts, Joseph M. Kinast, Brian P. Timmons, and Richard E. Stoner. Light pulse atom interferometry at short interrogation times. *Journal of the Optical Society of America B*, 28(3):416, March 2011.

[10] Hayden J. McGuinness, Akash V. Rakholia, and Grant W. Biedermann. High data-rate atom interferometer for measuring acceleration. *Applied Physics Letters*, 100(1):011106, January 2012.

[11] Akash V. Rakholia, Hayden J. McGuinness, and Grant W. Biedermann. Dual-Axis High-Data-Rate Atom Interferometer via Cold Ensemble Exchange. *Physical Review Applied*, 2(5):054012, November 2014.

[12] G. W. Biedermann, H. J. McGuinness, A. V. Rakholia, Y.-Y. Jau, D. R. Wheeler, J. D. Sterk, and G. R. Burns. Atom Interferometry in a Warm Vapor. *Physical Review Letters*, 118(16):163601, April 2017.

[13] Vincent Ménoret, Pierre Vermeulen, Nicolas Le Moigne, Sylvain Bonvalot, Philippe Bouyer, Arnaud Landragin, and Bruno Desruelle. Gravity measurements below 10-9 g with a transportable absolute quantum gravimeter. *Scientific Reports*, 8(1):12300, December 2018.

[14] Sheng-wey Chiow and Nan Yu. Compact atom interferometer using single laser. *Applied Physics B*, 124(6):96, June 2018.

[15] Mark Kasevich and Steven Chu. Atomic interferometry using stimulated Raman transitions. *Physical Review Letters*, 67(2):181–184, July 1991.

[16] L. Zhou, Z. Y. Xiong, W. Yang, B. Tang, W. C. Peng, K. Hao, R. B. Li, M. Liu, J. Wang, and M. S. Zhan. Development of an atom gravimeter and status of the 10-meter atom interferometer for precision gravity measurement. *General Relativity and Gravitation*, 43(7):1931–1942, July 2011.

[17] Susannah M. Dickerson, Jason M. Hogan, Alex Sugarbaker, David M. S. Johnson, and Mark A. Kasevich. Multiaxis Inertial Sensing with Long-Time Point Source Atom Interferometry. *Physical Review Letters*, 111(8):083001, August 2013.

[18] Manuel Schilling, Étienne Wodey, Ludger Timmen, Dorothee Tell, Klaus H. Zipfel, Dennis Schlippert, Christian Schubert, Ernst M. Rasel, and Jürgen Müller. Gravity field modelling for the Hannover 10 m atom interferometer. *Journal of Geodesy*, 94(12):122, December 2020.

[19] T. Kovachy, P. Asenbaum, C. Overstreet, C. A. Donnelly, S. M. Dickerson, A. Sugarbaker, J. M. Hogan, and M. A. Kasevich. Quantum superposition at the half-metre scale. *Nature*, 528(7583):530–533, December 2015.

[20] Holger Müller, Sheng-wey Chiow, Quan Long, Sven Herrmann, and Steven Chu. Atom Interferometry with up to 24-Photon-Momentum-Transfer Beam Splitters. *Physical Review Letters*, 100(18):180405, May 2008.

[21] Anne Louchet-Chauvet, Tristan Farah, Quentin Bodart, André Clairon, Arnaud Landragin, Sébastien Merlet, and Franck Pereira Dos Santos. The influence of transverse motion within an atomic gravimeter. *New Journal of Physics*, 13(6):065025, June 2011.

[22] A Peters, K Y Chung, and S Chu. High-precision gravity measurements using atom interferometry. *Metrologia*, 38(1):25–61, February 2001.

[23] F. Riehle, Th. Kisters, A. Witte, J. Helmcke, and Ch. J. Bordé. Optical Ramsey spectroscopy in a rotating frame: Sagnac effect in a matter-wave interferometer. *Physical Review Letters*, 67(2):177–180, July 1991.

[24] Mingjie Xin, Wui Seng Leong, Zilong Chen, and Shau-Yu Lan. An atom interferometer inside a hollow-core photonic crystal fiber. *Science Advances*, 4(1):e1701723, January 2018.

[25] G. D. McDonald, H. Keal, P. A. Altin, J. E. Debs, S. Bennetts, C. C. N. Kuhn, K. S. Hardman, M. T. Johnsson, J. D. Close, and N. P. Robins. Optically guided linear Mach-Zehnder atom interferometer. *Physical Review A*, 87(1):013632, January 2013.

[26] Eugene Vetsch. *Optical Interface Based on a Nanofiber Atom-Trap*. PhD thesis, Johannes Gutenburg University of Mainz, 2010.

[27] E. Vetsch, D. Reitz, G. Sagué, R. Schmidt, S. T. Dawkins, and A. Rauschenbeutel. Optical Interface Created by Laser-Cooled Atoms Trapped in the Evanescent Field Surrounding an Optical Nanofiber. *Physical Review Letters*, 104(20):203603, May 2010.

[28] A. Goban, K. S. Choi, D. J. Alton, D. Ding, C. Lacroûte, M. Pototschnig, T. Thiele, N. P. Stern, and H. J. Kimble. Demonstration of a State-Insensitive, Compensated Nanofiber Trap. *Physical Review Letters*, 109(3):033603, July 2012.

[29] Christoffer Østfeldt, Jean-Baptiste S. Béguin, Freja T. Pedersen, Eugene S. Polzik, Jörg H. Müller, and Jürgen Appel. Dipole force free optical control and cooling of nanofiber trapped atoms. *Optics Letters*, 42(21):4315, November 2017.

[30] Y. Meng, A. Dareau, P. Schneeweiss, and A. Rauschenbeutel. Near-Ground-State Cooling of Atoms Optically Trapped 300 nm Away from a Hot Surface. *Physical Review X*, 8(3):031054, September 2018.

[31] Fam Le Kien, V. I. Balykin, and K. Hakuta. Atom trap and waveguide using a two-color evanescent light field around a subwavelength-diameter optical fiber. *Physical Review A*, 70(6):063403, December 2004.

[32] D. Leibfried, R. Blatt, C. Monroe, and D. Wineland. Quantum dynamics of single trapped ions. *Reviews of Modern Physics*, 75(1):281–324, March 2003.

[33] Adam D. West, Randall Putnam, Wesley C. Campbell, and Paul Hamilton. Tunable transverse spin-motion coupling for quantum information processing. *arXiv:2007.10437 [physics, physics:quant-ph]*, July 2020.

[34] Govind P. Agrawal. *Fiber-Optic Communication Systems*. Wiley-Interscience, third edition, 2002.

[35] Jacques Bures and René Ghosh. Power density of the evanescent field in the vicinity of a tapered fiber. *Journal of the Optical Society of America A*, 16(8):1992, August 1999.

[36] Ariel Lipson, Stephen G. Lipson, and Henry Lipson. *Optical Physics*. University Press, Cambridge, fourth edition, 2011.

[37] Fam Le Kien, J. Q. Liang, K. Hakuta, and V. I. Balykin. Field intensity distributions and polarization orientations in a vacuum-clad subwavelength-diameter optical fiber. *arXiv:quant-ph/0411131*, November 2004.

[38] Amnon Yariv. *Optical Electronics in Modern Communication*. Sanders College Publishing, Philadelphia, 1991.

[39] Harry F. Davis and Arthur David Snider. *Introduction to Vector Analysis*. Wm. C. Brown Communication, Inc., Dubuque, IA, seventh edition, 1991.

[40] Milton Abramowitz and Irene A. Stegun. *Handbook of Mathematical Functions*. Dover Publications, Inc., New York, ninth edition, 1972.

[41] Mark Kasevich, David S. Weiss, Erling Riis, Kathryn Moler, Steven Kasapi, and Steven Chu. Atomic velocity selection using stimulated Raman transitions. *Physical Review Letters*, 66(18):2297–2300, May 1991.

[42] Fam Le Kien and A. Rauschenbeutel. Anisotropy in scattering of light from an atom into the guided modes of a nanofiber. *Physical Review A*, 90(2):023805, August 2014.

[43] Fam Le Kien, Philipp Schneeweiss, and Arno Rauschenbeutel. Dynamical polarizability of atoms in arbitrary light fields: General theory and application to cesium. *The European Physical Journal D*, 67(5):92, May 2013.

[44] B. Albrecht, Y. Meng, C. Clausen, A. Dareau, P. Schneeweiss, and A. Rauschenbeutel. Fictitious magnetic-field gradients in optical microtraps as an experimental tool for interrogating and manipulating cold atoms. *Physical Review A*, 94(6):061401, December 2016.

[45] Rudolf Grimm, Matthias Weidemüller, and Yurii B. Ovchinnikov. Optical Dipole Traps for Neutral Atoms. In *Advances In Atomic, Molecular, and Optical Physics*, volume 42, pages 95–170. Elsevier, 2000.

[46] Harld J. Metcalf and Peter van der Straten. *Laser Cooling and Trapping*. Springer, 1999.

[47] Christopher J. Foot. *Atomic Physics*. Oxford University Press, 2005.

[48] J M Dziedzic, J E Bjorkholm, and Steven Chu. Observation of a single-beam gradient force optical trap for dielectric particles. page 3, 1986.

[49] Takahiro Kuga, Yoshio Torii, Noritsugu Shiokawa, Takuya Hirano, Yukiko Shimizu, and Hiroyuki Sasada. Novel Optical Trap of Atoms with a Doughnut Beam. *Physical Review Letters*, 78(25):4713–4716, June 1997.

[50] J. Söding, R. Grimm, and Yu.B. Ovchinnikov. Gravitational laser trap for atoms with evanescent-wave cooling. *Optics Communications*, 119(5-6):652–662, September 1995.

[51] M. Hammes, D. Rychtarik, and R. Grimm. Evaporative cooling of cesium atoms in the gravito-optical surface trap. *arXiv:physics/0012058*, December 2000.

[52] Jun He, Bao-dong Yang, Yong-jie Cheng, Tian-cai Zhang, and Jun-min Wang. Extending the trapping lifetime of single atom in a microscopic far-off-resonance optical dipole trap. *Frontiers of Physics*, 6(3):262–270, September 2011.

[53] K. M. O'Hara, S. R. Granade, M. E. Gehm, T. A. Savard, S. Bali, C. Freed, and J. E. Thomas. Ultrastable CO 2 Laser Trapping of Lithium Fermions. *Physical Review Letters*, 82(21):4204–4207, May 1999.

[54] C. Wuttke, G. D. Cole, and A. Rauschenbeutel. Optically active mechanical modes of tapered optical fibers. *Physical Review A*, 88(6):061801, December 2013.

[55] Jakob Gillespie Hinney. *Generation of Squeezed Light with Nanofiber-Trapped Atoms*. PhD thesis, Vienna University of Technology, 2019.

[56] N.L. Manakov, V.D. Ovsiannikov, and L.P. Rapoport. Atoms in a laser field. *Physics Reports*, 141(6):320–433, August 1986.

[57] P Rosenbusch, S Ghezali, V A Dzuba, V V Flambaum, K Beloy, and A Derevianko. Ac Stark shift of the Cs microwave atomic clock transitions. *PHYSICAL REVIEW A*, page 8, 2009.

[58] Fam Le Kien, V. I. Balykin, and K. Hakuta. State-insensitive trapping and guiding of cesium atoms using a two-color evanescent field around a subwavelength-diameter fiber. *arXiv:quant-ph/0411178*, November 2004.

[59] Bindiya Arora, M. S. Safronova, and Charles W. Clark. Tune-out wavelengths of alkali-metal atoms and their applications. *Physical Review A*, 84(4):043401, October 2011.

[60] R. Mitsch, C. Sayrin, B. Albrecht, P. Schneeweiss, and A. Rauschenbeutel. Exploiting the local polarization of strongly confined light for sub-micrometer-resolution internal state preparation and manipulation of cold atoms. *Physical Review A*, 89(6):063829, June 2014.

[61] Y B Ovchinnikov, S V Shul'ga, and V I Balykin. An atomic trap based on evanescent light waves. *Journal of Physics B: Atomic, Molecular and Optical Physics*, 24(14):3173–3178, July 1991.

[62] Kathryn Moler, David S. Weiss, Mark Kasevich, and Steven Chu. Theoretical analysis of velocity-selective Raman transitions. *Physical Review A*, 45(1):342–348, January 1992.

[63] Peter Lambropoulos and David Petrosyan. *Fundamentals of Quantum Optics and Quantum Information*. Springer, 2007.

[64] D. Reitz, C. Sayrin, R. Mitsch, P. Schneeweiss, and A. Rauschenbeutel. Coherence Properties of Nanofiber-Trapped Cesium Atoms. *Physical Review Letters*, 110(24):243603, June 2013.

[65] N. Arias, V. Abediyeh, S. Hamzeloui, and E. Gomez. Low phase noise beams for Raman transitions with a phase modulator and a highly birefringent crystal. *Optics Express*, 25(5):5290, March 2017.

[66] James Bateman, André Xuereb, and Tim Freegarde. Stimulated Raman transitions via multiple atomic levels. *Physical Review A*, 81(4):043808, April 2010.

[67] P. J. Lee, B. B. Blinov, K. Brickman, L. Deslauriers, M. J. Madsen, R. Miller, D. L. Moehring, D. Stick, and C. Monroe. Atomic qubit manipulations with an electro-optic modulator. *Optics Letters*, 28(17):1582, September 2003.

[68] J. B. Naber, L. Torralbo-Campo, T. Hubert, and R. J. C. Spreeuw. Raman transitions between hyperfine clock states in a magnetic trap. *Physical Review A*, 94(1):013427, July 2016.

[69] Pippa Storey and Claude Cohen-Tannoudji. The Feynman path integral approach to atomic interferometry. A tutorial. *Journal de Physique II*, 4(11):1999–2027, November 1994.

[70] Kai Bongs. Taking atom interferometric quantum sensors from the laboratory to real-world applications. *Nature Review Letters*, pages 731–739, 2019.

[71] J. E. Hoffman, S. Ravets, J. A. Grover, P. Solano, P. R. Kordell, J. D. Wong-Campos, L. A. Orozco, and S. L. Rolston. Ultrahigh transmission optical nanofibers. *AIP Advances*, 4(6):067124, June 2014.

[72] Jonathan E. Hoffman, Fredrik K. Fatemi, Guy Beadie, Steven L. Rolston, and Luis A. Orozco. Rayleigh scattering in an optical nanofiber as a probe of higher-order mode propagation. *Optica*, 2(5):416, May 2015.

[73] J.D. Love, W.M. Henry, W.J. Stewart, R.J. Black, S. Lacroix, and F. Gonthier. Tapered single-mode fibres and devices. Part 1: Adiabaticity criteria. *IEE Proceedings J Optoelectronics*, 138(5):343, 1991.

[74] S. Ravets, J. E. Hoffman, P. R. Kordell, J. D. Wong-Campos, S. L. Rolston, and L. A. Orozco. Intermodal Energy Transfer in a Tapered Optical Fiber: Optimizing Transmission. *Journal of the Optical Society of America A*, 30(11):2361, November 2013.

[75] Ryutaro Nagai and Takao Aoki. Ultra-low-loss tapered optical fibers with minimal lengths. *Optics Express*, 22(23):28427, November 2014.

[76] J. M. Ward, A. Maimaiti, Vu H. Le, and S. Nic Chormaic. Contributed Review: Optical micro- and nanofiber pulling rig. *Review of Scientific Instruments*, 85(11):111501, November 2014.

[77] Jonathan E. Hoffman. *Optical Nanofiber Fabrication and Analysis Towards Coupling Atoms to Superconducting Circuits*. PhD thesis, University of Maryland, College Park, 2014.

[78] T.A. Birks and Y.W. Li. The shape of fiber tapers. *Journal of Lightwave Technology*, 10(4):432–438, April 1992.

[79] Abderrahim Azzoune, Philippe Delaye, and Gilles Pauliat. Optical microscopy for measuring tapered fibers beyond the diffraction limit. *Optics Express*, 27(17):24403, August 2019.

[80] Adrien Godet, Abdoulaye Ndao, Thibaut Sylvestre, Vincent Pecheur, Sylvie Lebrun, Gilles Pauliat, Jean-Charles Beugnot, and Kien Phan Huy. Brillouin spectroscopy of optical microfibers and nanofibers. *Optica*, 4(10):1232, October 2017.

[81] E. Vetsch, S. T. Dawkins, R. Mitsch, D. Reitz, P. Schneeweiss, and A. Rauschenbeutel. Nanofiber-Based Optical Trapping of Cold Neutral Atoms. *IEEE Journal of Selected Topics in Quantum Electronics*, 18(6):1763–1770, November 2012.

[82] C Lacroûte, K S Choi, A Goban, D J Alton, D Ding, N P Stern, and H J Kimble. A state-insensitive, compensated nanofiber trap. *New Journal of Physics*, 14(2):023056, February 2012.

[83] G. Sagué, E. Vetsch, W. Alt, D. Meschede, and A. Rauschenbeutel. Cold-Atom Physics Using Ultrathin Optical Fibers: Light-Induced Dipole Forces and Surface Interactions. *Physical Review Letters*, 99(16):163602, October 2007.

[84] Maxime Joos, Alberto Bramati, and Quentin Glorieux. Complete polarization control for a nanofiber waveguide using the scattering properties. *Optics Express*, 27(13):18818, June 2019.

[85] J Lee, J A Grover, J E Hoffman, L A Orozco, and S L Rolston. Inhomogeneous broadening of optical transitions of ^{87} Rb atoms in an optical nanofiber trap. *Journal of Physics B: Atomic, Molecular and Optical Physics*, 48(16):165004, August 2015.

[86] Signe B. Markussen, Jürgen Appel, Christoffer Østfeldt, Jean-Baptiste S. Béguin, Eugene S. Polzik, and Jörg H. Müller. Measurement and simulation of atomic motion in nanoscale optical trapping potentials. *Applied Physics B*, 126(4):73, April 2020.

[87] R Ritter, N Gruhler, W H P Pernice, H Kübler, T Pfau, and R Löw. Coupling thermal atomic vapor to an integrated ring resonator. *New Journal of Physics*, 18(10):103031, October 2016.

[88] Yuri B Ovchinnikov and Folly Eli Ayi-Yovo. Towards all-optical atom chips based on optical waveguides. *New Journal of Physics*, 22(5):053003, May 2020.

[89] Ethan A. Scott, John T. Gaskins, Sean W. King, and Patrick E. Hopkins. Thermal conductivity and thermal boundary resistance of atomic layer deposited high- k dielectric aluminum oxide, hafnium oxide, and titanium oxide thin films on silicon. *APL Materials*, 6(5):058302, May 2018.

[90] D. J. Wineland and Wayne M. Itano. Laser cooling of atoms. *Physical Review A*, 20(4):1521–1540, October 1979.

[91] D. A. Varshalovish, V. K. Moskalev, and A. N. Khersonskii. *Quantum Theory of Angular Momentum*. World Scientific, 1988.

[92] V. Devanathan. *Angular Momentum Techniques in Quantum Mechanics*. Kluwer Academic Publishers, 1999.